A Study of Collision Cascade Collapse in Cu_3Au

by

Thomas J. Black

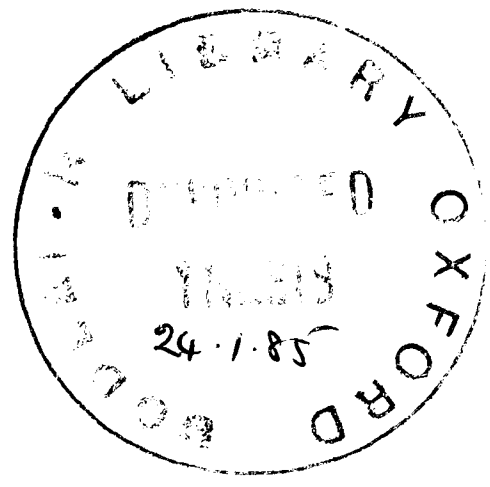

Wolfson College, Oxford

September 1984

ABSTRACT

A Study of Collision Cascade Collapse in Cu_3Au

Thomas J. Black

Wolfson College, Oxford

A thesis submitted for the degree of Doctor of Philosophy

Trinity Term, 1984

This thesis describes an ion irradiation study of ordered Cu_3Au. Argon, Copper and Krypton ions of 50 and 100keV were implanted to nominal doses of 10^{11} ions cm^{-2} both at room temperature and at liquid helium temperature. The damage induced at low temperature was observed in-situ and after subsequent warming to room temperature.

The collapse of collision cascades to vacancy dislocation loops was observed to occur with moderately high probability under all irradiation conditions at low temperature, with no subsequent increase in the number of loops on warming. Comparison of the collapsed fraction of cascades at low temperature with that produced by room temperature irradiation revealed that the collapse process is more efficient in the latter case. An increase in collapse probability with ion mass was also observed, although no dependence on ion energy was found over the range investigated.

Quantitative analysis of the disordered zones which result in ordered Cu_3Au at individual cascade sites revealed that cascades which had collapsed to loops generally produced larger disordered zones. Additionally, increases in disordered zone size with ion mass, ion energy and irradiation temperature were identified. The observation that disordered zone sizes exceed the theoretically predicted cascade dimensions for the case of the highest energy density in this study (50keV Kr) is interpreted as evidence for leakage of energy from the cascade region to the surrounding lattice.

A model is proposed which attributes the observed cascade collapse behaviour to vacancy migration during the cooling of the cascade region being systematically directed toward its centre, and accounts for the observed disordered zones in terms of extensive atomic rearrangement during the cooling. The major factors identified as controlling this vacancy and atomic motion are the initial spatial distribution of energy and vacancies within the region, and the rate at which the region cools.

CONTENTS

		Page
CHAPTER 1	INTRODUCTION	1
CHAPTER 2	PREVIOUS STUDIES	
	2.1 INTRODUCTION	3
	2.2 BASIC CONCEPTS	3
	2.3 THEORY AND SIMULATION	7
	2.3.1 Methods	7
	2.3.2 Cascade Configurations	8
	2.3.3 Cascade Sizes	10
	2.3.4 Defect Production	12
	2.3.5 Spike Effects	14
	2.4 EXPERIMENTAL STUDIES	17
	2.4.1 TEM Observations	18
	2.4.2 FIM Observations	24
	2.4.3 Sputtering Studies	26
	2.4.4 Resistivity Studies	27
CHAPTER 3	OBJECTIVES AND TECHNIQUES	
	3.1 INTRODUCTION	29
	3.2 OBJECTIVES	29
	3.3 THE SUPERLATTICE TECHNIQUE	32
	3.3.1 The Alloy Cu_3Au	32
	3.3.2 Disordered Zone Imaging	33
	3.3.3 Dislocation Loop Imaging	36
	APPENDIX 3.1	40
CHAPTER 4	SPECIMEN PREPARATION	
	4.1 INTRODUCTION	42
	4.2 EQUIPMENT AND PROCEDURE	43
	4.3 THEORETICAL CONSIDERATIONS	43
	4.3.1 The Evaporation	43
	4.3.2 Film Nucleation and Growth	45

4.4 SPECIMEN PRODUCTION 46

4.4.1 Evaporation 46
4.4.2 Ordering 49

4.5 SPECIMENS PRODUCED 50

CHAPTER 5 EXPERIMENTAL TECHNIQUES

5.1 INTRODUCTION 52

5.2 IRRADIATIONS 53

5.2.1 Low Temperature Irradiations 53
5.2.2 Room Temperature Irradiations 55

5.3 ELECTRON MICROSCOPY 56

5.4 DEFECT YIELD DETERMINATIONS 59

5.4.1 Procedure 59
5.4.2 Uncertainties 61

5.5 ZONE AND LOOP SIZING 67

5.5.1 Method 67
5.5.2 Uncertainties 69
5.5.3 Subzone Frequency 70

CHAPTER 6 RESULTS

6.1 INTRODUCTION 71

6.2 DEFECT YIELD RESULTS 72

6.2.1 Low Temperature Irradiation Results 72
6.2.2 Room Temperature Irradiation Results 75
6.2.3 Comparison of Room and Low Temperature Irradiations 75
6.2.4 Errors and Limitations 76

6.3 ZONE AND LOOP SIZES 79

6.3.1 Correlation between Zone Size and Collapse Probability 80
6.3.2 Correlation between Zone Size and Ion Mass 80
6.3.3 Correlation between Zone Size and Ion Energy 81
6.3.4 Correlation between Zone Size and Irradiation Temperature 82
6.3.5 Loop Sizes 83
6.3.6 Errors and Limitations 83

6.4 SUMMARY OF RESULTS 87

APPENDIX 6.1 89

APPENDIX 6.2 90

APPENDIX 6.3 92

CHAPTER 7 DISCUSSION

7.1 INTRODUCTION 93

7.2 DISORDERING 98

7.2.1 Possible Mechanisms 98
7.2.2 The Model 105

7.3 CASCADE COLLAPSE 110

7.4 SUMMARY 117

APPENDIX 7.1 119

REFERENCES 120

APPENDIX A

APPENDIX B

ACKNOWLEDGMENTS

Sincere thanks are due primarily to my two supervisors Dr. Mike Jenkins at Oxford and Dr. Colin English at Harwell who always made time for my problems, offering continual support and friendship throughout my three years at Oxford.

For her assistance in the typing and reading of this manuscript, but more importantly for her understanding during its production, I am grateful to my fiancée Ann. For the sacrifices and encouragement of my Mum and Dad, without which I would never have reached Oxford, I shall be forever indebted.

For his part in the low temperature experiments, and for the friendship he extended, very special thanks are due to Dr. Mark Kirk. My initiation to the delights of thin film evaporation was provided by Dr. Chris Grovenor to whom I must express my gratitude.

Thanks are due also to Mr. Graham Dixon-Brown for his expert maintenance of the JEM100B microscope, and to Professors Hirsch and Christian for the provision of facilities at Oxford.

At Argonne, Dr. Tony Taylor, Dr. Wayne King and Mr. Ed Ryun deserve special mention for their attention during my stay there, although I am indebted to all the staff of the HVEM-Tandem facility. For his operation of the ion accelerator at Harwell thanks are due to Mr. Mick Warman.

In addition to those singled out above, there are many at Oxford, Harwell and Argonne who have shaped my thoughts on radiation damage and wider issues, and to them all I am genuinely grateful.

Financial support for this work was provided by the Science and Engineering Research council and by AERE Harwell, which also provided photographic and other services.

CHAPTER ONE

INTRODUCTION

Fast neutrons, such as are generated in a fast reactor or fusion device are slowed by the structural components surrounding the core and may seriously affect their physical and mechanical characteristics. Void swelling, irradiation hardening and irradiation induced creep are known to result from neutron bombardment and have been extensively investigated during the past twenty years. Such manifestations of neutron damage are usually the result of point defect production and subsequent migration to clusters or sinks, although the production of transmutation gases from nuclear reactions (e.g. He) is considered important in void nucleation and growth.

The fact that under neutron bombardment, the point defects are generated in highly localized volumes by collision cascades (Chapter Two) and not in a homogeneous manner, has significant consequences for the subsequent evolution of the damage structure. In particular, the phenomenon of cascade collapse, which results in the production of vacancy dislocation loops at the centre of the cascade volume, restricts the number of vacancies which may contribute to the swelling and creep of the material. Additionally, the loops thus generated may act as pinning centres for dislocations, resulting in hardening. Despite the obvious importance of the collapse process, surprisingly little is known of the point defect interactions

which result in the production of loops. In fact, only recently have the various stages of the cascade process itself been determined.

The object of the present study was to investigate the phenomenon of collapse, and in particular to determine if it is athermal as had often been suggested previously.

In Chapter Two a brief resumè of previous investigations of cascades and their collapse is presented in order that the motivation for this work may be fully appreciated. Chapter Three lays out the objectives of the experiments conducted and the principles of the techniques employed. The details of the procedures adopted are covered in Chapters Four and Five, with the results obtained presented in the penultimate chapter. Finally, the interpretation of these results and their significance is recounted in Chapter Seven.

CHAPTER TWO

PREVIOUS STUDIES

2.1 INTRODUCTION

In this chapter, those aspects of radiation damage relevant to the present study are presented in order that the significance of the experiments performed may be established. No attempt has been made to exhaustively review the subject of fundamental radiation damage, and the more comprehensive treatment of high density cascades by Thompson [1981] is suggested if further information is required.

Section 2.2 presents an outline of the basic features of displacement cascades, with Sections 2.3 and 2.4 detailing the theoretical (including computer simulation) and experimental studies which have contributed to the present understanding of the phenomenon.

2.2 BASIC CONCEPTS

If a fast particle, incident on a solid, transfers sufficient energy to a lattice atom, it may displace it, thus producing a vacant lattice site (vacancy) and forcing the displaced atom to reside in an interstice of the atomic array (interstitial). Such a vacancy-interstitial arrangement is known as a Frenkel Pair. The energy required to separate the interstitial sufficiently from the vacancy to prevent mutual annihilation (i.e. to carry the interstitial beyond the Recombination

Volume of the vacancy), is the Displacement Threshold Energy. Computer simulations [Erginsoy et al 1964; Stuart et al 1976] have demonstrated that this depends on the material and on the direction of displacement. For a low index direction in an fcc material such as Cu, it may be as low as ~20eV, whereas in bcc it generally exceeds this value, especially if the displacement is randomly orientated.

The nature of the interaction between a fast particle and a lattice atom determines the fraction of the particle's energy which may be transferred. This interaction is heavily dependent on their mass ratio, the particle's velocity, charge distribution etc. With respect to reactor design, the most important class of fast particle is the neutron which is capable of producing high energy recoils as it interacts with atomic nuclei by short range nuclear forces. The atom with which the neutron interacts is known as the Primary Knock On (PKO), the recoiling energy of which is an increasing function of neutron energy.

Fast fission neutrons may transfer several hundred keV to a lattice atom, generally in elastic collisions. Anticipated knock-on energies in fusion devices are expected to average around 500keV [Birtcher et al 1982].

Charged particles on the other hand, interact with atoms by relatively "soft" coulomb forces, generally producing knock-ons of lower energy. From Fig. 2.1 it is clear that even heavy ions of many MeV produce lower energy recoils than fast neutrons, although for high energy ions (E~50MeV) of the

Fig 2.1 Energy dependence of PKO spectrum for various charged particles incident on nickel, and for fast neutron bombardment of iron. [From Marwick 1974]. (The 3.5μm and 2.5μm curves for 46.5MeV Ni refer to mean damage depths, varied by "rocking" the specimen which produces a wider damage layer).

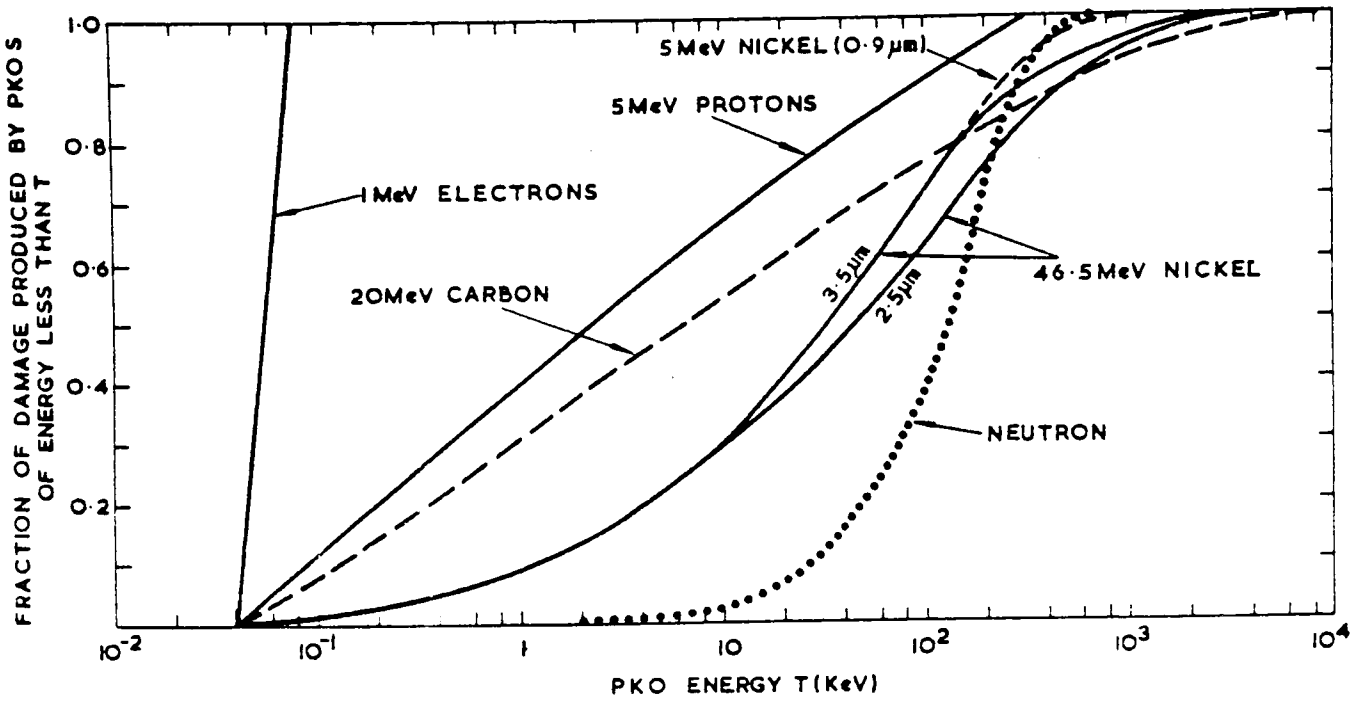
FRACTION OF DAMAGE PRODUCED BY PKO S OF ENERGY LESS THAN T
1·0
0·8
0·6
0·4
0·2
5MeV NICKEL (0·9μm)
5MeV PROTONS
1MeV ELECTRONS
20MeV CARBON
3·5μm
2·5μm
46·5MeV NICKEL
NEUTRON
10⁻²
10⁻¹
1
10
10²
10³
10⁴
PKO ENERGY T(KeV)

target species, the recoil spectrum is similar. Energetic electrons however, are too light to generate fast recoils, and 1MeV electrons rarely produce knock-ons above 50-100eV.

Since very fast (many MeV) ions create similar knock-on energies to neutrons, but are readily available as high intensity beams - thus giving greatly enhanced damage rates - they are often used to simulate the effects of prolonged exposure to neutron fluxes. In this way a beam of 50MeV Ni ions (for example), can generate similar damage in a few minutes, to that which would be accumulated over many days in a fast reactor. Alternatively, ions of ~5-200keV are frequently employed to simulate the individual PKOs generated by neutrons. Above about 100keV the energy lost by ions to the electrons in a metallic solid becomes an appreciable fraction of the total [Lindhard et al 1963], as illustrated in Fig. 2.2, but below this the ion's energy is lost predominantly through elastic collisions with atomic nuclei. Brinkman [1954] demonstrated that as the energy drops, the mean free path between collisions approaches the lattice spacing and a regime is entered in which many atoms are displaced in a local volume, as the PKO energy is distributed between successive generations of knock-ons. Such a "collision cascade" as it has become known, is shown schematically in Fig. 2.3. The PKO generated by neutron or fast heavy-ion bombardment generally falls into this regime, and collision cascades are the primary unit of damage produced by such projectiles. The function of the lower energy ion simulations (~5-200keV) is to generate monoenergetic cascade populations, and thus allow systematic investigation of the phenomenon.

Fig 2.2 Rate of energy loss through electronic excitation $(dE/dx)_{ex}$ and elastic collisions with nuclei $(dE/dx)_c$ for carbon ions in graphite. [From Thompson 1969]. (Curves for metallic solids are similar to those shown).

Fig 2.3 Schematic representation of the dynamic phase of a collision cascade. [From Thompson 1969]. Primary, secondary and tertiary knock-ons are visible.

Within this collision cascade, which is typically about 100Å across, many Frenkel pairs are produced and a local vacancy concentration of several atomic percent may result. The effect on the lattice of depositing such energy into a small volume is still a matter of controversy although it now seems likely that appreciable atomic rearrangements may result if the recoil density is sufficiently high. The extensive theoretical, simulation and experimental studies recounted in the following two sections have led to the "four phase" description for the temporal evolution of a cascade which will now be presented.

Initially there exists a Displacement phase (lasting $\sim 10^{-13}$s) during which many atoms are displaced as the PKO loses its energy to secondary knock-ons, which in turn create further displacements, etc. The volume within which this process occurs is known as the cascade volume although in most cases only some fraction of the total number of enclosed atoms will be directly involved in this initial phase. Local thermal equilibrium may ensue if the energy is then spread throughout the atoms of the region such that a Maxwell-Boltzmann distribution of velocities is attained, although it is not clear that such a process will occur in diffuse, low recoil density cascades. This second, Relaxation phase which may result in much vacancy-interstitial recombination, takes typically 5×10^{-13}s to occur. Following this the cascade region cools during the Cooling or Spike phase by losing energy to the surrounding lattice. This "spike phase" varies in length from 10^{-12}s for rapidly quenched cascades, to 10^{-10}s if cooling is

slower. Strictly, at this point the cascade process has terminated, but a fourth phase, during which the remaining point defects may migrate in order to cluster or anneal at sinks has been identified by some authors. This Annealing phase lasts ~10^{-9} s-10^{-7} s and will only occur if the ambient lattice temperature is high enough to permit long range defect migration.

Transmission electron microscopy studies have established that at some stage in this evolution, the vacancy component of the cascade damage structure may form a dislocation loop. This agglomeration of vacancies has become known as Cascade Collapse. Exactly what precipitates this collapse and at which point in the cascade evolution it occurs has not yet been established unambiguously, and this remains the major question in fundamental radiation damage research. The studies described in the subsequent sections have however contributed to a partial understanding of the phenomenon.

2.3 THEORY AND SIMULATION

2.3.1 Methods

Modelling of displacement cascades has been attempted in two ways. Initially, consideration of the elastic energy deposition led to an analytical approach which allows predictions to be made about the average behaviour of cascades, but the advent of fast electronic computers in the early 1960s enabled simulation of individual events. Initially, the approach adopted by the group at Brookhaven Laboratories [Gibson et al 1960] was to consider all atomic interactions in

the cascade volume. This fully dynamic method is however limited to low energy simulations due to its heavy demands on computer time and core memory. In an attempt to circumvent this problem, the so-called binary collision approximation was developed by Robinson and Torrens [1974]. In all work of this type it is assumed that all collisions may be treated as two body interactions, with one of the partners at rest. This dramatically reduces the number of required computations but may only be used in circumstances in which the binary approximation holds. Thus, beyond the collision phase of a cascade, the validity of binary simulations must be suspect, especially in high density cascades, where many atoms may be simultaneously in motion in a local volume.

2.3.2 Cascade Configurations

As pointed out above, as early as 1954 Brinkman's analysis of collision cross-sections between atoms of the same species led to his proposal of cascades or displacement spikes. Shortly after this, Silsbee [1957] suggested that the regular crystalline nature of metallic solids may affect such atom-atom collisions by producing focussing of collisions along close-packed directions such as <110> in fcc or <111> in bcc. Such chains of collisions, by which momentum may be transferred over long distances in a crystal are known as Focussed Collision Sequences (Fig. 2.4). Seeger [1958] extended this concept further by proposing that if each atom in the chain replaces its neighbour in a Replacement Collision Sequence (RCS) or Dynamic Crowdion, then vacancies and interstitials may be produced at opposite ends of such chains. (There

Fig 2.4 Schematic representation of a focussed collision sequence. The angles are such that $\theta_{n-1} > \theta_n > \theta_{n+1}$ which results in focussing of the momentum along a well defined direction. This effect is enhanced by collisions with atoms surrounding (but not included in) the chain. Such a mechanism, which alows FCS to propogate at higher energies, is know as Assisted Focussing.

Fig 2.5 Defect configurations at end of collision phase for a 1keV cascade in Cu, as predicted by binary simulation [From Heinisch 1983]. The vacancy core (cubes) and interstitial periphery (crosses) are visible.

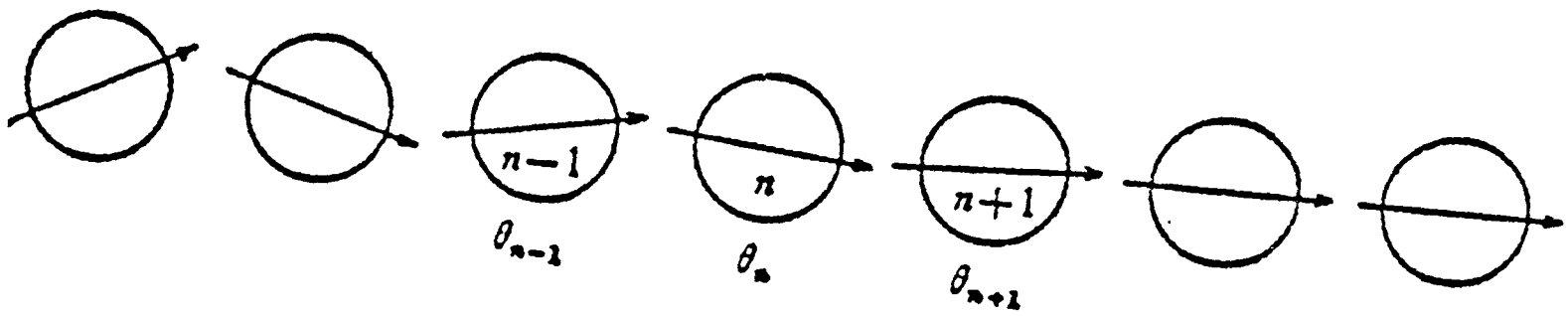

[redacted]

exists some controversy over the lengths of such sequences - see later). He suggested that the occurrence of such a phenomenon within a cascade may result in a vacancy-rich core surrounded by a diffuse shell of interstitials. Subsequent fully dynamic, low energy simulations demonstrated the existence of RCS in both Cu [Vineyard 1963] and α- Fe [Erginsoy et al 1964], and some evidence was obtained to support the existence of a vacancy rich central region [Erginsoy et al 1965]. More recent simulations employing both the binary collision approximation [see e.g. Heinisch 1983] and fully dynamic treatments [King and Benedek 1983] have clearly demonstrated the accuracy of Seeger's prediction (Fig. 2.5). Field ion microscope observations have also confirmed the existence of such vacancy rich regions, and transmission electron microscope studies have demonstrated their instability by imaging the vacancy loops which often result from the collapse of such regions (Section 2.4.1).

Higher energy computer work (ie binary), has also demonstrated that in cases of a high PKO energy, an atom may escape collision for many atomic distances and thus induce a subcascade, removed from the initial one, when it eventually collides (Fig 2.6) [eg Beeler and Beeler 1975]. Some controversy exists about the energy at which such a regime is entered although Heinisch [1983] has observed that cascades created by PKOs of energy greater than 30keV often consist of subcascade units, similar in size to a 30keV cascade.

Fig 2.6 Subcascade structure of a 50keV cascade in Cu [From Heinisch 1983]. Larger dots represent vacancies, with the smaller for interstitials. Three distinct subcascade damage regions are visible.

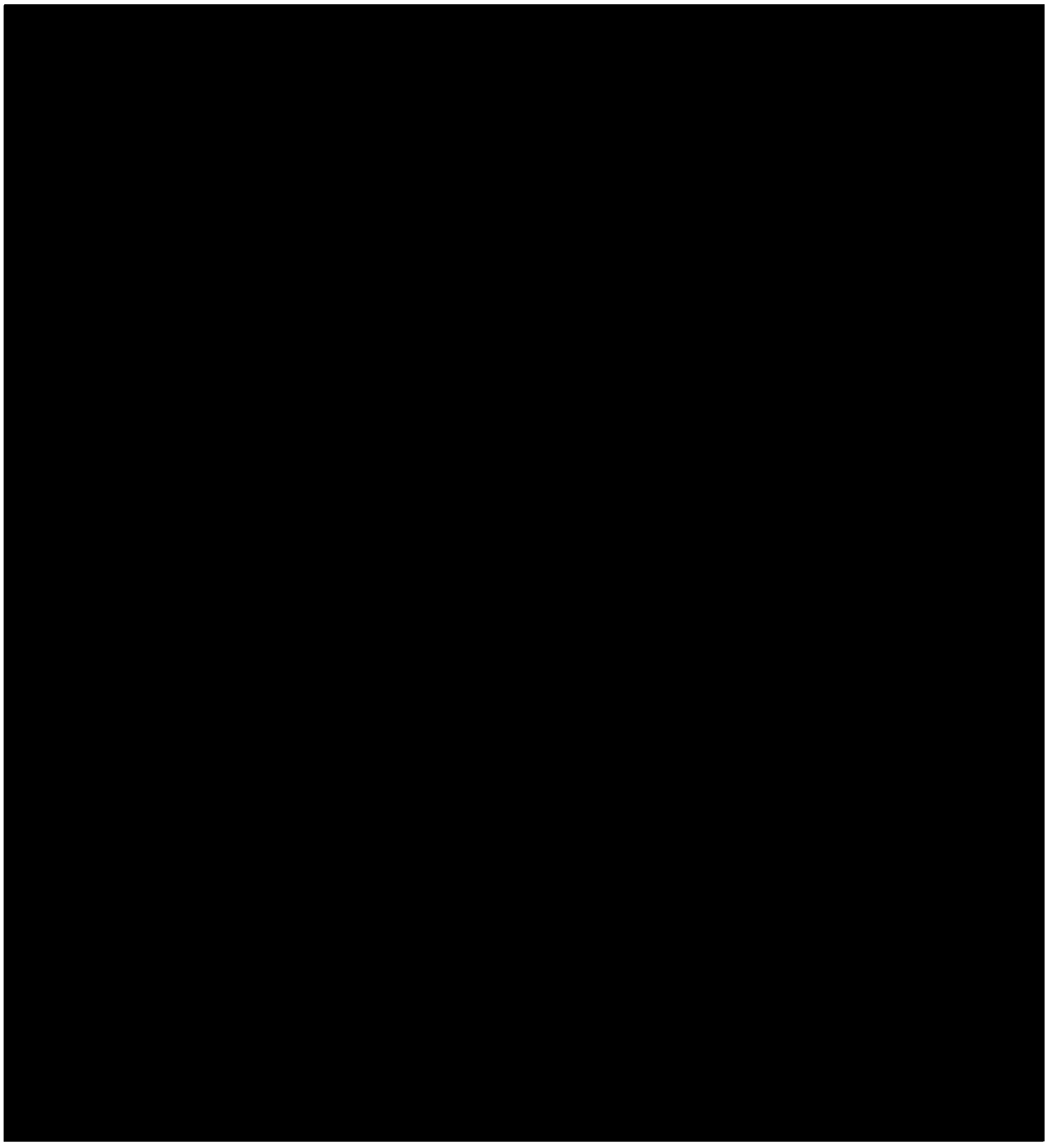

2.3.3 Cascade Sizes

The most complete theory for cascade size predictions is the analytical WSS theory, which is based on the binary approximation. The work of Lindhard et al [1963] mentioned previously, allows the Damage Energy (i.e. that not lost to electronic excitation) to be calculated for any ion/target combination, and Winterbon et al [1970] used a linearized form of the Boltzman transport equation to determine the spatial distribution of this elastically deposited energy. This distribution may be used to estimate cascade dimensions by identifying the second moment of the distribution with the cascade radius. Some important trends in cascade dimensions are predicted by this work. The cross-section for a high energy collision increases as the PKO energy decreases and as the PKO mass approaches that of the target. This behaviour of the cross-section results in:

(i) Highly energetic ions undergoing many low-energy collisions and producing diffuse cascades.

(ii) Light ions undergoing many low-energy collisions and producing diffuse cascades.

(iii) Heavy ions undergoing few high-energy collisions and producing compact cascades.

Additionally, the atomic mass of the target influences the cascade dimensions, with those generated in heavy targets tending to be more compact than those in lighter materials. Diffuse cascades, such as are produced by highly energetic

light particles, result in the movement of only a small fraction of the total number of atoms in the cascade volume during the collision phase. It thus seems unlikely that the relaxation phase will redistribute the PKO energy throughout all the atoms of the region, and collective motion is expected to play a relatively minor role. Thus, if two such cascades are spatially and temporally superimposed, they should not interact. This has led to such events being termed <u>linear</u> cascades. For heavy ions however, the opposite is true and collisions between moving atoms and the consequent collective effects are expected to play an important part. Thus, an equivalent superposition should result in extensive interaction. These have therefore become known as <u>non-linear</u> cascades. A useful parameter which summarizes this is the Energy Density, θ, [Sigmund 1974]. This is defined as the average atomic kinetic energy in the cascade volume, and is simply the PKO energy divided by the number of atoms in the volume. Thus, more compact cascades have higher energy densities. At some value of energy density it is expected that the binary approximation will break down, and the WSS theory must cease to describe such cascades accurately.

The major problem associated with this analytical approach is that the elastically deposited energy distribution, having been derived by statistical means, inevitably describes the cumulative average cascade (i.e. an envelope within which individual cascades will be produced), and cannot account for subcascades which are known to occur within individual events. It is therefore to be expected that individual cascades will

rarely occupy the whole of the WSS volume, and that this parameter must overestimate the spatial extent of cascades. Binary computer simulations by Walker and Thompson [1978], whilst confirming the trends in cascade sizes predicted by WSS, have demonstrated that the analytical approach does indeed overestimate cascade dimensions, especially in cases of low energy density (ie especially for diffuse cascades) (Fig 2.7).

The extent to which vacancies and interstitials are separated in a cascade, and therefore the degree of recombination expected, depends on the lengths of RCS in the material. This is a subject on which experimental and theoretical estimates disagree significantly. Some experimental results have been interpreted as indicating that RCS lengths exceed 150-200Å (Section 2.4), whereas recent fully dynamic simulations [Tenenbaum 1978; King and Benedek 1982] and analytical calculations [Kapinos and Kevorkyan 1983] suggest that RCS are generally much shorter ($l<50$Å). Furthermore, this work indicates that longer sequences are expected at lower temperatures due to defocussing of sequences by lattice vibrations at higher temperatures.

2.3.4 Defect Production

In addition to the spatial configuration of defects in a cascade, the number generated is also important. This problem was first addressed by Kinchin and Pease [1955] who viewed the atoms involved as hard spheres, and obtained the simple result:

Fig 2.7 Comparison of computer simulated cascades (binary) with WSS predictions for various 20keV ions in a silicon target. The dots show the predicted vacancy locations, and the solid lines are the contours for 1/10th maximum energy as given by WSS. [From Walker and Thompson 1978]. The tendency for WSS to overestimate cascade sizes is apparent, especially at lower ion masses where subcascades are prevalent. (Note increasing scale on (a), (b), (c).)

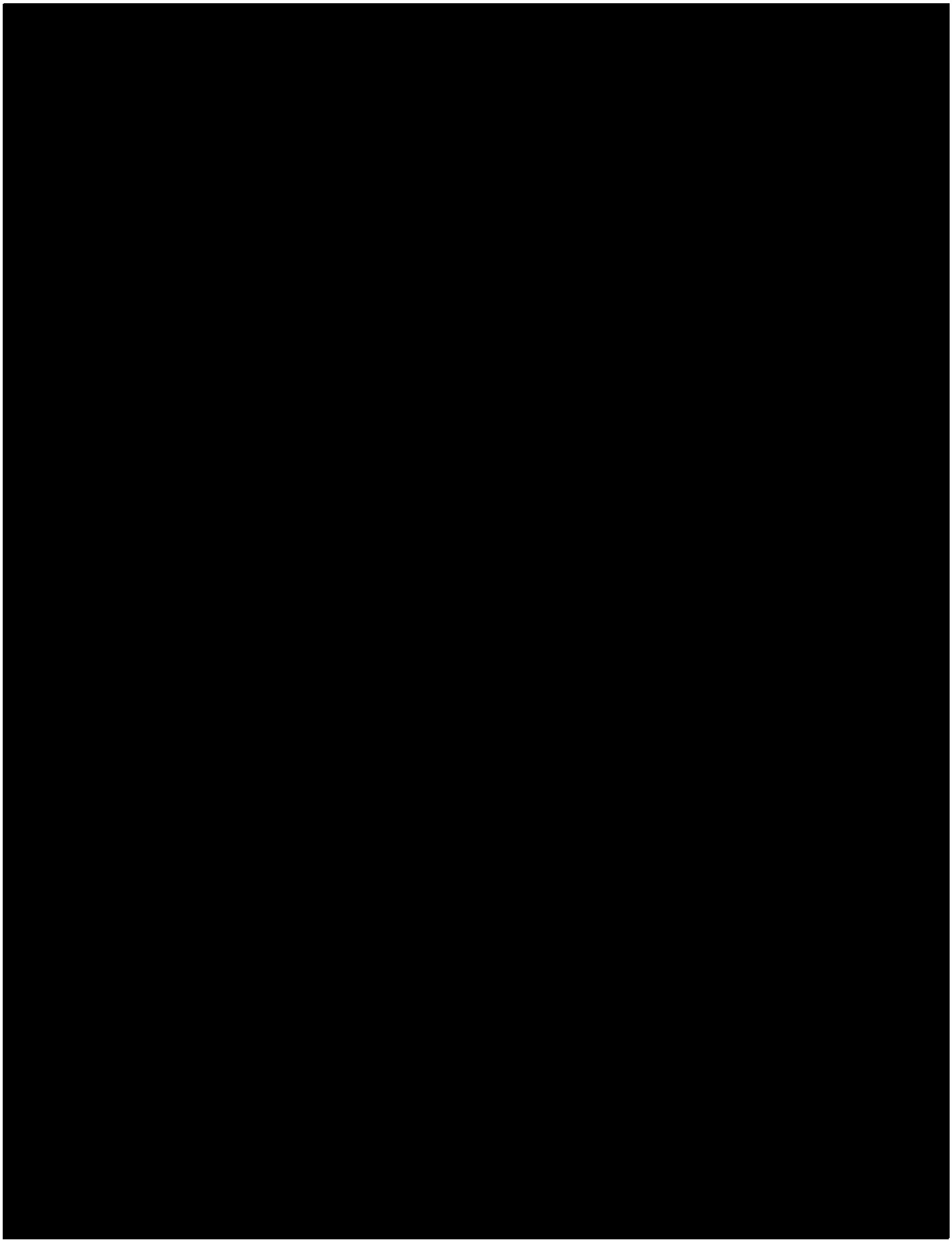

$$N = E/2E_d$$

for $E > 2E_d$, and $N = 1$ for $E_d < E < 2E_d$.

Where: N is the number of defects produced.

E is the PKO energy.

E_d is the displacement threshold (assumed constant).

Which simply suggests that 50% of the PKO energy is used to generate Frenkel pairs, with the remainder spent in sub-threshold encounters. This however, has been found to over-estimate the numbers measured by experiment (Section 2.4.2). Sigmund [1969a] and Norgett et al [1972] critically reviewed this expression and suggested the modified (NRT) version:

$$N = \kappa\nu(E)/2E_d$$

Where: $\nu(E)$ is the Damage Energy. (i.e. allowing for electronic losses). An analytical expression for this is given by Norgett et al [1972].

κ is an efficiency factor which accounts for the fact that the "hard sphere" concept does not apply to atoms which have "softer" interactions.

Sigmund indicated that a value of $\kappa = 0.8$ would be most realistic, and this was confirmed by the binary simulations of Torrens and Robinson [1972] who obtained a value of 0.8 irrespective of the PKO energy. It should be remembered however, that even these modified expressions assume a single value for the displacement threshold, which Erginsoy and co-workers have indicated is unrealistic (see previous).

Recent fully dynamic simulations have indicated that

consideration of only the collision phase of the cascade is inadequate for a full description of the defect production involved. Guinan and Kinney [1981] have carried out simulations (for PKO energies of up to 10keV, far in excess of previous dynamic simulations) which are in direct opposition to the binary treatment of Torrens and Robinson in that they predict a decrease in the efficiency κ, as the PKO energy is increased. This decrease in κ, which levels out at ~0.4 for PKO energies of 100 times the threshold (Fig. 2.8), has also been confirmed by various experimental studies, and close examination of the simulations indicate that it is due to significant Frenkel pair recombination during the relaxation and cooling phases of the cascade. In support of this conclusion, the dynamic simulations of King and Benedek [1983] also indicate appreciable recombination during relaxation and cooling of the cascade. Interestingly, they find that the number of defects present at the end of the collision phase compares well with the above analytical expressions, but that it decreases subsequently due to recombination.

2.3.5 Spike Effects

As indicated previously, in the case of high density cascades, non-linear effects are likely to occur due to the collective motion of many atoms during the spike phase of the cascade.

Beeler [1970] recognized that toward the end of the collision phase, the PKO energy, which up to that point is shared between the energetic knock-ons only, must be distributed between many more atoms as the volume approaches local

Fig 2.8 Energy dependence of damage efficiency as measured from fully dynamic computer simulation and various experimental studies. [From Guinan and Kinney 1981].

Fig 2.9 Reconstruction from FIM images of a 60keV Kr cascade generated in tungsten. [From Wei et al 1981]. The dots represent vacancies with nearest neighbour agglomerates joined.

equilibrium. He calculated that this process should occur within a few lattice vibration periods, after which a Maxwell-Boltzman velocity distribution should have been established. The collective motion which follows such equilibration has come to be known as a spike. Previously, Brinkman [1954] had foreseen this possibility of a locally heated region, and estimated that the melting temperature of most metals would be exceeded. Seitz and Koehler [1956] examined the possibility of local melting resulting from the cascade process and concurred with Brinkman that temperatures exceeding those at the melting point may well be attained (10^4K), but only for a very short time ($\sim 10^{-11}$s). Sigmund [1974] used the Gaussian energy deposition profiles predicted by the WSS theory to estimate the average atomic energy (energy density) within the cascade volume, and the period over which these energies would be maintained. This work also indicated that atoms within a cascade volume may attain energies ranging from a few tenths of an eV to several tens of eV, greatly exceeding that required for melting in some cases. Not surprisingly, the more dense cascades which achieve higher energy densities, cool more rapidly than diffuse cascades. Thus, it was still not clear if these high energy densities could be maintained for sufficient time to induce melting.

It was pointed out by Chudinov et al [1977] that the normally adopted practice of calculating the maximum "temperature" anticipated to arise, and applying the heat conduction equation to that temperature (as in Sigmund's work), is not a legitimate procedure. As the maximum expected temperature is often of the order of 10^4K, which corresponds to atomic velo-

cities greatly in excess of that of sound in a metal, no group motions exist to remove the energy and they propose that collisional mechanisms, such as RCS, must dominate until the velocity of sound is attained. This lower initial "temperature" for the cooling phase results in longer cascade lifetimes than predicted by Sigmund's treatment.

As previously indicated, binary computer models are of no value in simulating this stage of the cascade, but fully dynamic models have been successfully applied to the problem. King and Benedek [1983] found a very distinct transition from the collision phase to the cooling phase of the cascade with the number of point defects reaching a maximum at the transition, and extensive recombination being observed during the latter stage. An important point to emerge from this study is that a Maxwell-Boltzman velocity distribution is not observed until well into the cooling phase (6.6×10^{-12}s in a 650eV cascade), and the authors warn against the assignment of a "temperature" until this has been achieved. This would appear to be very similar to the conclusions reached by Chudinov et al indicated above. In another study, Guinan and Kinney [1981] have observed vacancy jump rates during the cooling phase which are far in excess of that which would be predicted from equilibrium considerations. This is thought to be due to the energy released by the high degree of recombination observed (see above). The implications of this enhanced vacancy motion must be considered in any investigation of the phenomenon of cascade collapse.

By delaying the initiation of the simulation until the start

of the cooling phase, Protasov and Chudinov [1982] have been able to follow the process further than previous studies. The most significant results of this study are not only that local melting, followed by extensive vacancy motion upon recrystallization is observed, confirming Guinan and Kinney's observations, but that this motion becomes systematically directed toward the cascade centre, an observation which has obvious implications for the understanding of loop production. "Fast" cooling of the region ($6x10^{14}$ Ks^{-1}) results in a doubling of the vacancy concentration at the centre, whereas slow cooling ($2x10^{14}$ Ks^{-1}) produces a void which has been observed to collapse to a Frank dislocation loop if the thermal pressure of the surrounding lattice is simulated. A similar study by Chudinov et al [1983] has demonstrated that disordering of the binary alloy Ni_3Sn may occur if cooling is slow enough.

Many of these theoretical and simulation studies have been prompted by the extensive experimental work carried out over the same period and these are briefly reviewed in the next section.

2.4 EXPERIMENTAL STUDIES

Many methods have been employed in the experimental investigation of displacement cascades although four in particular have contributed significantly to the understanding of the phenomenon. They are: transmission electron microscopy (TEM), field ion microscopy (FIM), heavy ion sputtering and residual resistivity measurements. The most important

contributions of each will be recounted briefly in the following sections.

2.4.1 TEM Observations

Initially such investigations were restricted to observing the vacancy loops which occur only at the sites of collapsed cascades, but more recently the technique of observing disordered zones in ordered alloys has relaxed this restriction.

(a) Dislocation loop observations

TEM observation of dislocation loops produced by ion irradiation was initiated in the early 1960s [e.g. Brandon and Bowden 1961] although the first quantitative study was performed by Merkle [1966]. The most extensive work has been in fcc metals with bcc and hcp receiving less attention. In most cases, loops have been observed provided the ion energy exceeds a threshold value (eg ~5keV for Xe bombardment of Au [Merkle et al 1970]). The geometry of the loops formed in most cases is consistent with collapse occurring onto the closest packed planes, followed by unfaulting if this is energetically favourable. Thus, in fcc, loops often remain faulted with $\underline{b}=1/3\langle 111\rangle$, but in bcc, they generally unfault as the stacking fault energy is higher in such materials. In the exceptional case of α-Fe, energetically unfavourable $\underline{b}=\langle 100\rangle$ loops have been observed [Jenkins et al 1978]. The reason for this is unknown, although such loops were only found in cascades of high energy density. In lower energy regimes, each cascade is

expected to produce a maximum of one loop, but in the case of high PKO energies, subcascades are expected to form (Section 2.3.2) and TEM studies [eg Merkle and Averback 1975] have demonstrated that individual subcascades may contain loops. Thus, at high energy (E>100keV) several loops may result from each incident ion.

In two separate publications, Merkle introduced the concepts of collapse probability, which later became known as the Defect Yield [1966], and the Cascade Efficiency [1969], and these two parameters have since been used in most subsequent studies. The first of these is defined as the fraction of cascades which have collapsed to dislocation loops, and the second is the fraction of vacancies generated in a cascade which survive in the dislocation loop. The defect yield is usually determined (although not in this work) by careful measurement of the loop areal density and incident ion dose:

$$\text{Defect Yield} = \frac{\text{Areal density of loops}}{\text{Areal density of incident ions}}$$

whereas the cascade efficiency is found by obtaining the mean number of vacancies surviving in a loop (from the mean loop diameter) and comparing this with one of the modified Kinchin and Pease expressions (Section 2.3.4) for the original number of defects generated:

$$\text{Cascade Efficiency} = \frac{\text{No of vacancies surviving in loop}}{\text{No of vacancies created in cascade}}$$

Variations in ion mass and energy have been observed to produce systematic changes in both defect yield and cascade

efficiency, and a few results from the many previous studies carried out at room temperature have been selected to illustrate this. These are presented in Table 2.1. From this it is clear that:

(i) Defect yield increases with ion mass.

(ii) Defect yield increases with ion energy. (In most cases this has been observed to saturate at 1 for ion energies of 50 to 100keV).

(iii) Cascade efficiency increases with ion mass.

(iv) Cascade efficiency decreases with ion energy.

Both Eyre [1973] and Wilkins [1975] have attributed the enhanced collapse produced by heavier ions to the smaller cascades produced by such ions (as predicted by WSS: Section 2.3.3) generating a higher vacancy concentration at the cascade centre which in turn increases the "driving force" for collapse. Additionally, Wilkins suggested that the decrease in cascade efficiency observed with increasing ion energy may be attributed to the lower vacancy concentration occurring in such cascades. Such qualitative arguments, although valuable, are based on linear cascade theory and as such take no account of fluctuations in vacancy concentration within individual cascades or possible vacancy motion which may occur within the spike phase.

Another observation which may be made from the table is that the defect yields in fcc materials exceed those in bcc. The reasons for this are not yet clear although loss of perfect loops by glide from the higher stacking fault energy bcc

Target	Ion	Defect Yield	Cascade Efficiency	Reference
Cu	30keV Cu	0.50	0.36	Stathopolous 1981
	30keV W	0.60	0.71	
	10keV Au	0.25	0.50	Hausserman 1972
	20keV Au	0.40	0.40	
	70keV Au	0.90	0.25	
Ni	80keV Ni	0.44	0.25	Robinson & Jenkins 1981
	80keV W	0.81	0.28	
Mo	60keV Mo	0.16	0.27	Eyre & English 1982
	60keV Xe	0.18	0.51	
α-Fe	80kev Fe	No loops		Jenkins et al 1978
	80keV W	0.18		

Table 2.1 Defect Yields and Cascade Efficiencies in various fcc and bcc metals.

materials may play some part. However, the loop geometries observed by English et al [1977] suggest that this mechanism is not solely responsible for the difference. The observation that self-ion irradiation of α-Fe produces no resolvable loops (Table 2.1), is an interesting one which sets this material apart from others investigated.

The effect of ambient lattice temperature on the collapse process was first investigated by Howe et al [1966] who observed loops in both Au and Al at temperatures as low as 10K. More recent work [Haga et al 1983] has confirmed this observation with loops resulting in Au and Ag from ion bombardment at 10K. Such observations have led to the conclusion that cascade collapse is an athermal process although no detailed studies have yet been performed to compare low temperature defect yields with those generated at room temperature. Laupheimer et al [1981] have reported no change in defect yield between Cu specimens implanted with self-ions at both room and low temperature. However, as all observations in this work were at room temperature, the possibility of additional collapse on warming cannot be discounted. Additionally, no variation in loop size was reported over the range 6K-295K. It is interesting to note that Wilkins' explanations for the observed trends in cascade collapse (described previously) if extended, would suggest that more loops should result at lower temperatures. This is due to the longer RCS produced at low temperature (Section 2.3.3) reducing recombination, and thus enhancing vacancy concentrations and cascade collapse.

Besides vacancy loop observations, the depths of interstitial loops have been used to estimate RCS lengths in Cu [Hertel et al 1980]. These observations suggest that interstitials may be transported up to 200Å from the cascade.

(b) Ordered alloy observations.

Siegel [1949], having bombarded Cu_3Au with neutrons, was first to report disordering of an ordered alloy under irradiation, but the first attempts at examining the damage structure by TEM were performed by Seiler et al [1974]. Jenkins et al [1976] refined this technique which involves the use of superlattice reflections to image the disordered zones produced at cascade sites (Chapter Three), and have since employed it in the examination of damage produced in Cu_3Au by heavy ions, high-energy protons, fission and fusion neutrons. [Reviewed by Jenkins and English 1982]. Disordered zones were observed at the sites of individual cascades, and a detailed study of those created by Cu ions indicated that every cascade created by a knock-on of greater than 10keV produced a zone. Whether this disorder results from collective atomic motion during the spike phase, or from collisional mechanisms is as yet unclear. (This is dealt with in detail in Chapter Seven). Some indication of the structure of individual cascades is revealed from examination of the shape of disordered zones, and this has been used to identify subcascades.

The major advantage of this technique over the conventional method of TEM observation is that previously inaccessible information on cascades may obtained from the disordered zone shapes. (A full interpretation of such information does

however require a knowledge of the disordering mechanism). Additionally, defect yields may be determined independently of ion dose measurements, an advantage exploited in the current study.

Jenkins and English [1982] observed that subcascades are produced by high-energy Cu ions, but not by Au ions which were found to produce much more compact cascades, as expected from binary collision simulations and the WSS theory. However, the sizes of zones produced by high density cascades have been found to exceed that predicted by WSS, in direct contradiction to the findings of binary models. (Section 2.3.3). The limited results which are available on cascade collapse in Cu_3Au suggest that it does not differ significantly from that in pure Cu [Jenkins and Wilkins 1976].

In addition to the study recounted above, several less detailed observations have been made on other ordered systems. These include: Cu_3Pd, Fe_3Al [Laupheimer and Wilkens 1979]; Zr_3Al [Howe and Rainville 1979]; Ni_3Sn [Potter and Hernandez 1981]; Nb_3Sn [Jenkins et al 1982; Pande 1979]; and in all cases disordered zones were observed, although the atomic scattering factors (Chapter Three) are such that the contrast is not as strong as in Cu_3Au. The results in Cu_3Pd corroberate those from the Cu_3Au study as the Cu ion zones are well described by WSS, but those produced by Au ions are larger than predicted, a result attributed by the authors to disordering resulting from extensive vacancy motion during loop formation. Subcascade formation has been observed in Cu_3Pd and Fe_3Al, but not in Zr_3Al or Nb_3Sn. It has been reported

that 35keV Cu ions have produced no visible disordered zones in either Ni_3Mn or Fe_3Si [Jenkins and English 1982], although no possible reason for this observation has been suggested.

2.4.2 FIM Observations

In contrast to the TEM techniques described above, which are restricted to examining the gross spatial characteristics of cascades, field ion microscopy provides a method of examining individual cascades with atomic resolution. Early work employing the FIM was restricted to observing clusters of vacancies, but more recent use of pulsed field evaporation and sophisticated data acquisition by the group at Cornell University has allowed individual point defects to be resolved. The vacancies present within the central core of cascades may therefore be analyzed, and the structure of the so-called Depleted Zones determined [Seidman 1973]. Figure 2.9 displays a visual reconstruction of such a zone. The major drawback of such investigations is the excessive time required to acquire data on each zone, which has limited the experiments to very small zone populations.

In an attempt to determine the differences between depleted zones created by various heavy ions, [Wei et al 1981; Current et al 1983], W specimens were implanted at 10K with Ar, Cr, Cu, Kr, Mo and W ions at 30keV. The effect of ion energy was investigated by implanting Kr ions at 15, 30, 45, 60 and 70keV. The relevant observations of this study were:

(i) The number of vacancies was found to be independent

of ion mass, and increased linearly with ion energy.

(ii) The diameters of the zones were found to increase with ion energy.

(iii) Collapse of the vacancy distribution to a dislocation loop was never observed.

The fact that varying ion mass did not alter the number of defects produced is in agreement with the analytical models of defect production as the electronic losses for all ions used are similar, resulting in equal damage energies in each case. Furthermore, the changes with ion energy agree with the NRT model (Section 2.3.4) if a threshold of 52eV is adopted. Despite the increase in size with ion energy, the results demonstrate that the observed diameters are only ~40% of that predicted by WSS. The discrepancy is more pronounced at lower ion mass and higher ion energy in which cases subcascade formation was prevalent, as expected from computer models. That none of the observed cascades had collapsed is rather surprising when it is considered that the irradiation conditions employed generated Sigmund energy densities of up to ~30eV/atom. This indicates that energy density/vacancy concentration is not the only variable to be considered when studying cascade collapse.

In a further study, Pramanik and Seidman [1983] implanted W with Ag and W monatomic and diatomic ions to investigate the effect of high density cascades. The principle behind such investigations is that diatomic ions should dissociate on impact and produce two cascades which overlap both spatially

and temporally, and a comparison of the monatomic and diatomic cascades thus allows any non-linear effects to be detected. The number of vacancies created per-ion in the diatomic cascades was found to be 55% higher than in the monatomic case, clearly demonstrating the non-linearity of such cascades. Further, the diatomic zones were larger than the monatomic, indicating incomplete overlap between the separate damage regions. However, the most significant result of this work was that void-like contrast was observed in the diatomic case, but not in the monatomic, which is attributed by the authors to the agglomeration of vacancies during the spike phase of the cascade, a conclusion strongly supported by the simulations of both Guinan and Kinney [1981] and Protasov and Chudinov [1982] described above.

FIM has also been employed to study RCS lengths in W by measuring the distance separating interstitial atoms from depleted zones (measured along close-packed directions). [Wei and Seidman 1981]. The value of 160Å obtained was considered to represent an upper limit to the length of such sequences.

2.4.3 Sputtering Studies

The ejection of atoms from the surface of a solid under irradiation - sputtering - has become a useful method of investigating displacement cascade events. According to the linear cascade theory [Sigmund 1969b], the number of atoms ejected from a displacement cascade which intersects the surface of the irradiated material should be proportional to the damage energy (ie that lost through nuclear collisions).

However, measurements of heavy-ion sputtering yields (which is the number of ejected atoms per incident ion, determined by dividing the total number of ejected atoms by the number of incident ions) have suggested that this linear relationship does not describe the situation accurately. Andersen and Bay [1973] measured enhancements of over 100% in the sputtering yield per atom for diatomic bombardment relative to monatomic, demonstrating the non-linearity of the cascades. Subsequently [Anderson and Bay 1974, 1975], they were able to show that the enhancement in yield increased with deposited energy density. Merkle and Pronko [1974] suggested that the inadequacy of the linear theory might lie in its failure to account for local variations within individual cascades, which may lead to regions of energy density greatly in excess of that predicted by WSS, and this has been corroborated by a recent investigation [Merkle and Jäger 1981]. In contrast to previous studies of heavy-ion sputtering, these workers employed TEM to examine craters created by individual cascade events. Their findings were that less than one percent of all cascades created, even by diatomic Bi ions, produced a crater; but that the sizes of the craters produced suggested that ten times as many atoms as predicted may be ejected in an individual event. This was interpreted as implying that only those cascades with energetic subcascades intersecting the surface produced craters.

2.4.4 Resistivity Studies

Investigation of radiation damage by measurements of residual resistivity has confirmed both the decrease in cascade

efficiency at high energy, and the non-linearity of cascades. In a systematic attempt to determine the dependence of K, the damage efficiency (Section 2.3.4), on both ion mass and energy, Averback et al [1978] irradiated Ag and Cu with ions ranging from protons to Bi over the energy interval 20 to 855keV. The efficiency was found to decrease monatonically with increasing ion mass from 1 for protons to ~0.33 for Bi (Fig. 2.10), probably indicating increased recombination within the relaxation and cooling phases of the more dense cascades. For all masses above Ne(20), the efficiency was found to lie between 0.3 and 0.4, independent of energy. At first sight this result may appear to contradict the findings of Guinan and Kinney [1981] (Section 2.3.4), as they observed a decrease in efficiency with increasing energy. However, this is not the case as the simulation study indicated that the decrease in efficiency should occur well below 20keV, and that it should level out at approximately 0.4, as observed by the resistivity work.

Averback [1982] has confirmed the presence of spike effects, even in cases of very low Sigmund energy density ($\theta <$ 0.1ev/atom), by consecutive proton and heavy ion irradiation of Ag and Cu. The principle of these experiments is that besides damaging the specimen, the cascade irradiations anneal some of the existing Frenkel pairs. The degree of annealing and the fact that it was more pronounced at higher energy densities suggested that Frenkel pairs outwith the cascade volume were recombining as a result of energy leakage from the cascade during the spike.

Fig 2.10 Dependence of damage efficiency on ion mass. [From Averback et al 1978].

CHAPTER THREE

OBJECTIVES AND TECHNIQUES

3.1 INTRODUCTION

From the review presented in the preceding chapter, it is clear that despite the extensive interest in the phenomenon of cascade collapse, a detailed understanding has not been obtained of the mechanisms involved. The primary objective of the current study was to investigate the phenomenon in detail, considering in particular the influence of ambient lattice temperature and variations in ion energy and mass. It was hoped that this would clarify the vacancy agglomeration mechanism involved. In this chapter the individual objectives are outlined, and the principles of the experimental techniques employed to realize these are described. The details of the experiments are however, deferred until Chapter Five.

3.2 OBJECTIVES

The overall objective of the study was to identify the mechanism by which the vacancies produced in a collision cascade agglomerate to form a dislocation loop. It was decided that the best method of realizing this objective would be to irradiate Cu_3Au under a variety of conditions, and to measure the defect yield and cascade dimensions for each. The choice of Cu_3Au as the target material was dictated by the availability of the superlattice technique (Section 3.3) which

enables the disordered zones present at the sites of individual cascades to be observed. As the temperature of the ambient lattice was considered to be a possible influence on the collapse process, irradiations were performed at both liquid helium temperature (i.e. well below the onset of self diffusion in Cu_3Au [Takamura and Okuda 1973]) and at room temperature. Cascade sizes and energy densities were varied by employing ions of three different masses (Ar, Cu, Kr) and two energies (50 and 100keV). It was hoped that insight into the vacancy agglomeration mechanism would be gained by correlating any differences in defect yields and cascade dimensions observed between irradiation conditions. Additionally, as the observation of individual disordered zones is possible by the superlattice technique, it was intended to identify any systematic differences between collapsed and uncollapsed cascades within a single population. In order to fulfil these planned objectives it was essential that techniques and facilities be available to:

(a) Produce TEM specimens of Cu_3Au for irradiation, in which both disordered zones and dislocation loops show strong contrast (previously used methods were unsuitable for careful defect yield determinations).

(b) Implant these specimens with ions of varying mass and energy at room temperature, and subsequently observe the induced damage.

(c) Implant ions and observe the specimens <u>in-situ</u>, at low temperature ($T<10K$).

(d) Carefully determine the defect yield for each condition.

(e) Quantify differences in cascade sizes and shapes.

With respect to (a) above, the constraint that the TEM specimens show strong contrast for both zones and loops led to their production by vacuum evaporation. Details of the process are deferred until Chapter Four.

The room temperature irradiations were carried out on the Lintott Series 2 ion accelerator at Harwell, with subsequent observation on the JEM100B transmission electron microscope at Oxford. The low temperature irradiations and in-situ observations were performed on the HVEM-Tandem ion irradiation facility at Argonne National Laboratory. (It transpired that specimens survived the low temperature experiments so that subsequent additional examination in the JEM100B at Oxford was possible).

The method employed to determine the defect yield at each irradiation condition involved the matching of disordered zone and dislocation loop images. By determining the fraction of zones which contain loops, a direct measure of the yield is obtained.

The sizing of individual zones was initially intended to be performed on the Kontron digitizing system at Harwell, but the extent to which the data required manipulation was beyond the capabilities of the system. As a result, software was written for a Hewlett Packard digitizer-microcomputer system which had

superior control facilities.

3.3 THE SUPERLATTICE TECHNIQUE

3.3.1 The Alloy Cu_3Au

Below a critical temperature of ~390K, Cu_3Au may exist either in an ordered or a disordered state. Above this, all order is destroyed, and only the disordered phase is stable. However, by careful heat treatment (Chapter Four) it is possible to produce specimens of Cu_3Au which possess a high degree of order, and it is this property of the alloy which may be exploited in the study of radiation damage. The degree of order of the material may be represented by the classical Bragg-Williams Long Range Order Parameter, S, which is given by:

$$S=1-X/M$$

Where: X is number of copper atoms on gold sites

and: M=3/16N is the maximum number of wrongly sited copper atoms. (N being the total number of atoms in the crystal)

Thus, S=1 for a perfectly ordered lattice, and S=0 for complete disorder. The ordered phase of the alloy possesses an $L1_2$ superlattice, which is basically an fcc structure with gold atoms on the cube corners and copper atoms on the face centres, as shown in Fig. 3.1, whereas the disordered phase has a random arrangement of atoms on the fcc sites.

Even in the ordered state, disruptions to the regular arrange-

Fig 3.1 Structure of the ordered phase of Cu_3Au. Anti-phase boundaries introduce the 1/2[110] lattice shift shown.

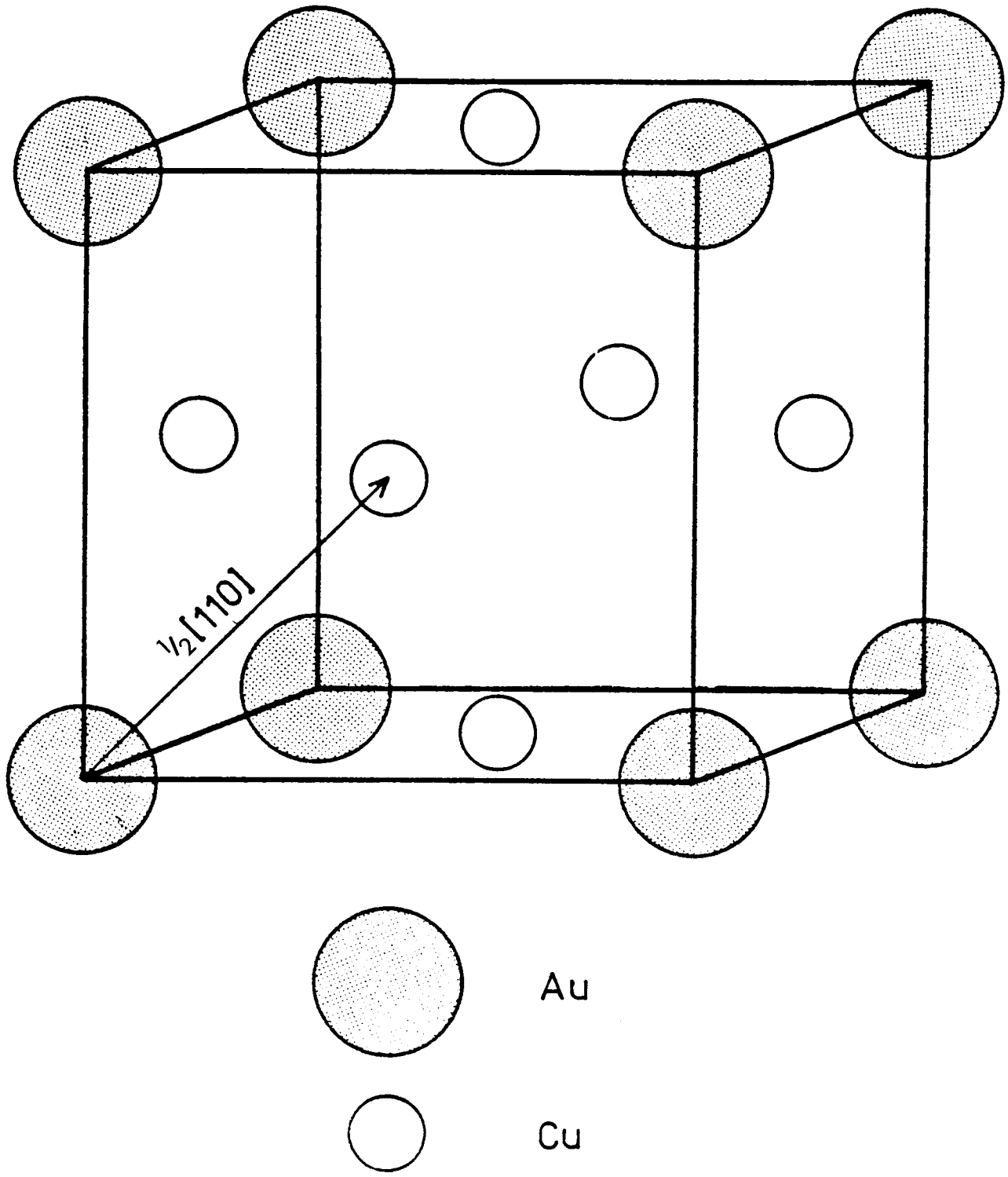
½[110]
Au
Cu

ment are common. Individually highly ordered regions may be separated by planar faults known as Antiphase Boundaries, [Fisher and Marcinkowski 1961], which introduce a shift of $\underline{R}=1/2\langle 110\rangle$ between the two regions. Examples of such faults are displayed on the transmission electron micrograph in Fig. 3.2, and show up as the dark lines against the lighter background of the ordered regions. Such faults have the effect of displacing copper atoms onto gold sites and vice versa, (as can be seen in Fig. 3.1), and are introduced at this point simply to explain their presence on the many micrographs which will subsequently be presented.

3.3.2 Disordered Zone Imaging

The amplitude of a diffracted beam from a specimen in a TEM is proportional to the "Structure Factor" F(h,k,l), of the employed reflection, where h,k and l are the Miller Indices of the atomic planes producing the diffracted beam [Hirsch et al 1965]. Normal fcc lattices are such that if h,k and l are of mixed parity, the structure factor of the reflection is zero and no diffracted beam is produced; whereas, if h,k and l are of the same parity, the structure factor is non zero and electrons are scattered into the diffracted beam. However, the ordered nature of the $L1_2$ superlattice causes departures from this behaviour and diffracted beams result even from planes of mixed Miller Indices, so-called superlattice reflections. The magnitude of the structure factor for a fundamental (h,k,l same parity) and a superlattice (h,k,l mixed parity) reflection are given by the formulae (which are derived in Appendix 3.1):

Fig 3.2 110 dark field TEM micrograph of a well ordered Cu_3Au specimen showing antiphase boundaries against lighter background. These faults lie predominantly on {100} planes and are therefore perpendicular to the plane of the foil. (The foil normals are [001] - Chapter Four)

Fig 3.3 Schematic representation of a disordered zone created at a cascade site, embedded in the ordered lattice.

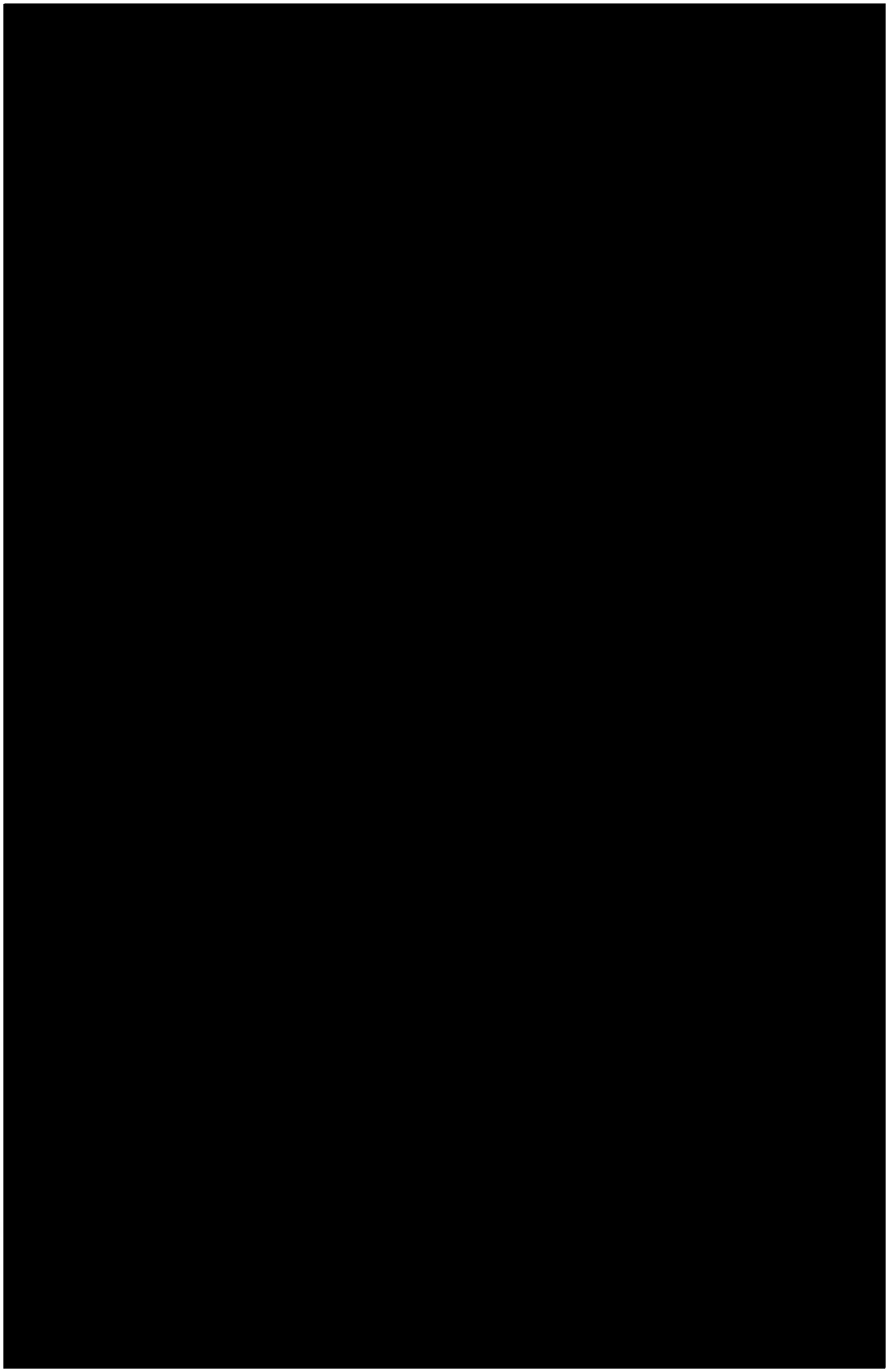

A.E.R.E. HARWELL
PHOTOGRAPHIC GROUP

HR 1527

NOT FOR PUBLICATION

$$F(h,k,l) = f_A + 3f_C \qquad \text{Fundamental}$$

$$F(h,k,l) = S\,(f_A - f_C) \qquad \text{Superlattice}$$

Where f_A and f_C are the atomic scattering factors for electrons [Hirsch et al 1965] for Au and Cu atoms respectively. From these expressions it is clear that the amplitude of a fundamental reflection is independent of the degree of order, whereas that of a superlattice reflection is proportional to S.

The neutron irradiations of Cu_3Au performed by Siegel [1949] demonstrated the occurrence of disorder within individual cascades [Seitz 1952; Brinkman 1954]. Thus, if a superlattice reflection is selected to form an image of a specimen with such locally disordered zones (Fig. 3.3), these should manifest themselves as local variations in intensity on the TEM micrographs.

Jenkins et al [1976] irradiated electropolished specimens of Cu_3Au with Cu ions in order to test this hypothesis, and found that by forming Superlattice Dark Field images the disordered zones present at cascade sites could be rendered visible as black dots against the lighter, well ordered background, provided suitable imaging conditions were employed. An example of such disordered zones from the present work is given in Fig. 3.4. By carefully determining the areal density of disordered zones, Jenkins and Wilkins [1976] were able to show that every Cu ion of over 10keV produced a resolvable zone.

Fig 3.4 A 110 dark field TEM micrograph in which disordered zones present at the sites of 50keV Kr cascades show up as the dark features. Antiphase boundaries are also visible, as is a stacking fault (Chapter Four).

Fig 3.5 Computed {110} diffracted beam intensities as a function of the thickness of ordered Cu_3Au specimens containing 10nm and 5nm slabs of completely disordered material situated at a depth of 5nm. [From Jenkins et al 1976]. It is apparent that appreciable contrast from such disordered regions will only result in thin areas of foil.

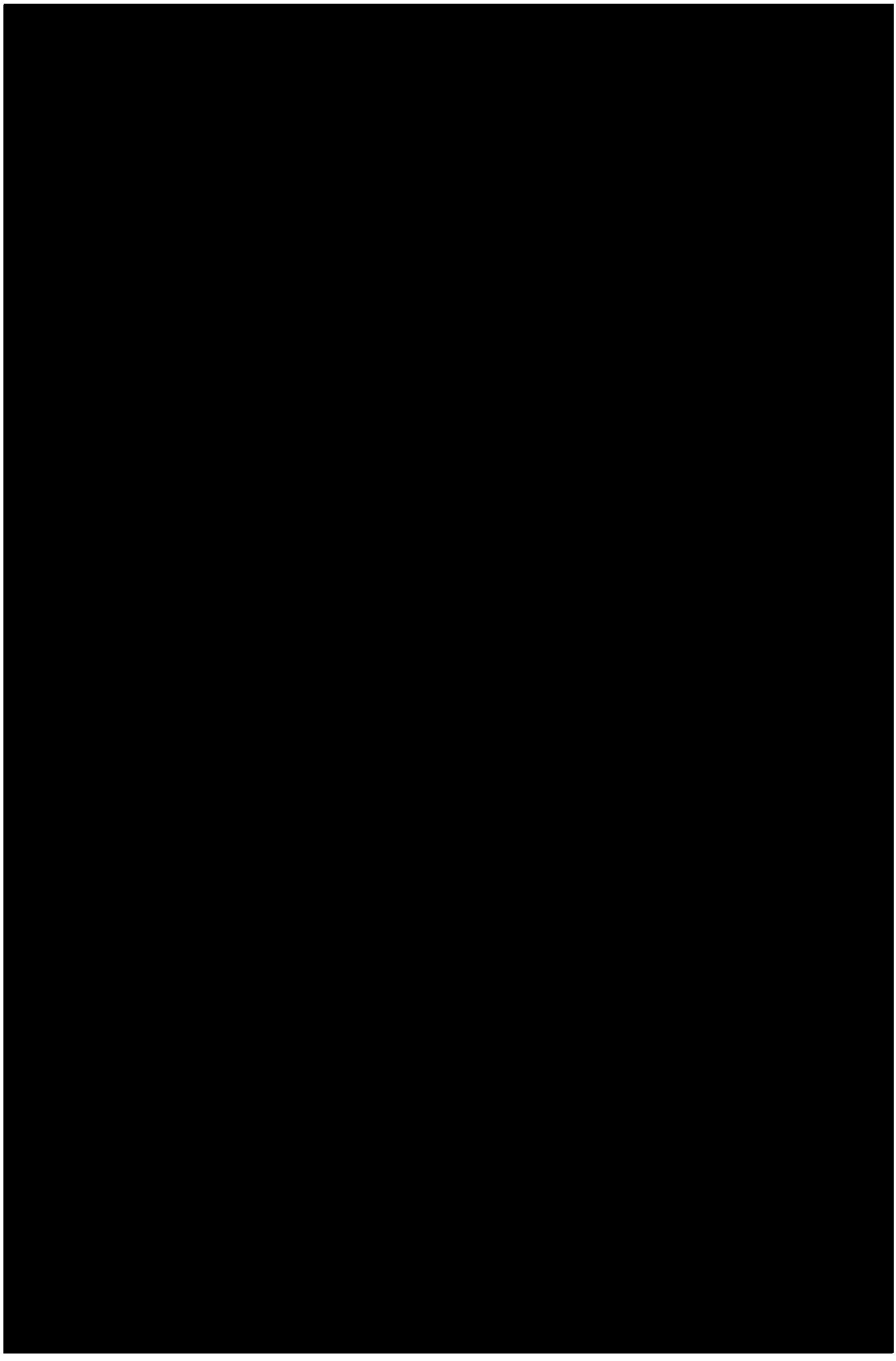

A.E.R.E. HARWELL

PHOTOGRAPHIC GROUP

HR 1524

NOT FOR PUBLICATION

By image simulation techniques, Jenkins et al [1976] were able to determine the optimum TEM imaging conditions for disordered zone observations. They found that of the superlattice reflections available, the {110} diffracted beam gave the strongest images, provided foil thicknesses of less than ~350Å were employed. Fig. 3.5 is taken from this study and shows {110} image intensities as a function of foil thickness for two zones of diameters 50 and 100Å, situated at a depth of 50Å from the upper foil surface. This illustrates that both zones should show up as dark features against the background (with the larger of the two giving stronger contrast) provided the foil thickness is less than ~400Å, but that appreciable contrast is not expected unless it is below ~300-350Å. They further determined that for an incompletely disordered zone, or imperfectly ordered lattice, reduced contrast should result. Special attention was paid in this study to the expected influence of the dislocation loops present in collapsed cascades on the disordered zone image. The conclusion drawn was that their effect should be negligible in such thin areas of foil. Because of the particular significance of this effect on the interpretation of the results of the current study, it is dealt with in more detail in Chapter Six.

The electron microscopy performed in the present study was done under the conditions recommended by Jenkins et al, i.e. {110} dark field (110DF) images of foils of less than 350Å thickness.

3.3.3 Dislocation Loop Imaging

Besides the imaging of disordered zones, the determination of defect yields also requires that dislocation loops be identified. The imaging of such features has received much attention [e.g. Rühle 1969; Jäger 1981], and image simulation by computer has been used to confirm experimental observations. More recently however, Katerbau [1976; 1981] has developed an analytical theory, based on a Bloch wave approach which accounts for the observed images.

If the diameter of a dislocation loop exceeds the extinction distance of the operating reflection ξ_g, it will be clearly resolved. However, smaller loops cannot be resolved by the diffraction contrast mechanism, and the situation is considerably more complicated in such cases. As theoretical and computer simulation treatments have been restricted to considering "two-beam" conditions (i.e. only one diffracted beam excited) most experimental studies are performed under these conditions. It is convenient at this point to follow Katerbau and distinguish between "thick" foils ($t>3\text{-}5\xi_g$) and "thin" foils ($t<2\xi_g$).

(i) Thick Foils

Under dynamical conditions ($s=0$), loop images consist of adjacent black and white lobes, provided the defect is not further than $\sim 1.5\xi_g$ from either surface. Such "black-white" images are well understood and are a result of anomalous absorption. The direction of the vector $\underline{l}$ (which points from the black to the white lobe) oscillates with defect depth, and

may be used to determine the loop nature. However, if the loop is further than ~1.5ξ_g from either surface, the white part of the image is attenuated and a "black dot" image results. (Such images are often weak and care is required to ensure visibility of small loops which are close to the centre of thick foils (Stathopolous 1981)). Similarly, if kinematical imaging conditions ($s \neq 0$) are employed, a simple black dot is observed irrespective of defect depth. This has led to such images being dubbed "kinematical".

(ii) Thin Foils

In such specimens anomalous absorption is insignificant, and black-white images are never observed, only black dots. Additionally, the reciprocal lattice spikes in the diffraction pattern from thin specimens are elongated [Hirsch et al 1965 p98], which may result in several spikes intersecting the Ewald sphere simultaneously and thus preventing the attainment of two-beam conditions. As the determination of loop burgers vectors and habit planes requires comparison of black-white images obtained under two-beam conditions with theoretical predictions, the lack of black-white images and well defined conditions in thin specimens precludes any such determination.

The restriction that very thin foils are required to image disordered zones resulted in the situation described in (ii) above applying in the present experiments. Black-white images were rarely observed and black dot, kinematical images predominated (Fig. 3.6). Additionally, two beam conditions were never attained, although this may be partially due to local foil bending (Chapter Five).

Fig 3.6 Kinematical bright field TEM micrograph showing "black-dot" images of dislocation loops created by 100keV Kr ions. In some cases subcascade formation is apparent.

A.E.R.E. HARWELL

PHOTOGRAPHIC GROUP

HR 1517

NOT FOR PUBLICATION

It is a well established result that dislocation loops in fcc materials have burgers vectors of the types $\underline{b}=a/3\langle 111\rangle$ or $\underline{b}=a/2\langle 110\rangle$, and this was also found to be the case in ion irradiated Cu_3Au by Jenkins and Wilkens [1976]. Also, Mukai and Mitchell [1982] found only the former type (Frank loops) in Cu_3Au specimens subjected to electron irradiation. A prior knowledge of these burgers vectors was important since, in general dislocations may only be imaged if the reflection employed, $\underline{g}$, and the burgers vector of the dislocation, $\underline{b}$, are such that $\underline{g}.\underline{b}\neq 0$, [Hirsch et al 1965 p169]. In view of this, it was decided that the ion implanted specimens in the present work should be imaged in $\underline{g}=\langle 220\rangle$ reflections to reveal the loops. As the specimens employed had a foil normal of $\underline{n}=[001]$, (Chapter Four), the two $\langle 220\rangle$ reflections easily accessible, (i.e. at the [001] pole), were [220] and $[2\bar{2}0]$. Table 3.1 indicates that by imaging in both of these reflections, all ten loop types which are expected to be present should be rendered visible. (As pointed out previously, it was never possible to ensure the excitation of only one diffracted beam in the present work, but this does not invalidate the conclusion that both $\langle 220\rangle$ reflections should image all loops).

Thus, loop imaging in the present study was achieved by recording dark field images employing both [220] and $[2\bar{2}0]$ reflections (ie 220DF and $2\bar{2}0$DF). Additionally, it was decided that, as in previous defect yield studies, bright field kinematical (BFK) images employing both $\langle 220\rangle$ reflections should also be recorded, (ie BFK(220) and

$\underline{b}$ / $\underline{g}$	1/2[110]	1/2[1$\bar{1}$0]	1/2[101]	1/2[10$\bar{1}$]	1/2[011]	1/2[01$\bar{1}$]
[220]	2	0	1	1	1	1
[2$\bar{2}$0]	0	2	1	1	-1	-1

$\underline{b}$ / $\underline{g}$	1/3[111]	1/3[11$\bar{1}$]	1/3[1$\bar{1}$1]	1/3[$\bar{1}$11]
[220]	4/3	4/3	0	0
[2$\bar{2}$0]	0	0	4/3	-4/3

Table 3.1 Value for $\underline{g}.\underline{b}$ for all ten loop types under both <220> reflections. $\underline{g}.\underline{b}$=0 indicates that loop is invisible in reflection.

BFK($2\bar{2}0$)) to supplement the dark field micrographs.

Jenkins and Wilkins [1976], having electropolished Cu_3Au discs for a defect yield analysis, encountered great difficulty in imaging very small loops. This was due to prominent Moirè fringe contrast on fundamental images, thought to arise from the deposition of a Au layer on the specimen surface during electropolishing. To avoid this problem, it was decided that the specimens for the present study should be produced by vacuum evaporation.

APPENDIX 3.1

The structure factor for a given reflection $\underline{g}=(h,k,l)$ is given by [Hirsch et al 1965]:

$$F = \sum_j f_j \exp\{ -2\pi i(\underline{g}.\underline{r}_j) \}$$

Where r_j is the location of the jth atom within the unit cell, and f_j is its atomic scattering factor for electrons. Given that the atomic locations of the four atoms within the unit cell in an Fcc lattice are (0,0,0); (1/2,1/2,0); (1/2,0,1/2); (0,1/2,1/2); this becomes:

$$F = f_1 + f_2 \exp\{ -2\pi i(h/2 + k/2) \} + f_3 \exp\{ -2\pi i(h/2 + l/2) \}$$
$$+ f_4 \exp\{ -2\pi i(k/2 + l/2) \}.$$

In the case of a fundamental reflection (h,k, and l of the same parity), all three exponential factors must be unity. Thus, the structure factor is simply the sum of the atomic scattering factors within the unit cell. The stoichiometry of Cu_3Au means that, on average 3 of the 4 atoms in the unit cell will be Cu, and 1 will be Au. Thus,the structure factor for a fundamental reflection is simply,

$$F = f_A + 3f_C$$

Where f_A and f_C are the atomic scattering factors of Au and Cu atoms respectively. The case of superlattice reflections is however, more complicated. With h,k and l of mixed parity, two of the three exponential factors must be -1, with the remaining factor being +1. Thus, the structure factor may be written:

$$F = f_1 + f_2 - f_3 - f_4$$

Again, the stoichiometry of Cu_3Au simplifies this as three of the four atomic scattering factors must be identical. Thus the expression reduces to,

$$F = f_1 - f_2$$

Where the subscripts now refer to any two of the four sites in the unit cell). Now, the atomic scattering factor of site 1 is that of a Cu atom multiplied by the probability that the site is occupied by such an atom, added to that for Au. i.e.

$$F = (p_{C_1} f_C + p_{A_1} f_A) - (p_{C_2} f_C + p_{A_2} f_A)$$

Where p_{C_1} is the probability that site 1 is occupied by a Cu atom etc. These probabilities must now be expressed in terms of the long range order parameter S, which is given by:

$$S = 1 - X/M$$

Where X is the number of Cu atoms situated on Au sites, and M = 3N/16 with N being the maximum number of wrongly sited Cu

atoms. S may therefore be given by:

$$S = 1 - 16X/3N$$

The probability that a Cu atom occupies a Au site must be given by the total number of Cu atoms, divided by number of Au sites, if the atoms are arranged randomly. i.e.

$$p_{C_1} = X/N/4 = 4X/N$$

Similarly, the probability that a Au atom occupies a Au site is:

$$p_{A_1} = 1 - 4X/N$$

and that a Cu atom occupies a Cu site is:

$$p_{C_2} = 1 - 4X/3N$$

and that a Au atom occupies a Cu site:

$$p_{A_2} = 4X/3N$$

Substituting these four probabilities into the expression for F yields:

$$F = \{ 4X/N\ f_C + (1-4X/N)\ f_A \} - \{ (1-4X/3N)\ f_C + 4X/3N\ f_A \}$$

Some simple algebraic manipulation gives the result:

$$F = S (f_A - f_C)$$

for the structure factor of a superlattice reflection in Cu_3Au.

CHAPTER FOUR

SPECIMEN PREPARATION

4.1 INTRODUCTION

As outlined in the preceding chapter, electropolished foils of Cu_3Au had the major drawback that images employed for dislocation loop imaging were rarely of a sufficiently high quality for careful defect yield determinations to be made. For this reason, evaporated thin films of Cu_3Au were produced in order that the quality of fundamental images could be improved. For such films to produce TEM specimens which were suitable for defect yield measurements, they had to be highly continuous but with a thickness of less than 35nm. Additional requirements included a high degree of long range order with large antiphase domain sizes (~100nm), which of course cannot be obtained unless the stoichiometry is correct. Further useful attributes for such specimens are a low dislocation density and large areas free from local bending. In order to obtain the high degree of order and large antiphase domain sizes desired, a careful heat treatment was employed subsequent to the evaporation. The production of vacuum evaporated Cu_3Au films had been successfully attempted prior to the start of this work by Yamaguchi et al [1961]. However, the technique employed, namely co-deposition (see below), led to the production of films which possessed very few of the requirements listed previously. For this reason, it was necessary to develop a new technique of Cu_3Au film production.

4.2 EQUIPMENT AND PROCEDURE

An Edwards 306 vacuum evaporation system was employed to produce the specimens and is shown schematically in Fig 4.1(a),(b). The salient features are:

(i) A vacuum chamber and pumping system capable of pressures $<10^{-6}$ Torr;

(ii) Material to be evaporated - the evaporant;

(iii) Evaporation boat or spiral for containing evaporant;

(iv) Substrate, onto which evaporant is deposited;

(v) Current source for heating boat;

(vi) Current source for heating substrate;

(vii) Shutter for substrate shielding.

In essence, the procedure is a simple one. Evacuation of the chamber to $\sim 10^{-6}$ Torr is followed by heating of the evaporant to a temperature at which it can evaporate onto the substrate, thus producing the desired thin film.

4.3 THEORETICAL CONSIDERATIONS

4.3.1 The Evaporation

Evaporation of a material will only proceed at a significant rate if its vapour pressure, at the temperature of interest, is appreciably higher than the ambient pressure. The lowest pressures which could be obtained by the Edwards system, in a reasonable time, were $\sim 10^{-6}$ Torr. This means that vapour pressures at the source must be $\sim 10^{-2}$ Torr if the evaporation is to proceed at a rate such that contamination of

Fig 4.1(a) Schematic representation of pumping system for vacuum chamber. The rotary pump allows roughing to a vacuum of ~10^{-2} Torr, with further evacuation to ~10^{-6} Torr facilitated by the diffusion pump on the backing line.

Fig 4.1(b) Schematic representation of vacuum chamber showing geometry of the evaporations.

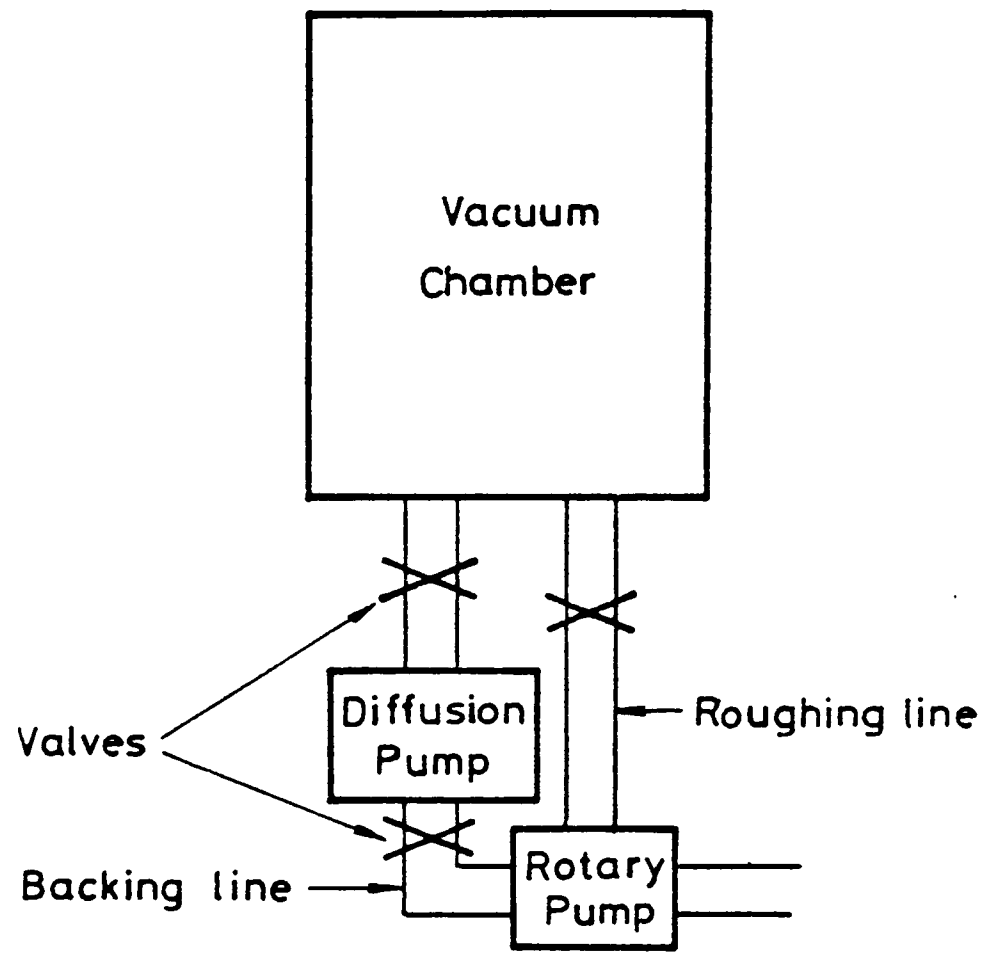
Vacuum
Chamber
Valves
Diffusion
Pump
Roughing line
Backing line
Rotary
Pump

(a)

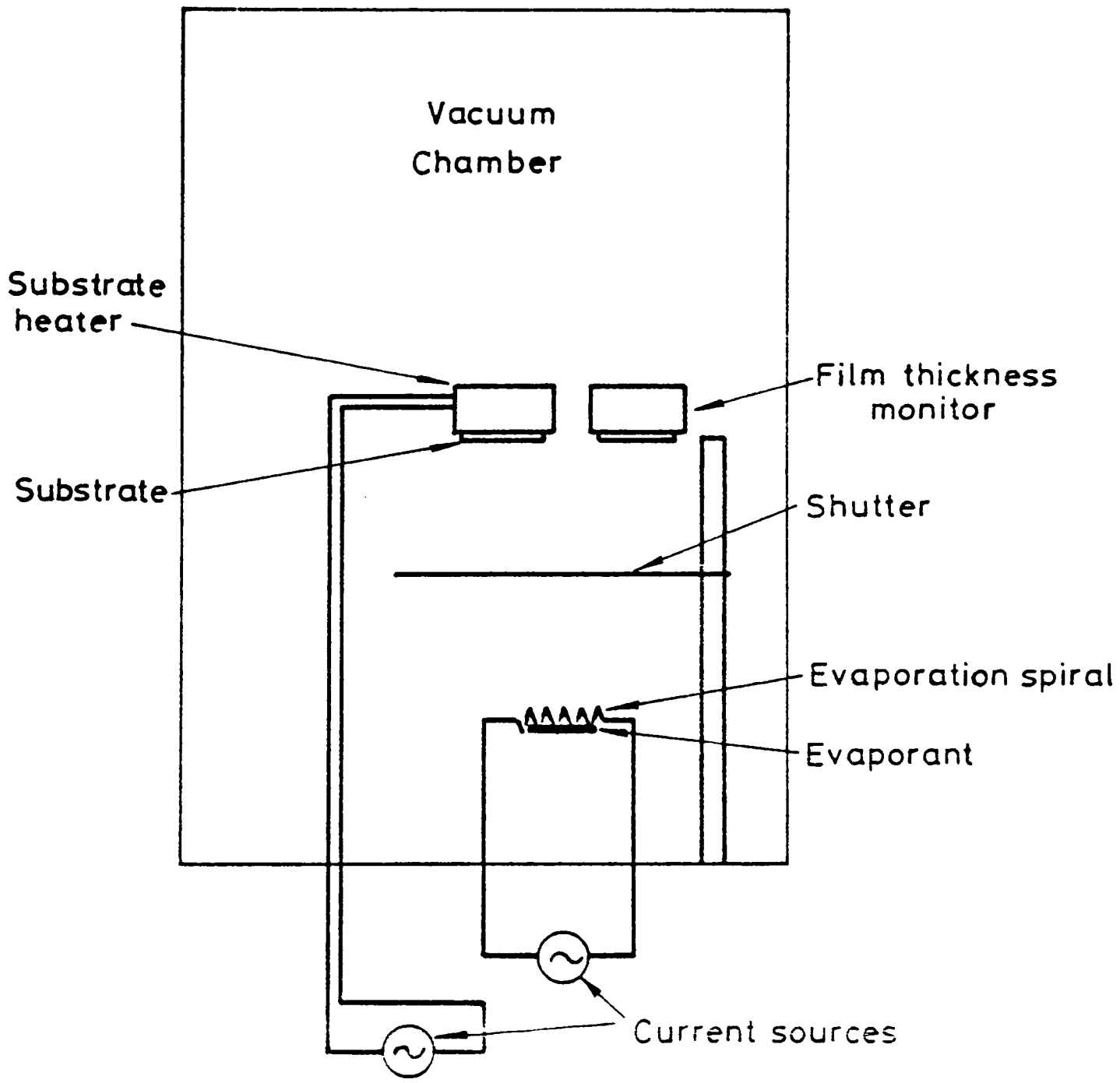
Vacuum
Chamber
Substrate
heater
Film thickness
monitor
Substrate
Shutter
Evaporation spiral
Evaporant
Current sources

(b)

the film by the remaining air in the system is to be kept to a minimum [Brodie and Muray 1982]. However, it should be noted that if the evaporation rate becomes excessively high, erratic evaporation may occur resulting in poor quality films. For most metals (with the notable exceptions of the refractory metals), such vapour pressures are achieved at temperatures in the range 500<T<2000K, as illustrated by Table 4.1. If the metal is such that it achieves a sufficiently high vapour pressure at temperatures at which it is still solid, heating may be accomplished by simply passing an electic current through the solid evaporant and subliming it (e.g. Zn, Mn). It is however more common that metals melt before their vapour pressures reach ~10^{-2} Torr and evaporation from the liquid phase was carried out. This method involves placing the evaporant in a holder of another metal which only achieves high vapour pressures at greatly increased temperatures. For this reason refractory metals are usually used (e.g. W, Mo). By resistive heating of the refractory boat or spiral, the evaporant may be melted and subsequently evaporated. This method was employed to produce the films used in the current work, with a tungsten spiral serving as the evaporant holder.

The production of binary alloy films is somewhat more complicated than the single species case described above. Depending on the individual constituents, one of two methods is used:

(i) Evaporation of the bulk alloy;

(ii) Codeposition of the two components from separate

TABLE 4.1 Temperatures at which vapour pressure reaches 0.01 Torr for various elements [From Powell et al 1966 p224].

sources.

The former is generally favoured due to its simplicity although the preservation of stoichiometry dictates that the two constituent elements must have similar evaporation rates, i.e. similar vapour pressures at the temperature of evaporation. If this condition is not met, stoichiometric films can only be produced by the second method with each source at the correct temperature for the element. Since evaporation rates depend exponentially on temperature, very precise control is required. Fortunately, Cu and Au do share similar vapour pressures over the temperature range of interest (Table 4.1) and evaporation from the bulk alloy was possible.

4.3.2 Film Nucleation and Growth

Although it is understood in a qualitative sense, a detailed understanding of thin film nucleation and growth has not yet been achieved. However the important stages in the process have been identified and are recognised to be [Brodie and Muray 1982 P259]:

(i) Evaporant particle adsorption;

(ii) Production of small nuclei (~0.5nm);

(iii) Growth of nuclei;

(iv) Coalescence of nuclei.

Once the evaporant particle has been adsorbed onto the substrate surface it migrates until its energy decreases sufficiently for it to be trapped at a nucleation site

(usually a surface irregularity). Nuclei thus formed, grow into three dimensional islands of varying orientation. When two islands coalesce, the smaller will usually reorientate itself to accommodate the larger, provided the substrate temperature is high enough for this process to occur. Obviously a high nucleation density favours the coalescence of smaller islands, increasing the probability of reorientation, and thus of single crystal films. This process, not surprisingly, is heavily dependent on the substrate characteristics. If single crystal films are desired, the substrate should also be a single crystal with a low dislocation density since substrate dislocations tend to be mirrored in the film. If the evaporant is an f.c.c. metal, alkali-halide crystals are favoured.

4.4 SPECIMEN-PRODUCTION

4.4.1 Evaporation

Bulk Cu_3Au was produced by melting 99.999% pure Cu and Au (50.82 wt%) in an inert atmosphere. Repeated rolling followed by 900°C anneals resulted in the production of 0.1mm thick foils, from which thin strips were cut for evaporation.

The evaporations were carried out in a standard Edwards 306 evaporator employing a rotary backed diffusion pump system capable of 10^{-7} Torr but more commonly evacuated to $\sim 10^{-6}$ Torr. The basic system was modified by Dr C.R.M. Grovenor to incorporate a substrate heating facility which employed radiation heating from a high intensity light bulb, allowing substrate temperatures of ~400°C to be reached. Fig 4.1(b) is

a close up view of the source-substrate system. The shutter shown in the figure was used to shield the substrate from the early stages of deposition when the evaporation rate is very low. It was removed after the Cu_3Au had melted ensuring a high deposition rate and thus the coalescence of smaller islands. Early evaporations in which the shutter was not used often resulted in films of a polycrystalline nature.

To ensure that films of the correct thickness (t~30nm) were laid, an Edwards FTM2 film thickness monitor was employed. This instrument uses two quartz crystals oscillating at ~6MHz. One crystal is placed in the evaporation chamber close to the substrate and the other is used as a reference crystal. During the laying of the film, the resonant frequency of the first crystal decreases as its mass increases due to the deposit. The monitor uses this change in frequency, coupled with the deposit's density to give a thickness readout.

If highly accurate film thicknesses are required, some method of independent calibration must be used, such as X-ray absorption. However, in this case such accuracy was not thought necessary and a simple geometric determination was used. Assuming that the evaporation proceeds in a spherically symmetric manner the following relationship holds:

$$4\pi r_m^2 t_m = 4\pi r_s^2 t_s$$

Where: r_m = source - monitor distance

r_s = source - substrate distance

t_m = film thickness at monitor

t_s = film thickness at substrate

Since $4\pi r^2 t$ is the volume of a spherical shell of thickness t at distance r from the sphere's centre.

So that:
$$t_s = \left[\frac{r_m}{r_s}\right]^2 t_m$$

With r_m and r_s being 79mm and 54mm respectively, films of measured thickness t_m~14nm - 16nm, produced films of true thickness t_s ~30nm.

This relationship was found to give satisfactory results in that films laid in this manner produced strong disordered zone contrast.

Although individual evaporations varied in detail, the following procedure was generally adhered to:

(i) The vacuum chamber was evacuated and the W spiral outgassed at T>2000K for 1 minute.

(ii) An NaCl substrate was cleaved with a surface normal of $\underline{n}$ = <001>. This was subsequently washed in distilled water to remove any gross surface irregularities.

(iii) Having allowed the spiral to cool, the Cu_3Au strip and NaCl substrate were positioned as shown in Fig 4.1(b).

(iv) After re-evacuation to ~10^{-6} Torr, the substrate was heated to 250°C and held there for one hour.

(v) A current of ~20A (at 30V) was passed through the

tungsten spiral until the Cu_3Au melted. At this point the current was increased and the shutter removed.

(vi) Once the correct reading was achieved on the foil thickness monitor the shutter was replaced and the boat and substrate currents switched off.

(vii) After about 2 hours, the substrate and film were removed from the chamber.

In an attempt to improve specimen quality, many variations on the above procedure were used, the most notable of which were: changing substrate temperature over the range 200°C to 300°C in 20°C intervals, changing deposition rate from ~5Ås^{-1} to 100Ås^{-1} (measured by the film thickness monitor), using unwashed substrates and neglecting to outgas filament. However, these changes either had no effect or degraded film quality.

4.4.2 Ordering

As explained in Chapter Three, a perfectly ordered superlattice will possess a Bragg-Williams long range order parameter of S=1. However, as pointed out in Section 4.1, the antiphase domain size is of critical importance for the successful application of the superlattice technique. Previous authors [Fisher and Marcinkowski 1961] have demonstrated that ordering procedures which lead to specimens of perfect order do not necessarily produce large domain sizes. Ordering procedures in which the specimen is held at ~380°C,

just below the order-disorder transition temperature for prolonged periods (~75 hours) result in less than perfect order (S~0.8) but very large antiphase domain sizes (~100nm). In contrast, a slow cool (~2-3°C/hour) through the order-disorder temperature to about 200°C results in effectively perfect order with antiphase domain sizes reduced to ~50nm.

In an attempt to produce large domains with as high a degree of order as possible, an ordering sequence which combines the above two was employed. Specimens were raised to ~450°C in a vacuum of $\sim 10^{-7}$ Torr and cooled to ~380°C over two hours. Having been held at this temperature for ~50 hours, they were then cooled at a rate of ~5°C per hour to room temperature.

4.5 SPECIMENS PRODUCED

On removal from the vacuum furnace the films were scored by a razor blade into squares of about $2mm^2$. The NaCl substrate was then dissolved in distilled water in such a manner that the Cu_3Au squares floated onto the surface. From there they were scooped onto 3mm, 400 mesh copper grids, thus producing specimens suitable for TEM. Such a specimen is shown in Fig 4.2. The foil normal is <001> and antiphase domain sizes in excess of 100nm are common. The long straight features are stacking faults with displacement vectors $\underline{R}$ = 1/6<112> or 1/3<112>. (It proved impossible to distinguish these due to problems associated with achieving two beam conditions in the thin films; see Chapter Five.) In some cases, the density of these faults became very high indeed, Fig 4.3. Although it was not explicitly measured, the long range order parameter is

Fig 4.2 A 110 dark field TEM micrograph showing an area of a good quality film. Antiphase domains of 100nm are common, and the long range order parameter is estimated at S~0.8. The straight features are stacking faults (see text).

Fig 4.3 Area of foil with exceptionally high density of stacking faults.

[redacted]

A.E.R.E. HARWELL
PHOTOGRAPHIC GROUP

HR 1508

NOT FOR PUBLICATION

thought to be at least 0.8 due to the ordering procedure used [Fisher and Marcinkowski 1961]. The relative concentrations of Cu and Au were measured by a CAMEBAX microprobe and were found to be consistent with a stoichiometry of Cu_3Au.

Perhaps the most surprising aspect of this method of specimen production is the variability in quality obtained. Not only did evaporations of nominally the same characteristics result in widely differing foils, but variation across a single substrate and even across a TEM specimen were often observed. However, a good specimen produced by this method (Fig 4.2) is of considerably better surface quality than that which can be achieved by electropolishing techniques. Significantly, the images obtained by exciting a fundamental reflection were almost completely free of Moirè fringes.

Of the fifty or so evaporations carried out, specimens from only six were irradiated and only three of these contribute to the results discussed in this work. Despite this low success rate, the excellent quality of the better specimens produced is sufficient to justify the technique.

Deterioration of the specimens in air was initially so slow that none was thought to occur. However, after surprisingly long times (~1 year) a fairly rapid deterioration occurred rendering specimens useless. An example of this is shown in Fig 4.4.

Fig 4.4 110 dark field micrograph showing foil contamination, which precluded the use of such foils.

A.E.R.E. HARWELL
PHOTOGRAPHIC GROUP

HR 1507

NOT FOR PUBLICATION

CHAPTER FIVE

EXPERIMENTAL TECHNIQUES

5.1 INTRODUCTION

Specimens prepared by the technique described in the preceding chapter were irradiated under six different irradiation conditions (50keV and 100keV Ar, Cu, Kr) both at low temperature and at room temperature. As described in Chapter Three, the object of this was to allow determinination of the defect yield in each case, and to attempt an explanation of any differences which may be found between the various cases by examining the cascades produced under each condition. In particular, it was hoped to determine whether cascade collapse occurs at low temperature in Cu_3Au and if so, if it differs in any way from that which occurs at room temperature.

In this chapter, the details of the electron microscopy performed on both the low temperature irradiated (LTI) and room temperature irradiated (RTI) specimens is recounted, with particular attention paid to the various effects which may influence disordered zone and dislocation loop imaging.

The defect yields for all twelve irradiation conditions were obtained by a careful comparison of superlattice and fundamental images and the details of this procedure are also recounted. Finally, in an attempt to explain the defect yield observations, the disordered zones in each case were sized by a semi-automatic digitizer and the procedure

followed, along with the computer software written for the purpose, is presented.

5.2 IRRADIATIONS

5.2.1 Low Temperature Irradiations

The low temperature irradiations were performed on the HVEM-Tandem facility at Argonne National Laboratory. This unique system permits in-situ ion irradiation of specimens mounted in a Kratos HVEM. In the present study, a Texas Nuclear 300keV ion accelerator was employed although the Tandem accelerator allows ion energies of up to 8MeV to be attained. The system is schematically represented in Fig 5.1. Ions leave the accelerator and are electrostatically deflected through the specially designed ion beam interface onto the specimen in the HVEM. (Electrostatic deflection is employed in preference to magnetic deflection in order that interference with the microscope be minimized.) If normal incidence of the ion beam is desired - as in the present work - the specimen must be tilted by 33° prior to irradiation. By means of the ion pump shown in Fig 5.1, the ion beam line is maintained at a vacuum of $\sim 10^{-10}$ Torr, although that in the specimen area is only $\sim 10^{-6}$ - 10^{-5} Torr.

As pointed out in Chapter Three, the superlattice technique is capable of measuring defect yields without ion doses being carefully determined. However, the dosimetry system (Fig 5.2) was employed to ensure that doses were $\sim 10^{11}$ ions cm^{-2}. This system, described by Taylor et al [1981], employs a skim cup which measures the ion beam current by stopping a circular

Fig 5.1 Schematic of HVEM-Tandem facility at Argonne National Laboratory. (See text).

Fig 5.2 Ion beam dosimetry system on HVEM-Tandem facility. (See text).

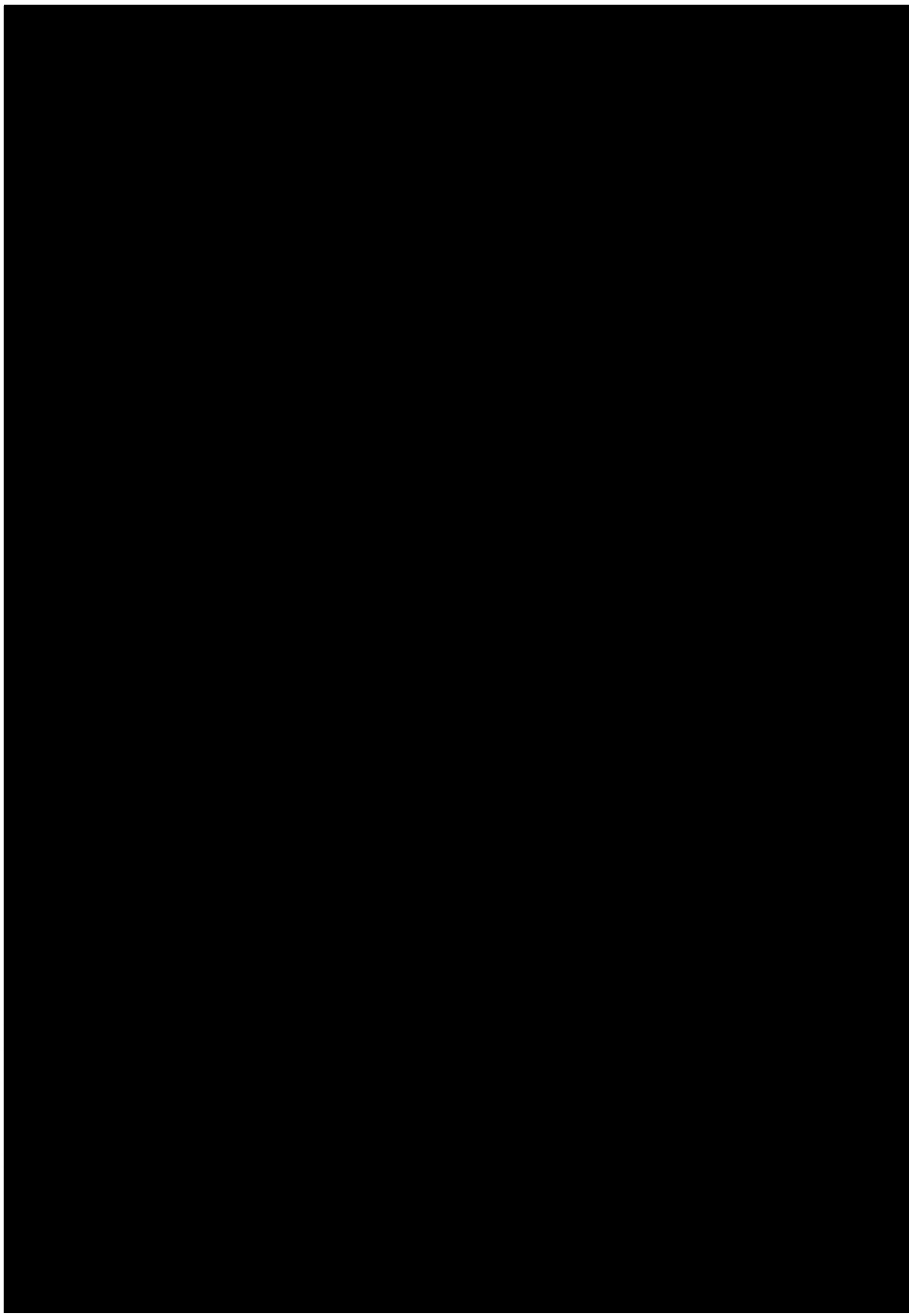

A.E.R.E. HARWELL
PHOTOGRAPHIC GROUP

HR 1519

NOT FOR PUBLICATION

section of the beam. The sector plate and 3mm aperture shown in the figure allow centring of the beam and ensure a circular cross section. The 2mm aperture on the skim cup stops a 0.5mm thick annular ring of the beam and integration of the stopped charge gives the accumulated dose. Calibration of this system is achieved by placing a Faraday cup in the specimen position. This cup is screened to reduce the effect of secondary electron emission. If homogeneous irradiation is essential, a beam scanning system may be employed, although in the present work this was not used and no great variation in dose across the 2mm beam diameter was apparent from the observed disordered zone areal densities.

By mounting the specimens in a liquid helium cooled specimen stage, shown in Fig 5.3 (details of which are given by King [1980]), it was possible to irradiate and observe at temperatures as low as 8K. Temperature monitoring was achieved by means of a platinum resistance thermometer which had been calibrated by the manufacturer (Rosemont Inc.) at four fixed points, and employing polynomial interpolation. It is expected that an accuracy of ±1K should be easily attainable by attaching the thermometer to the specimen block (Fig.5.3(b)). A soft indium ring was used to firmly secure the specimen in order to ensure good thermal contact between it and the block.

Irradiations were performed with 50keV and 100keV ions of Argon, Copper and Krypton (for isotopes used, see Table 5.1) all to nominal doses of $\sim 10^{11}$ ions cm^{-2}. In practice, the ion dose varied somewhat, due largely to errors in the timing of irradiations which lasted typically 10s, and the true doses

Fig 5.3(a) Liquid helium cooled specimen stage employed for low temperature irradiations.

Fig 5.3(b) Close-up of specimen area on stage showing connections to platinum resistance thermometer. The indium ring used to secure the specimen is also visible.

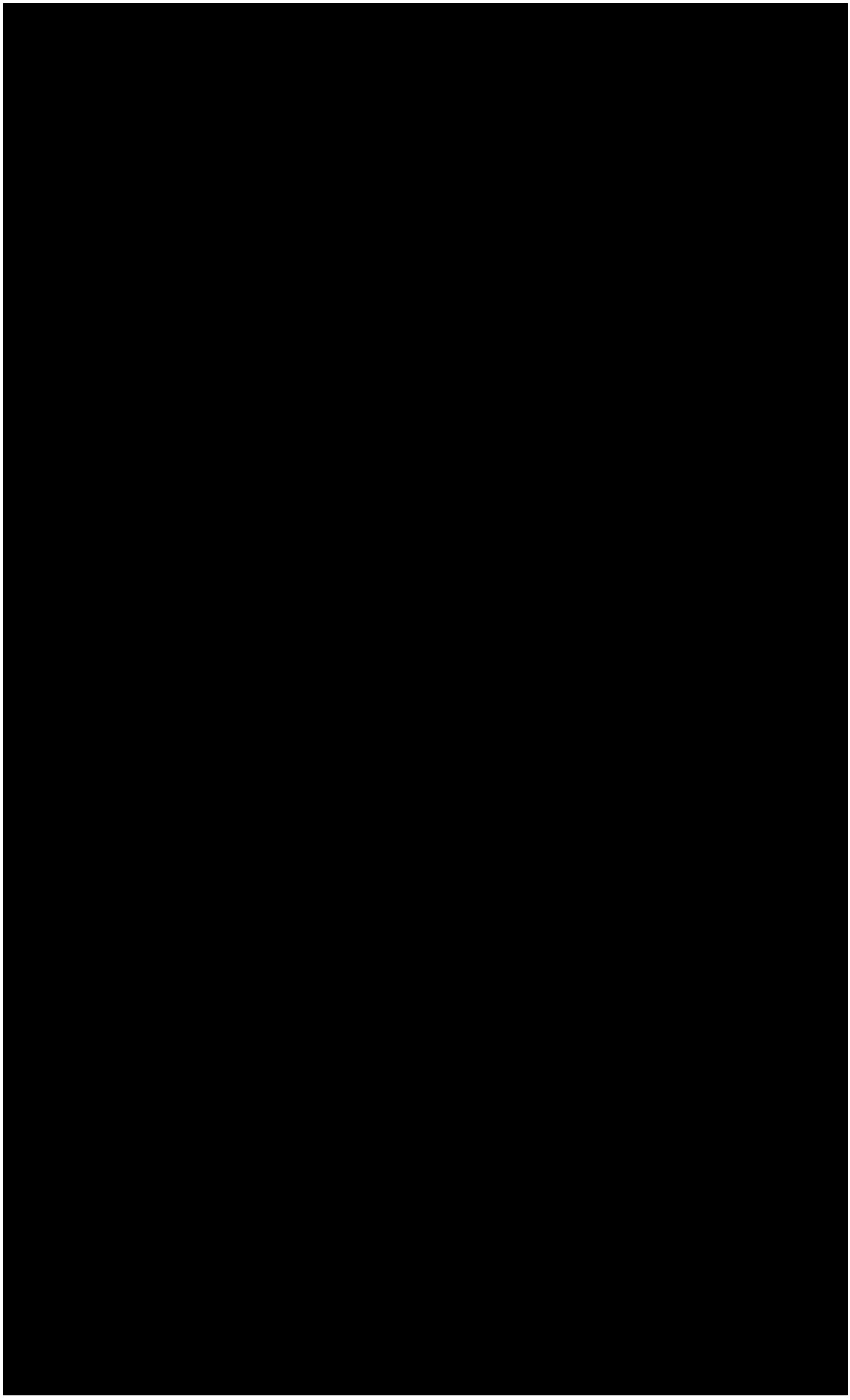

A.E.R.E. HARWELL
PHOTOGRAPHIC GROUP

HR 1526

NOT FOR PUBLICATION

Ion	Atomic No. Z	Atomic Mass A	Energy (keV)	Dose at Room Temp $x10^{10}$ ions cm^{-2}	Dose at Low Temp $x10^{10}$ ions cm^{-2}
Argon	18	40	50	9	
			100	6	5
Copper	29	63	50	5	7
			100	6	15
Krypton	36	84	50	8	13
			100	6	6

Table 5.1 Irradiation conditions used, with doses both for room and low temperature irradiations.

(as measured by disordered zone areal density) are given in Table 5.1. Prior to irradiation, specimens were cooled to ~8K at a rate of ~15°C min^{-1}. It was found that the residual gases in the microscope column condensed onto the specimen and began to affect electron transmission after about 15-20 minutes. In an attempt to minimise this effect, irradiations were carried out as soon as possible after reaching 8K, and the specimen was weakly illuminated throughout the cooling procedure. This was observed to retard the rate of condensation, presumably due to re-evaporation of the gases by the electron beam. This specimen contamination was usually the limiting factor which determined the extent of the low temperature analysis. Subsequent to irradiation, the electron microscopy described in Section 5.3 was performed with the specimen being maintained at ~8K at all times.

5.2.2 Room Temperature Irradiations

Room temperature irradiations were carried out using the Lintott Series 2 ion implanter at Harwell which is specifically designed for semiconductor wafer doping, and therefore has a large beam area at the specimen (30 x 5mm). Additionally, the required dose is implanted by rotating the specimen through the beam the appropriate number of times for the operating beam current. The irradiation conditions were as for the low temperature irradiations, i.e. Argon, Copper and Krypton ions at 50keV and 100keV. As the source voltage on this implanter has a maximum setting of 80keV, post-acceleration was required for the higher energy conditions.

The vacuum in the specimen chamber was between 10^{-6} -10^{-5} Torr. Ion beam dosimetry was achieved by using a pico-ammeter to measure the total beam current striking the specimen-mounting plate and by automatically terminating the irradiation once the accumulated dose reached ~10^{11} ions cm^{-2}, which usually required about 50 passes. Again, actual doses obtained are given in Table 5.1.

5.3 ELECTRON MICROSCOPY

The electron microscopy in the present study was carried out on two instruments; the Argonne HVEM and the Oxford JEM100B. The specimens irradiated at room temperature were examined only in the latter, whereas those irradiated at low temperature were examined in both, under a total of three different conditions:

(i) At low temperature, immediately after irradiation, in the HVEM.

(ii) Subsequent to warming to room temperature, in the HVEM.

(iii) After transportation back to Oxford, in the JEM 100B.

All micrographs recorded on the HVEM were taken at a nominal magnification of 50,000 times, whereas those on the JEM100B were at 60,000. As electrons of energy greater than 325keV are capable of displacing atoms in Cu_3Au [Hameed et al 1982] and thus producing additional unwanted radiation damage, all microscopy performed with the HVEM employed an accelerating

potential of 300keV, below the damage threshold. The Oxford instrument was operated at its maximum voltage of 100keV.

A problem encountered with the HVEM analyses was that the liquid helium cooled specimen stage employed could only be tilted about one axis, up to an angle of $\pm 60^{\circ}$. In view of the discussion presented in Chapter Three, it is clear that such a "single tilt" restriction, which prevents the excitation of both <220> reflections, must result in failure to image some of the loops present in a given area.

The procedure employed for the analysis of irradiated specimens was essentially the same on both instruments. As large an area as possible was excited in a 110DF reflection (at the [001] pole) and several such micrographs recorded to reveal the disordered zones. Subsequent recording of the same area in both 220DF and bright field kinematical (BFK(220)) reflections allowed the loops present at some disordered zone sites to be imaged (Chapter Three). As the JEM100B possessed a double tilting facility, the experiments performed on this instrument also used the orthogonal systematic reflections $1\bar{1}0$DF, $2\bar{2}0$DF and BFK($2\bar{2}0$) in order that all loops be rendered visible. In a typical experiment on the JEM100B between forty and sixty micrographs were taken, although at Argonne time constraints restricted this to about twenty.

It had initially been hoped that the same areas of foil would be analysed both at low temperature and at room temperature although it transpired that this was impossible. Warming of the foil resulted in extensive bending such that the flat

areas selected at low temperature were invariably deformed, and new areas had to be selected.

To illustrate the type of micrograph obtained, some of those from the JEM100B experiment performed on the 50keV Cu LTI specimen are shown in Fig 5.4. It is clear from these that bending of the foil on a local scale results in several 220DF images being required to ensure that the entire area of interest is excited exactly at the Bragg condition. A consequence of this is that the area is also excited with positive ($s>0$) and negative ($s<0$) deviations from the dynamical condition, although the extent of the bending makes it meaningless to assign a single s value to the image. A similar procedure is followed for the kinematical bright field images with sufficient micrographs being taken to ensure that the entire area is recorded both with $s>0$ and $s<0$ BFK(220) images. As shown in the figure, the process is then repeated with the other systematic row. The diffraction pattern shown is typical, and clearly illustrates that more than a single reflection is operating. This departure from two-beam conditions is a consequence of both the local bending, and the elongation of reciprocal lattice spikes (Chapter Three). This "many beam" situation has been identified by Hertel [1979] as being most suitable for the imaging of small loops, since with several diffraction vectors operating, $\underline{g}.\underline{b}=0$ will only occur in exceptional cases. It might be expected therefore that in the HVEM single-tilt experiments, a higher proportion of loops will be visible than suggested by the two beam considerations of Chapter Three.

Fig 5.4 Low magnification micrographs taken from the 50keV Cu LTI experiment performed on the JEM100B. The extent to which local specimen bending affected the diffraction conditions is apparent.

(a)	110DF
(b), (c), (d)	220DF
(e), (f), (g), (h)	BFK(220)
(i), (j), (k), (l)	$2\bar{2}$0DF
(m), (n), (o)	BFK($2\bar{2}$0)
(p)	Diffraction pattern

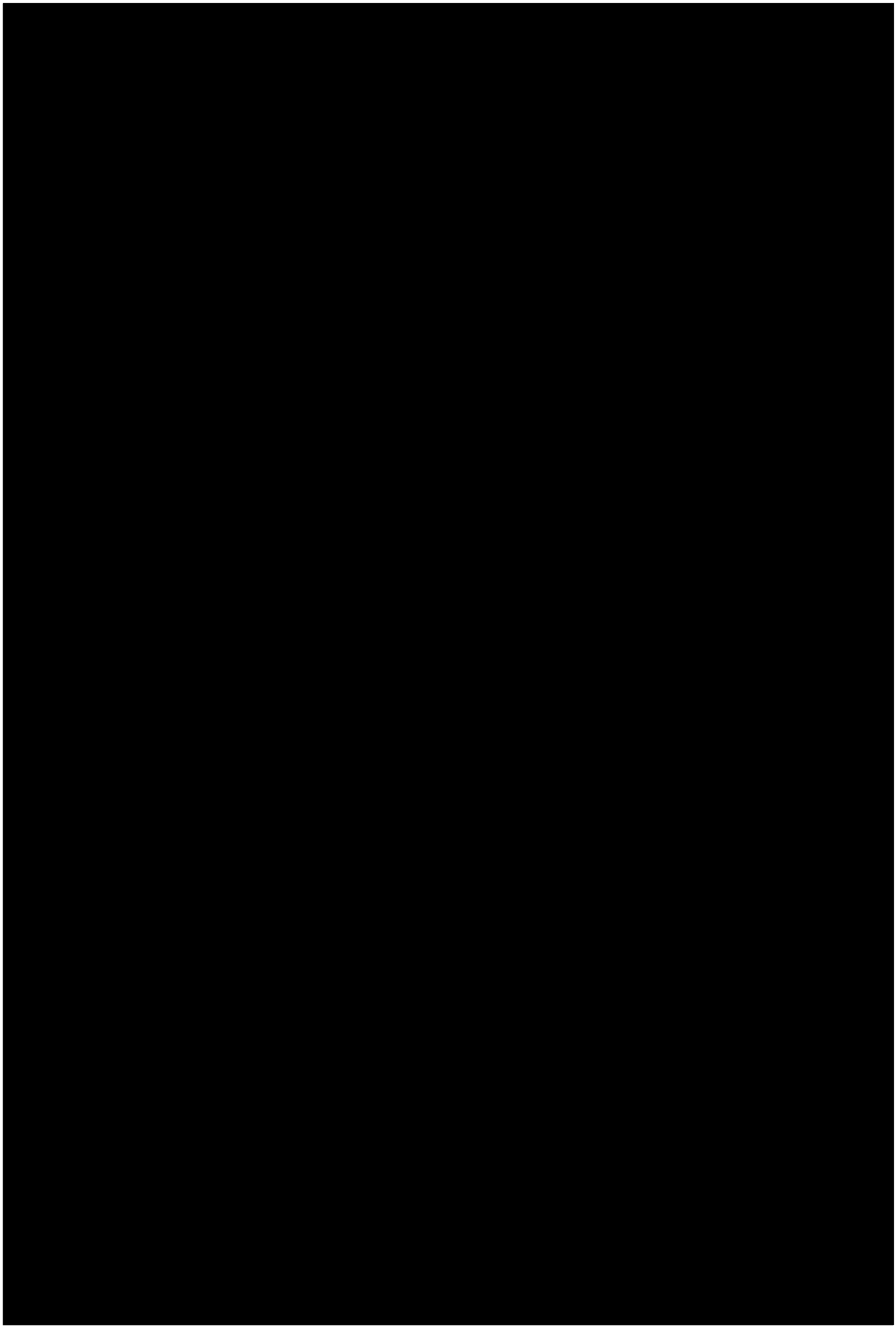

A.E.R.E. HARWELL
PHOTOGRAPHIC GROUP

HR 1518

NOT FOR PUBLICATION

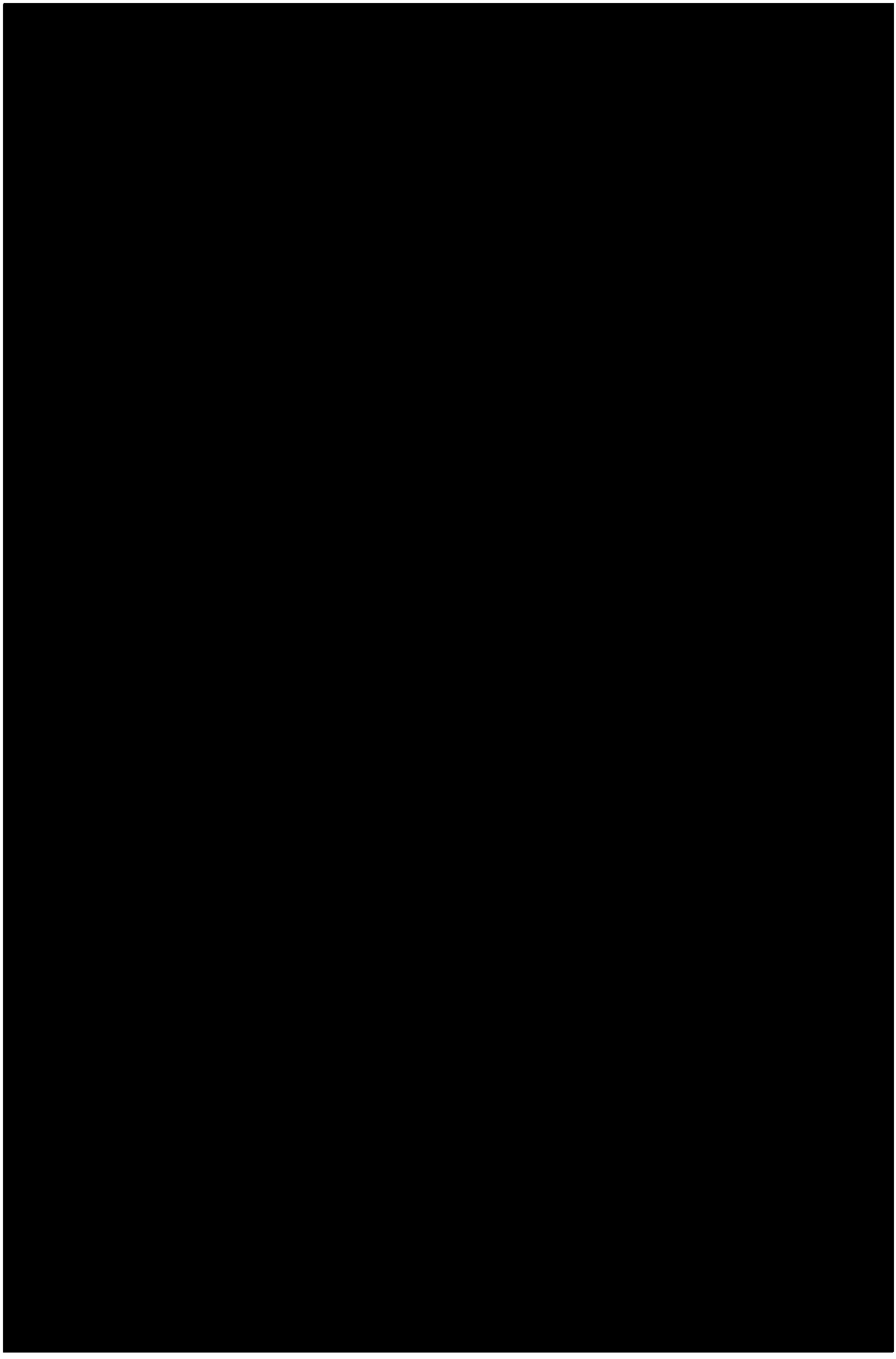

A.E.R.E. HARWELL
PHOTOGRAPHIC GROUP

HR 1518

NOT FOR PUBLICATION

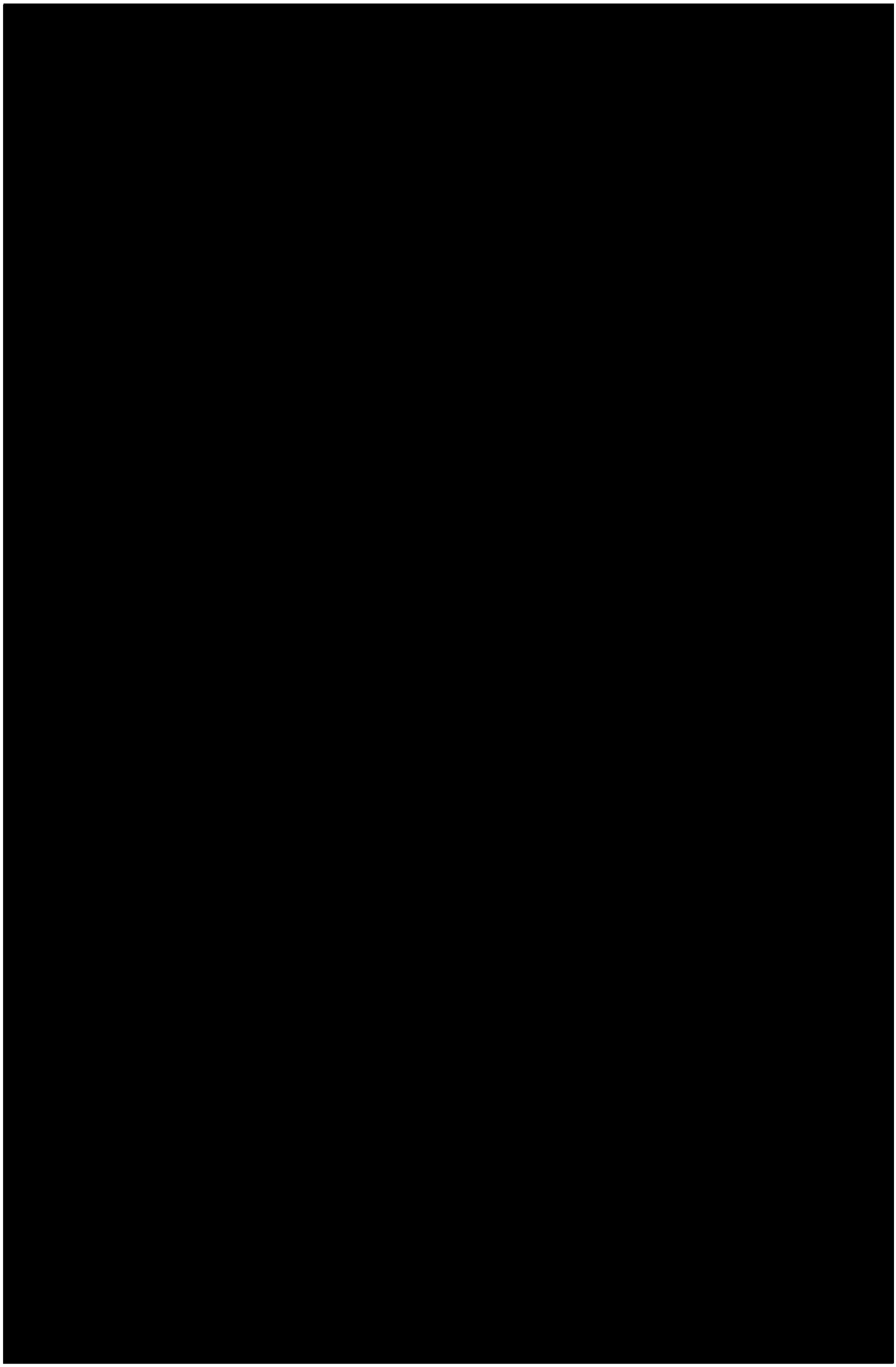

A.E.R.E. HARWELL
PHOTOGRAPHIC GROUP

HR 1510

NOT FOR PUBLICATION

5.4 DEFECT YIELD DETERMINATIONS

5.4.1 Procedure

As described in Chapter Three, comparison of the 110DF micrographs of a given area with the various 220DF and BFK images allows the fraction of displacement cascades which have collapsed to dislocation loops (i.e. the defect yield) to be determined. In order that the smallest resolvable loops be visible on the printed micrographs, a high linear magnification is required. For this reason, printing magnifications of between 9 and 12 were employed, giving total print magnifications of between 550,000 and 800,000.

Thus magnified, all the available 110DF and $1\bar{1}0$DF micrographs were examined, and all disordered zones visible on the 110DF prints were also present on the $1\bar{1}0$DF and vice versa. Examples of disordered zones in all twelve irradiation conditions are shown in Appendix A. All zones identified in this manner were individually numbered. Subsequently, the fundamental micrographs of the same area were examined and all loop images identified. It must be emphasized that the loops were identified quite independently of the disordered zones, in order to increase the likelihood of identifying only genuine loops.

By comparing the 110DF print with each fundamental image sequentially it was possible to match disordered zone images to loop images and thus identify, by their number, each disordered zone which contained a dislocation loop. The fraction:

$$\frac{\text{No. of zones which contain a loop}}{\text{Total No. of zones identified}}$$

is defined as the defect yield. Examples of this zone to loop matching procedure are shown in Fig 5.5 for various conditions. If fundamental micrographs from only one systematic row are used, then it is to be expected that not all loops would have been imaged and the ratio is known as the "single tilt defect yield". If, however, micrographs from both systematic rows are employed, every loop should have been identified and the ratio is known as the "double tilt defect yield" or simply "true defect yield". In the case of the HVEM analyses, only the single tilt values could be obtained, but in the JEM100B case, two single tilt values (one from each systematic row) and the double tilt value were evaluated. In all twelve cases the single tilt defect yield was between 70 and 90% of the true value (the fact that this figure is not 100% illustrates that despite the additional diffraction vectors operating, one systematic row is insufficient to image all loops). Despite this shortcoming of the HVEM analyses, since the conditions of the experiments were the same in all cases, the single tilt values are comparable. Thus, if loops are present both at low temperature and after warming to room temperature in the HVEM micrographs, comparison of the respective single tilt defect yields allows any change on warming to be identified. Of course, the local bending of a given area must result in contributions from other diffraction vectors producing contrast from loops which would normally be out of

Fig 5.5 Matching of disordered zones with dislocation loops under various irradiation conditions. Zones are in (a), with loops in (b) in each case.

100keV Ar low temperature irradiation recorded on HVEM at low temperature.

100keV Cu low temperature irradiation recorded on HVEM at low temperature.

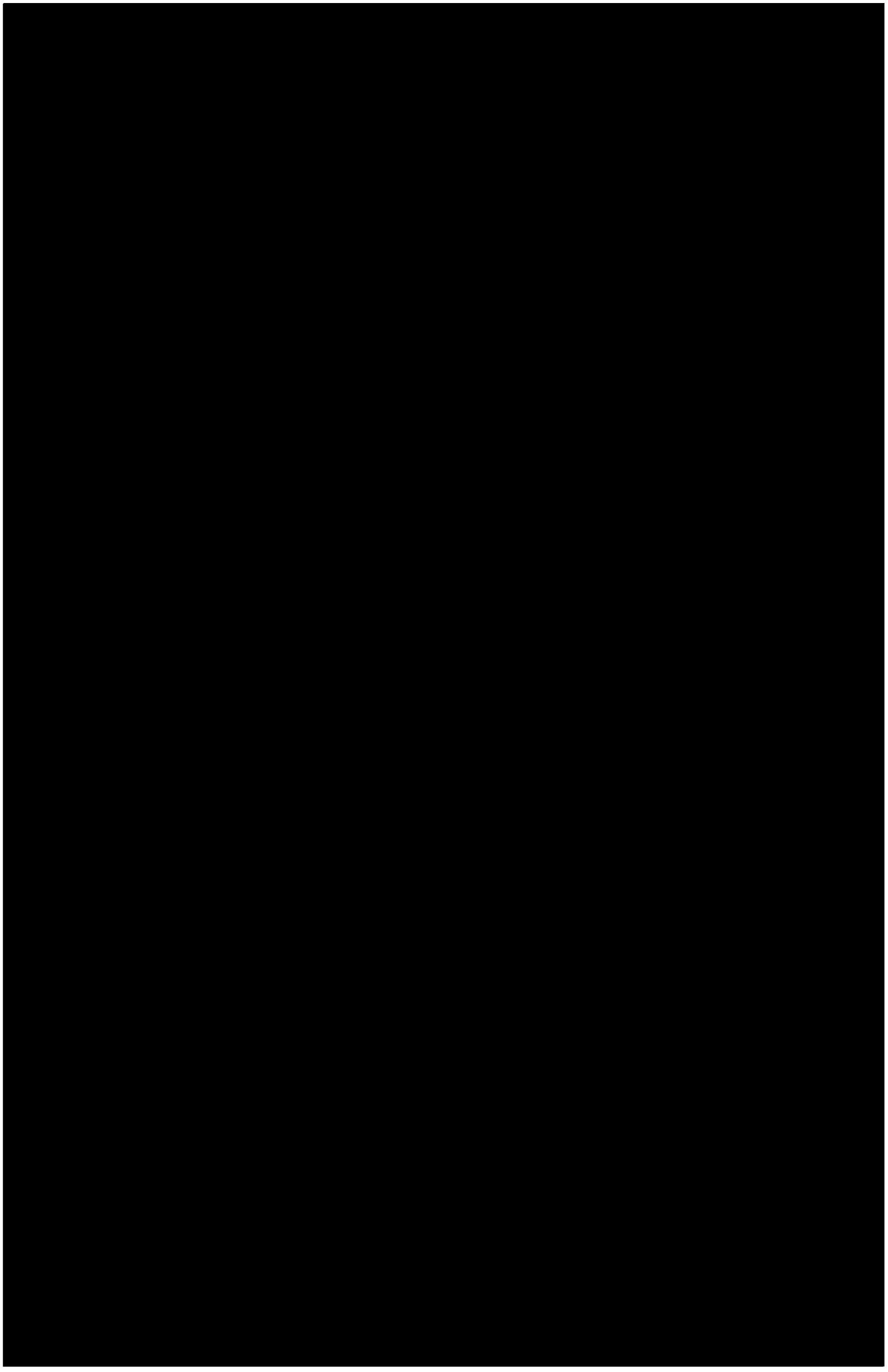

A.E.R.E. HARWELL

PHOTOGRAPHIC GROUP

HR 1509

NOT FOR PUBLICATION

50keV Kr low temperature irradiation recorded on HVEM at room temperature.

50keV Cu low temperature irradiation recorded on JEM100B.

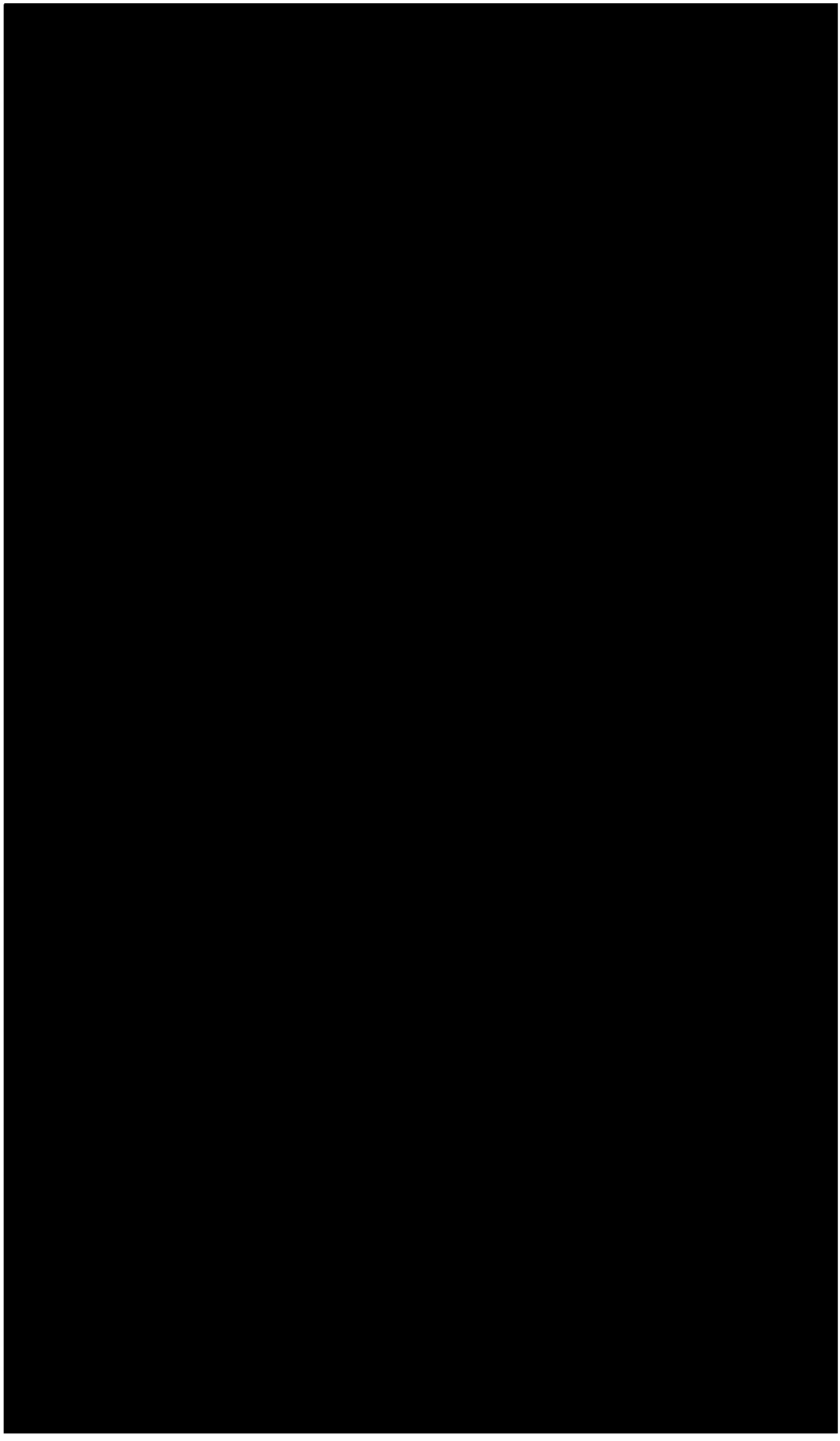

A.E.R.E. HARWELL
PHOTOGRAPHIC GROUP

HR 1512

NOT FOR PUBLICATION

50keV Ar room temperature irradiation recorded on JEM100B.

100keV Kr room temperature irradiation recorded on JEM100B

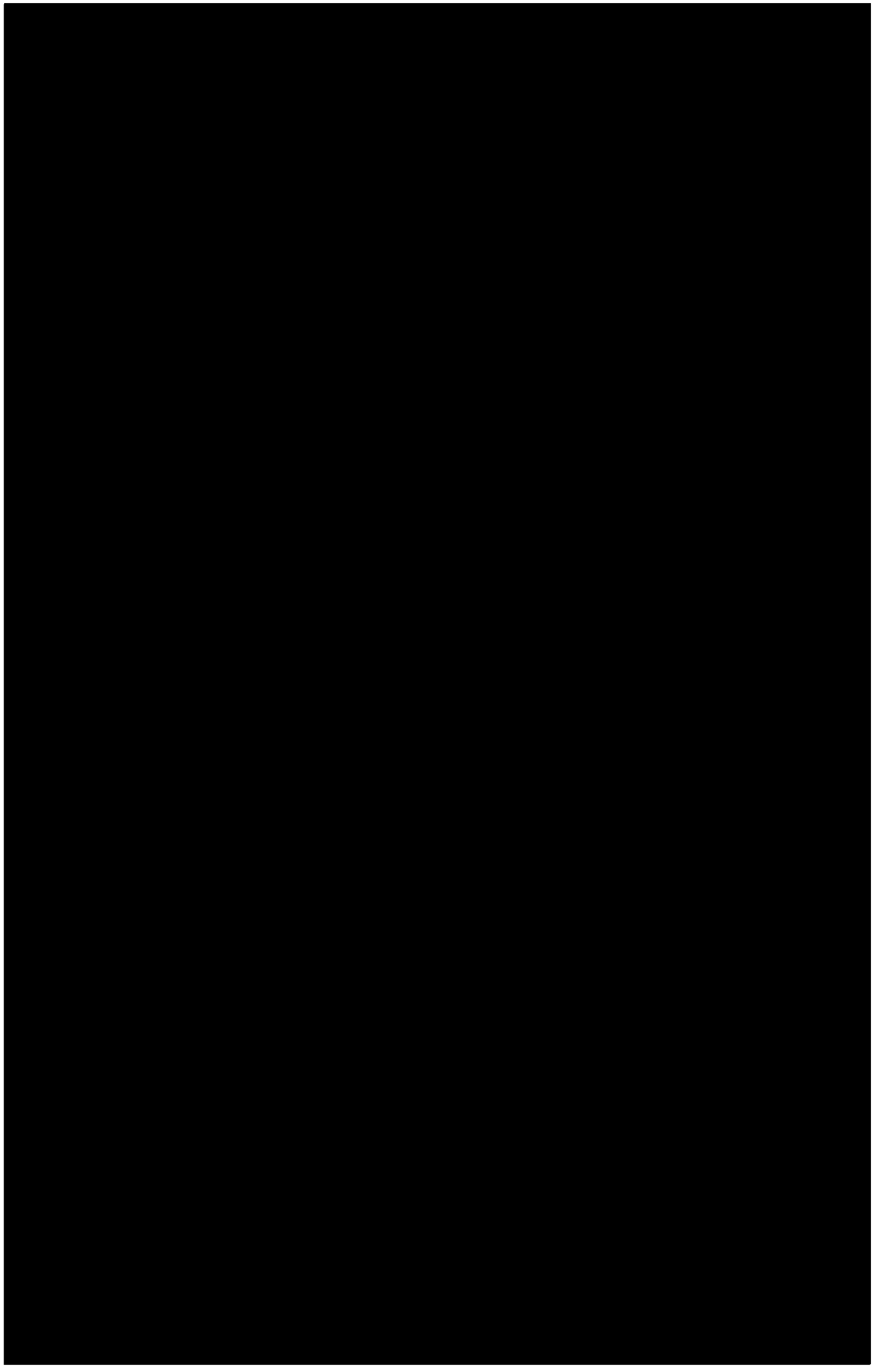

50keV Ar room temperature irradiation recorded on JEM100B.

100keV Kr room temperature irradiation recorded on JEM100B

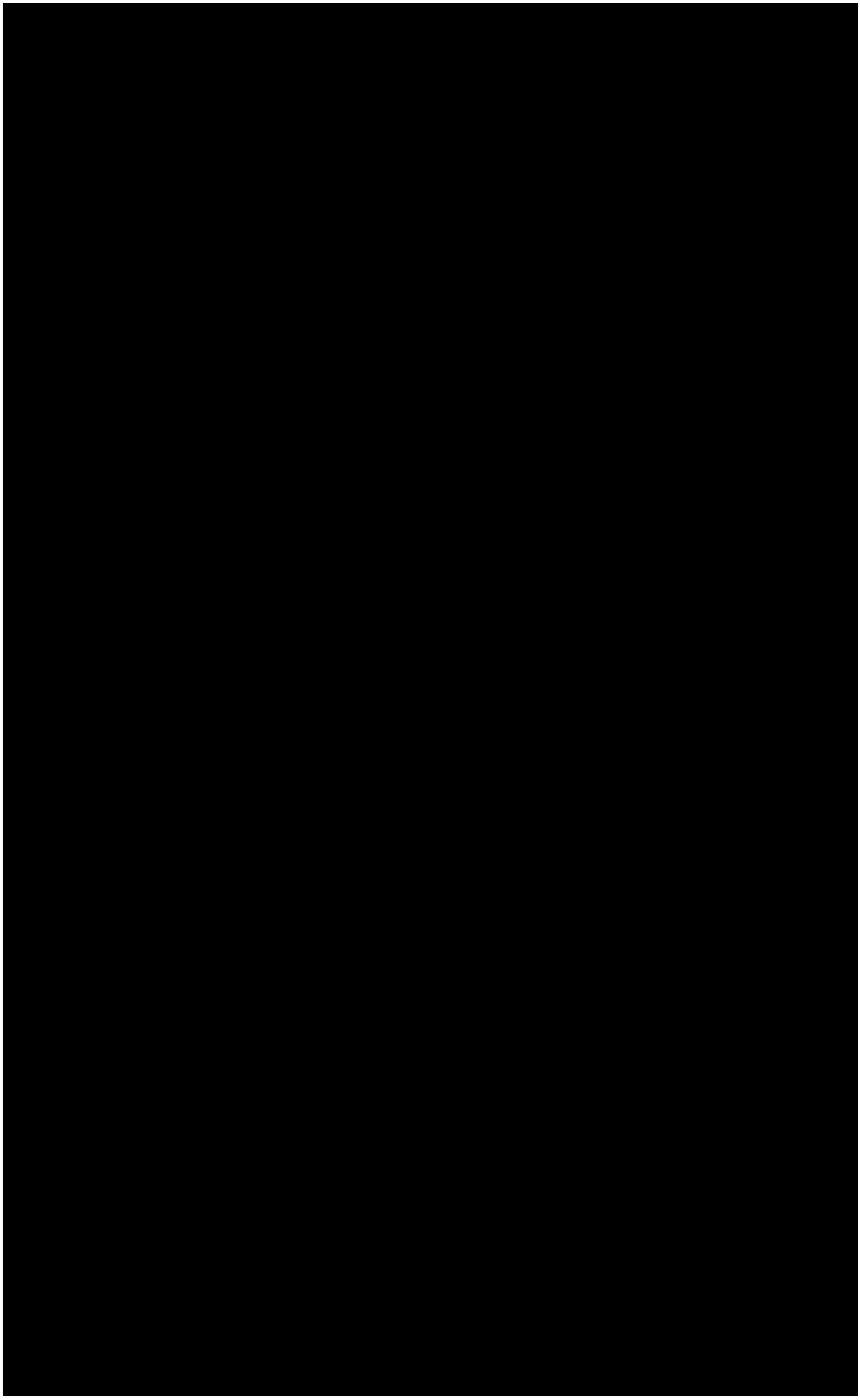

A.E.R.E. HARWELL

PHOTOGRAPHIC GROUP

HR 1511

NOT FOR PUBLICATION

contrast due to $\underline{g}.\underline{b}=0$ (Section 5.3), which in turn must result in minor statistical fluctuations in the fraction of loops which are imaged by a single systematic row and this is indeed observed. However, as great care was taken to ensure that diffraction conditions varied as little as possible between experiments, it is considered that the single tilt defect yields may be legitimately compared with one another. This is verified by the results given in the next chapter in which no systematic change in single tilt defect yields is observed on warming but small random fluctuations are apparent. Also, comparison of the HVEM single tilt defect yields with those obtained from the JEM100B using only one systematic row confirms the validity of this procedure, as no change is observed.

5.4.2 Uncertainties

Uncertainty in the defect yields obtained by the above procedure may result from any of the following sources:

(i) Random variations in collapse behaviour across the specimen.

It is quite possible that the area selected for the defect yield analysis is not typical and that a biased population has been identified for any given irradiation condition. However, for the low temperature irradiated specimens, several areas were used in each case and no significant variations in yield were detected. As a result of this, generally only one area was analysed on the room temperature irradiated specimens.

(ii) Wrongly identifying some feature as a disordered zone.

As disordered zones generally have fairly distinctive contrast, identifying some artefact as a zone is considered to be unlikely. As a precautionary measure, however, several 110DF and $1\bar{1}0$DF images were usually employed for the identification of zones.

(iii) Identifying subcascades as individual cascades.

In cases in which subcascades were present, care had to be taken to ensure that they were correctly classified as such and not as distinct cascades, as this would generate an artificially low value for the defect yield. Obviously, this situation may only arise if subcascades are produced under the irradiation condition in question, and is only expected to have a significant effect in cases of high dose, as confusion is likely to occur only if individual cascades are in close proximity. It is felt that in such cases, the tendency may have been to identify too many cascades, although it is not considered that this has significantly affected the results. Examples of the disordered zones generated under each of the twelve irradiation conditions are shown in Appendix A, and from these the conditions under which subcascades may have introduced uncertainty to the defect yield values can be recognized.

(iv) Failing to identify a loop.

Failure to image loops may have occurred if: (a) the

loop diameter is below the resolution limit of the technique (~10-20Å); (b) some contrast effect suppresses the loop's visibility; (c) foil contamination swamps the contrast from small loops.

The technique of imaging by diffraction contrast has the inherent limitation that very small loops will not be imaged. However, as most of the loops produced in the present study have diameters well in excess of the resolution limit (Section 6.3.5) it is considered that the measured defect yields should lie close to the true values. More importantly, as the size differences between loops produced by different ions are small (Section 6.3.5), the number of sub 20Å loops should be similar in each case, thus allowing the respective defect yields to be compared.

The possibility of missing loops for contrast reasons even when $\underline{g}.\underline{b} \neq 0$ has been indicated by both Stathopolous [1981] and Hertel [1979]. Each of these workers demonstrated that great care must be taken if kinematical images are used as these may fail to image a substantial fraction of the loops present. This is due to interactions between the Bloch waves in the foil which depend strongly on the excitation error as determined by Katerbau [1981]. However, Hertel's experiments demonstrated that this is less critical in thinner specimens especially if many diffraction vectors operate, as is the case in the present experiments; and Katerbau's theory indicates that the problem should be substantially alleviated if both positive ($s>0$) and negative ($s<0$) deviations from dynamical imaging conditions ($s=0$) are employed, as in this work

(Section 5.3).

Stathopolous also found that the number of loops observed in a given area depended on the pole at which the micrographs were taken. This is a manifestion of the loop's visibility altering as the effective foil thickness and defect depth are altered by foil tilting. However, he did report that the largest number of loops was observed when the pole coincided with the foil normal (i.e. when the foil is effectively thinnest), as in the present experiments. Despite this, some loops were invisible under these conditions and it cannot be excluded that this may also affect the present experiments, although with thinner foils its effect is expected to be much reduced.

Although it cannot be guaranteed that all loops present in a given area have been imaged by the procedure employed, it does seem that the conditions prevailing, (i.e. thin foil with many dynamical and kinematical images recorded in both bright and dark field) are such that all loops above ~20Å are likely to have been imaged. Thus, the defect yield values given in the next chapter are considered to closely reflect the true fraction of collapsed cascades. Even if some loops are missed by the adopted procedure, the fact that the same procedure has been followed for all irradiation conditions should result in comparison of the various defect yields being meaningful.

It is considered possible that in contaminated areas of foil, or in cases in which Moirè fringes are present on fundamental images, that small loops may have been missed. This effect

will obviously be more significant in foils of poorer quality.

(v) Wrongly identifying some feature as a loop.

Again, the erroneous identification of "loops" is expected to be more prevalent in contaminated areas of foil as under such conditions the density of artefacts, which may be mistaken for loops is increased. Additionally, it is possible that residual structure factor contrast from the disordered zones may be present in the fundamental image, and that this may mistakenly be identified as a loop. This situation may arise due to the fact that the attainment of two beam diffraction conditions in the present experiments is impossible (Section 3.3.3) and that some superlattice reflections may contribute to the fundamental image. However, if such a situation arises, it is easily detectable due to the presence of residual antiphase boundary contrast in the image. If such conditions arose, the particular fundamental micrograph was excluded from the analysis.

In an attempt to ensure that only genuine dislocation loops were included in the analysis, it was decided that only those loops present in two or more fundamental images should be classified as genuine. In cases in which a loop was identified by only one fundamental image, it was critically re-examined and a decision made about its validity. In fact, such situations were fairly rare and on average a loop was identified by five fundamental images. It is appropriate to mention at this point that in all nine cases in which the disordered zone size was measured (Section 5.5), it was found

that those zones which had collapsed to loops were invariably larger. Irrespective of the reason for this, it does indicate that in general, those zones which were identified as having collapsed had in fact done so. This provided a most satisfying independent check on the procedure for defect yield determination.

Despite this corroboration, the procedure must still be subject to the errors outlined above. The fact that such uncertainties are considered to depend largely on specimen quality has led them to be dubbed "specimen dependent" errors. Since the "quality" of a specimen is a fairly subjective concept, it was found to be rather difficult to estimate the magnitudes of these specimen dependent errors. However, two methods were adopted for this estimation. In the first of these the zone population was split into batches of twenty zones and the defect yield for each batch evaluated, so that a distribution of yields was obtained. The mean value of this distribution was in all cases exactly the same as the defect yield obtained by simply dividing the number of collapsed zones by the total number. The standard deviation of this distribution is therefore a measure of the variations in defect yield across the area of interest, and may be used to estimate the uncertainty in the defect yield value. It was interesting to note that the specimens which produced wide distributions were generally of poorer quality than those with smaller standard deviations. The second method of estimating the specimen dependent errors was as follows. As described above, if a loop was identified by only one fundamental image, it was carefully re-examined and only then classed as

collapsed or otherwise. However, if all such loops are excluded, a lower limit to the defect yield is obtained and if all such loops are included, an upper limit to the yield results. Thus, the likely limits of error may be determined.

Generally, the difference between the two methods was small although the first tended to give marginally higher values (typically between ~5 and 20% depending on the specimen), and it is these standard errors which are quoted as the likely error limits in the next chapter. Two exceptions to this were the 50 and 100keV Kr ion low temperature irradiated specimens. In these cases the first method gave fairly large spreads, but the second method produced slightly higher values and it is these which have been used.

5.5 ZONE AND LOOP-SIZING

5.5.1 Method

As described in Chapter Three, it was hoped that correlation of defect yields with disordered zone sizes would provide insight into the vacancy agglomeration mechanism which produces collapse. In particular, it was hoped that any systematic difference which may exist between those disordered zones which had collapsed to dislocation loops and those which had not, would be identified. To this end, the zones produced at each condition were measured.

In order to reduce the errors which must inevitably be incurred in the sizing of such small defects, high magnification prints were prepared. Again, linear

magnifications of between 550,000 and 800,000 were used, only in this case the magnifications were much more carefully monitored by means of recording objective lens currents and calibrating the microscope. All prints used were produced from negatives taken in the JEM100B microscope as these were generally of higher quality than the HVEM micrographs. The disordered zone sizes on such prints were typically ~1cm.

The sizing was performed by tracing around the zone peripheries with the cursor of a Hewlett Packard 9874A Digitizer which has a spatial resolution of 25μm. A coordinate pair was recorded every 0.1 secs such that a 50Å diameter zone usually required about 100 points for its periphery to be traced. The parameters determined for each zone were:

(a) Area

(b) Maximum Diameter

(c) Mean Diameter

(d) Elongation Ratio (Mean Diameter/Max Diameter)

(e) Shape Factor

with the first three quantifying zone size and the last two, zone shape. Having obtained this information for each zone individually, it was a simple matter to determine the distribution and mean value of each parameter for all zones at the irradition condition.

The acquisition of coordinates by the digitizer and subsequent manipulation of the data was controlled by a Hewlett Packard

86 Microcomputer for which three programmes were written. The peripheral coordinates acquired by the digitizer were transferred via the computer to floppy disc by a programme know as "DIGITIZE". A listing of this programme complete with extensive remark statements is given in Appendix B and it is not proposed to consider it in any further detail. The coordinates were subsequently withdrawn from disc and each of the five parameters calculated for every zone individually by a programme, "AREA", which is also listed in Appendix B. Finally, the mean value and frequency distribution for the population of zones in each irradiation condition is calculated by a third programme, "DISTRIBS", (again in Appendix B). By carefully noting if a particular zone has collapsed (from the defect yield analysis) it is possible to split the total population of zones into those which have collapsed and those which have not. Thus, comparison of the mean values and distributions in the two cases allows any systematic difference between collapsed and uncollapsed zones to be identified.

Under selected irradiation conditions, sizing of dislocation loops from kinematical bright field micrographs has also been performed by the above procedure.

5.5.2 Uncertainties

As the resolution of the digitizer is 25μm and the distance between consecutive coordinates is typically 100 to 200μm it is not considered that this will limit the results obtained. This was confirmed by comparing the results obtained using the

specially written software with those generated by the commercially available KONTRON digitizer. The mean diameter in each case was found to agree to within 1%. It is much more likely that the subjective assessment of where a zone periphery lies will determine the uncertainty in the results quoted in Chapter Six. However, as the digitizing was performed in as consistent a manner as possible, it is considered that although the disordered zone sizes obtained may be in error in an absolute sense, they are comparable relative to each other.

Even monoenergetic ions will create a range of knock-on energies in a crystal lattice resulting in a random variation in zone size and shape, which is apparent from the distributions shown in Chapter Six. The standard deviations of these distributions thus provides a measure of the uncertainty in the mean values quoted and it is these values which are given as the errors in the next chapter.

5.5.3 Subzone Frequency

In the 50keV irradiations, distinct subcascades were rare although at 100keV they were somewhat more common. In an attempt to supplement the data on zone shapes obtained from the digitizing procedure, the presence of such subcascades or lobes was identified on each of the disordered zones at room temperature, and the mean number of subzones per zone evaluated for each condition, the results being presented in the next chapter. Examples of such subzones or lobes are shown in Fig 5.6.

Fig 5.6 Disordered zones created by 100keV Kr ions, comprising:

(a) a single zone

(b) two subzones

(c) three subzones.

A.E.R.E. HARWELL

PHOTOGRAPHIC GROUP

HR 1516

NOT FOR PUBLICATION

CHAPTER SIX

RESULTS

6.1 INTRODUCTION

In this chapter quantitative data, obtained by applying the analyses described in the preceding chapter, are presented and the major results are identified.

As described in Chapter Five, ion irradiations of Cu_3Au thin films were performed under twelve irradiation conditions. Ar, Cu and Kr ions of energy 50keV and 100keV were implanted both at low temperature (T~10K) and at room temperature, always at nominal doses of ~10^{11} ions cm^{-2}. TEM micrographs of the low temperature irradiated (LTI) specimens were taken in the Argonne HVEM both at low and room temperature and again in the Oxford JEM 100B, giving three sets of micrographs in all. The room temperature irradiated (RTI) specimens were analysed only in the JEM100B.

Defect yield determinations were attempted in twenty-one of the twenty-four cases, with disordered zone sizes and shapes computed for nine of these. Additionally, dislocation loop sizes were measured in three cases. Table 6.1 summarises the various analyses which were performed in each case. The disordered zone and dislocation loop sizes were always obtained from micrographs taken in the 100keV instrument as these were generally superior to the HVEM micrographs.

It was considered unnecessary to measure all six of the

LTI	50keV Ar	50keV Cu	50keV Kr	100keV Ar	100keV Cu	100keV Kr
Defect Yld Low Temp HVEM	P	I	P	P	P	P
Defect Yld Room Temp HVEM	P	I	P	P	P	P
Defect Yld Room Temp 100B	I	P	P	P	P	P
Disordered Zone Sizing	N	P	P	P	N	N
Loop Sizing	N	P	N	N	N	N

RTI	50keV Ar	50keV Cu	50keV Kr	100keV Ar	100keV Cu	100keV Kr
Defect Yld Room Temp JEM100B	P	P	P	P	P	P
Disordered Zone Sizing	P	P	P	P	I	P
Loop Sizing	N	P	N	N	N	P

TABLE 6.1 Types of analyses carried out under each of the twelve irradiation conditions.

LTI = Low Temperature Irradiation
RTI = Room Temperature Irradiation
P = Analysis performed
I = Analysis impossible for experimental reasons
N = Analysis not attempted

disordered zone populations produced at low temperature, or indeed to measure dislocation loop sizes in all cases. Table 6.1 indicates that in the 50keV Ar LTI and 50keV Cu LTI cases, the defect yield data sets are incomplete for experimental reasons. Also, the 100keV Cu RTI zone sizes could not be obtained. The reasons for these deficiencies are indicated at the appropriate points below.

6.2 DEFECT YIELD RESULTS

6.2.1 Low Temperature Irradiation Results

The procedure for determining defect yield values outlined in Section 5.4 was applied to micrographs of specimens irradiated under all six conditions at low temperature. The results of this study are given in Table 6.2. The first two rows contain the single tilt defect yield values obtained from HVEM micrographs. The values displayed in row 3 are means of the two single tilt values available from the JEM100B analysis. It is worth re-emphasising that since a single g=<220> reflection is incapable of imaging all loops, these "single tilt yields" are not true defect yields. The limits of error quoted for each defect yield value were obtained by considering local spatial variations in the yield, as described in Section 5.4.2. The other figures given in this table are the sizes of the zone populations used to determine the defect yield in each case. Initially, 300 to 400 zones were examined at each condition although it was found that variations in the yield were rare after 150 to 200 zones had been examined. For this reason, later analyses were performed on reduced populations. In-situ

	50keV Ar	50keV Cu	50keV Kr	100keV Ar	100keV Cu	100keV Kr
Low Temp Single Tilt HVEM	0.25 ±0.02	-	0.38 ±0.08	0.24 ±0.02	0.36 ±0.02	0.36 ±0.07
	245		223	420	351	244
Room Temp Single Tilt HVEM	0.22 ±0.04	-	0.50 ±0.10	0.22 ±0.02	0.32 ±0.03	0.42 ±0.08
	128		211	335	358	237
Room Temp Single Tilt JEM100B	-	0.43 ±0.04	0.38 ±0.08	0.22 ±0.02	0.37 ±0.04	0.42 ±0.08
		190	130	342	323	248

TABLE 6.2 Single tilt defect yield values for specimens irradiated at low temperature. (The larger figures given are zone population sizes.)

	50keV Ar	50keV Cu	50keV Kr	100keV Ar	100keV Cu	100keV Kr
220	-	0.46	0.36	0.25	0.41	0.36
$2\bar{2}0$	-	0.39	0.39	0.20	0.33	0.47
Single Tilt Mean	-	0.43	0.38	0.22	0.37	0.42
Double Tilt	(0.31)	0.53 ±0.05	0.48 ±0.1	0.32 ±0.02	0.49 ±0.04	0.52 ±0.1
		190	130	342	323	248
	-	81%	81%	69%	75%	82%

TABLE 6.3 JEM100B defect yield values for specimens irradiated at low temperature.

( ) = Estimated value; see text.

values for the 50keV Cu case are not available due to this particular low temperature experiment being badly affected by mechanical vibration of the stage. This problem of course did not affect the irradiation itself and the JEM100B experiment was possible. In contrast, the 50keV Ar in-situ experiment was successful but subsequent specimen contamination prevented any further analysis of this condition.

Three significant conclusions can be drawn from Table 6.2:

(i) Cascade collapse occurs even at low temperatures where vacancies and interstitials are thermally immobile.

(ii) No significant change in the number of collapsed cascades is observed on warming to room temperature. (In the 50keV Kr case, the room temperature defect yield obtained at Argonne seems to be somewhat higher than the low temperature value. In view of the fact that the JEM100B value is exactly the same as that obtained at low temperature in the HVEM, it is concluded that in the room temperature HVEM case the local diffraction conditions were probably such that the single axis of tilt was sufficient to image almost all the loops present in that area (Section 5.4.1)).

(iii) Observations made in the JEM100B at Oxford are entirely consistent with the HVEM values obtained at Argonne.

It may have been expected that in all conditions more loops would be seen with the 100keV instrument due to its superior resolution, but this does not appear to be the case, probably because the incidence of very small loops (i.e. between the resolution limits of the two instruments, 15-30Å) is low (Section 6.3.5).

Having established that no change in defect yield is observed on warming to room temperature, or indeed on transporting foils to Oxford, the obvious corollary is that the defect yields measured by using the double tilt facility of the JEM100B are true reflections of the collapse occurring at low temperatures. These results are shown in Table 6.3. The individual single tilt values are shown in the first two rows simply to give an idea of the spread involved. Inspection of row 4 illustrates that:

(i) No change in defect yield was observed due to the change of ion energy from 50 to 100keV.

(ii) 100keV Ar ions produced a significantly lower defect yield than either of its Cu or Kr counterparts which were virtually indistinguishable.

Finally, the last row in Table 6.3 expresses the single tilt defect yield as a fraction of the double tilt value. The small spread in these values indicates that the relative proportions of loop types are probably similar in each case. By using the mean value of 78% in conjunction with the HVEM 50keV Ar defect yields, a rough estimate of 0.31 can be obtained for the double tilt value under these conditions.

Again, this Ar estimate is appreciably lower than either the Cu or Kr values at 50keV.

6.2.2 Room-Temperature Irradiation Results

In general, the specimens irradiated at room temperature were of a superior quality than their low temperature counterparts; the respective estimated errors reflect this. (See Section 5.4.2.) The defect yield values obtained from the room temperature specimens are given in Table 6.4, the layout being as for Table 6.3. On average, the mean single tilt defect yield is 82% of the double tilt value and in most cases, the two single tilts are fairly similar. The important points which can be drawn from this set of results are:

(i) A systematic increase in defect yield with increasing ion mass is observed at both ion energies.

(ii) Again, no significant change in defect yield on increasing ion energy from 50 to 100keV is evident.

Additional support is given to these results from a previous study [Jenkins and Wilkins 1976] in which bombardment of Cu_3Au with 50keV and 100keV Cu ions produced defect yields of 0.65 ±0.1 and 0.70±0.1, in agreement with the results in Table 6.4.

6.2.3 Comparison of Room and Low Temperature Irradiations

For ease of inspection, the double tilt defect yields have been extracted from Table 6.3 and 6.4 and are shown in Table 6.5. From inspection of this table it becomes obvious that:

	50keV Ar	50keV Cu	50keV Kr	100keV Ar	100keV Cu	100keV Kr
220	0.27	0.48	0.67	0.30	0.52	0.73
$2\bar{2}0$	0.32	0.49	0.64	0.32	0.44	0.69
Single Tilt Mean	0.30 ±0.03	0.48 ±0.03	0.65 ±0.03	0.31 ±0.03	0.48 ±0.03	0.71 ±0.03
Double Tilt	0.40 ±0.04	0.61 ±0.03	0.74 ±0.03	0.38 ±0.04	0.63 ±0.03	0.78 ±0.03
	181	193	173	178	176	200
	75%	79%	88%	82%	76%	91%

TABLE 6.4 Defect yield values for specimens irradiated at room temperature.

	50keV Ar	50keV Cu	50keV Kr	100keV Ar	100keV Cu	100keV Kr
Low Temp Irradiation	-	0.53 ±0.05	0.48 ±0.03	0.32 ±0.02	0.49 ±0.04	0.52 ±0.04
Room Temp Irradiation	0.40 ±0.04	0.61 ±0.03	0.74 ±0.03	0.38 ±0.04	0.63 ±0.03	0.78 ±0.03
Difference	-	15%	57%	19%	29%	53%

TABLE 6.5 Comparison of low temperature and room temperature irradiated specimens, analysed at room temperature.

(i) In all cases, the defect yields obtained from the room temperature irradiated specimens are significantly higher than those obtained from their low temperature counterparts after warming to room temperature.

In some cases this difference is most striking, being over 50% in both Kr ion results. In addition, the ratio of single/double tilt defect yields is similar in each case, probably indicating the presence of similar distributions of burgers vectors although it was impossible to confirm this as the diffraction conditions were not well defined, (Section 5.3).

6.2.4 Errors and Limitations

The superlattice technique employed in this work has the strong advantage over other methods of defect yield determination that it is completely independent of both ion dosimetry and microscope magnification calibration. Errors which do occur, however, may be split into two categories; technique dependent and specimen dependent. Specimen dependent errors have already been considered in Section 5.4.2 and it is these which give rise to the error bars quoted in Tables 6.2 to 6.5. Technique dependent errors on the other hand, are not considered to have had a major influence on the results although their effect was potentially great. Possible sources of such errors which have been considered include:

(i) Loss of "perfect" $\underline{b}$ = a/2<110> loops to foil surface

It has long been appreciated that dislocation loops containing no stacking fault - perfect loops - which lie close to a surface will be attracted along their glide cylinder towards that foil surface. This effect is thought to be more prevalent in b.c.c. rather than f.c.c. metals [Eyre 1973] and has been theoretically investigated [Jäger et al 1975]. However, this is not thought to be significant for the following reason. A $\underline{b}$ = a/2<110> loop in an $L1_2$ lattice is not perfect, but contains an antiphase boundary (APB). Thus, although not sessile in the true sense, such a loop would leave a tube of APB in its wake on gliding from the foil. As no such tubes have been observed, this possibility can be excluded.

(ii) Point defect mobility induced by electron beam heating of specimen.

Although unlikely, it is just possible that the loops observed at room temperature result from a thermally activated cascade collapse process, and that those observed at low temperature are due to local beam heating of the specimen. This possibility has been investigated using the model of Gale and Hale [1961] which has been expanded by Fisher [1970]. The calculations are shown in Appendix 6.1. The temperature rise of 9.2K was obtained by

neglecting radiation losses and assuming a fully focused electron beam. In fact, since dislocation loops were still observed if a heavily defocused beam was used [Fig. 6.1], which would lead to a reduced temperature rise, it is concluded that beam heating cannot be responsible for the loops observed at low temperature.

(iii) Point defect mobility induced by sub-threshold electron beam effects.

Despite the fact that 300keV electrons are not sufficiently energetic to produce vacancies and interstitials in Cu_3Au, they may transfer sufficient energy to a lattice atom neighbouring a vacancy to cause vacancy migration. This idea was first suggested by Nelson [1964] and more recently investigated by Urban [1979]. Urban has shown that a sub-threshold electron irradiation can cause agglomeration of pre-existing isolated defects to occur even at temperatures below the onset of thermal mobility, provided sufficient irradiation times and electron fluxes are employed. However, the simple calculation in Appendix 6.2 clearly demonstrates that this effect could not produce the loops observed under the experimental conditions used in this work.

Fig 6.1 BFK(220) micrograph recorded at low temperature within 60 seconds of illumination of the area with a diffuse electron beam. Dislocation loops (created by 100keV Ar ions) are visible indicating that neither beam heating nor beam induced defect mobility are responsible for collapse at low temperatures. (See text).

A.E.R.E. HARWELL
PHOTOGRAPHIC GROUP

HR 1513

NOT FOR PUBLICATION

6.3 ZONE AND LOOP SIZES

The primary objective of the zone sizing procedure was to investigate any correlation which may exist between zone size/shape and collapse probability. As a natural consequence of this the dependence of zone size/shape on ion mass, ion energy and irradiation temperature was determined. Three of the zone populations produced at low temperature were sized (from micrographs taken at room temperature in the JEM100B) and five produced at room temperature were measured. As explained in Chapter Five, five parameters were evaluated from the digitized periphery of each zone. The area, maximum and mean diameters quantify zone size, whereas the shape factor and ratio (of the two diameters) parameters describe zone shape. Supplementary data on zone shapes is provided by the mean number of sub-zones (as illustrated in Fig. 5.6) present in each zone for each of the five room temperature irradiations.

Table 6.6 gives average values for all five size/shape parameters computed for each room temperature irradiation condition using:

(a) total zone populations;

(b) only collapsed zones (i.e. zones containing loops);

(c) only uncollapsed zones (i.e. zones not containing loops).

Units are Å for lengths and $Å^2$ for areas. Table 6.7 shows analogous results for the low temperature irradiation conditions with data on sub-zones presented in Table 6.8.

TABLE 6.6 MEASURED ZONE PARAMETERS FOR ROOM TEMPERATURE IRRADIATED (RTI) SPECIMENS.

(a) For total zone populations.

(b) For collapsed zone populations.

(c) For uncollapsed zone populations.

Footnote:

The 100keV Cu zones were not sized simply because they did not show as strong contrast as the other conditions, (probably due to the foil being slightly thicker), and it was feared that this may affect the results.

TABLE 6.6(a)	50KeV Ar	50keV Cu	50keV Kr	100keV Ar	100keV Kr
AREA	4540 ±220	5840 ±250	6020 ±280	6780 ±370	9900 ±440
MAX DIAM	104 ±3	113 ±3	114 ±3	125 ±4	155 ±4
MEAN DIAM	75 ±2	85 ±2	86 ±2	90 ±2	112 ±3
RATIO	0.748 ±0.006	0.768 ±0.006	0.769 ±0.006	0.746 ±0.006	0.743 ±0.006
SHAPE	0.263 ±0.007	0.242 ±0.006	0.238 ±0.006	0.269 ±0.007	0.266 ±0.007
	181	193	173	178	200

TABLE 6.6(b)	50keV Ar	50keV Cu	50keV Kr	100keV Ar	100keV Kr
AREA	5560 ±360	6415 ±340	6390 ±320	9460 ±690	11210 ±510
MAX DIAM	117 ±5	119 ±4	117 ±4	153 ±7	167 ±5
MEAN DIAM	84 ±3	90 ±2	88 ±2	109 ±4	120 ±3
RATIO	0.741 ±0.01	0.774 ±0.008	0.771 ±0.007	0.733 ±0.009	0.740 ±0.006
SHAPE	0.271 ±0.01	0.236 ±0.008	0.235 ±0.007	0.283 ±0.01	0.271 ±0.008
	72	117	127	68	156

TABLE 6.6(c)	50keV Ar	50keV Cu	50keV Kr	100keV Ar	100keV Kr
AREA	3870 ±250	4940 ±270	5030 ±230	5120 ±280	5270 ±240
MAX DIAM	96 ±4	105 ±4	106 ±3	108 ±3	110 ±3
MEAN DIAM	70 ±2	78 ±2	78 ±2	79 ±2	81 ±2
RATIO	0.753 ±0.01	0.759 ±0.008	0.763 ±0.006	0.755 ±0.006	0.757 ±0.006
SHAPE	0.259 ±0.01	0.253 ±0.01	0.248 ±0.006	0.261 ±0.007	0.251 ±0.007
	109	76	46	110	44

TABLE 6.7 MEASURED ZONE PARAMETERS FOR LOW TEMPERATURE IRRADIATED (LTI) SPECIMENS.

(a) For total zone populations.

(b) For collapsed zone populations.

(c) For uncollapsed zone populations.

Footnote:

The zone population sized in the 100keV Ar case was different from that used to determine the defect yields. Thus, the collapsed and uncollapsed zones are unknown.

TABLE 6.7(a)	50keV Cu	50keV Kr	100KeV Ar
AREA	4230 ±220	3220 ±180	6270 ±370
MAX DIAM	97 ±3	84 ±3	118 ±4
MEAN DIAM	72 ±2	63 ±2	87 ±2
RATIO	0.761 ±0.006	0.768 ±0.007	0.763 ±0.007
SHAPE	0.249 ±0.007	0.239 ±0.008	0.249 ±0.007
	188	130	161

TABLE 6.7(b)	50keV Cu	50keV Kr	100keV Ar
AREA	4940 ±360	3940 ±320	-
MAX DIAM	105 ±4	94 ±5	-
MEAN DIAM	78 ±3	70 ±3	-
RATIO	0.761 ±0.007	0.764 ±0.01	-
SHAPE	0.246 ±0.008	0.242 ±0.01	-
	97	61	

TABLE 6.7(c)	50keV Cu	50keV Kr	100keV Ar
AREA	3470 ±250	2590 ±200	-
MAX DIAM	90 ±3	76 ±3	-
MEAN DIAM	66 ±3	57 ±2	-
RATIO	0.761 ±0.007	0.771 ±0.01	-
SHAPE	0.253 ±0.008	0.237 ±0.01	-
	91	69	

From these tables, correlations between zone size and ion mass, ion energy and irradiation temperature can be identified and these are presented in Sections 6.3.2 to 6.3.4 below. However, the most interesting correlation found is that between zone size and collapse probability.

6.3.1 Correlation between Zone Size and Collapse Probability

In all of the seven cases where the comparison was possible, the average size of a collapsed zone was significantly larger than that of an uncollapsed zone. Table 6.6 illustrates this quite clearly. If zone mean diameters are used as a measure of zone size, this effect ranges in magnitude from 13% for 50keV Kr up to 48% for 100keV Kr. As a further means of illustrating this point, distributions for both total populations and collapsed populations for three irradiation conditions are illustrated in Fig 6.2. (Total populations are used in preference to uncollapsed populations as the latter distributions, containing fewer zones, are less smooth.) In all cases the collapsed distributions are shifted to higher diameters.

6.3.2 Correlation between Zone Size and Ion Mass

An increase in zone size with increasing ion mass is evident from Table 6.6(a) and Fig 6.3. The effect appears to be more pronounced at lower ion masses with 50keV Ar zones being much smaller than 50keV Cu, but Cu and Kr being almost indistinguishable. There is a small difference between Cu and Kr

Fig 6.2 Mean diameter distributions illustrating that collapsed zones are larger than uncollapsed zones. (If the black histograms were for uncollapsed zones only, the effect would be more pronounced but such populations are generally too small for meaningful distributions to be presented.)

(a)

(b)

(c)

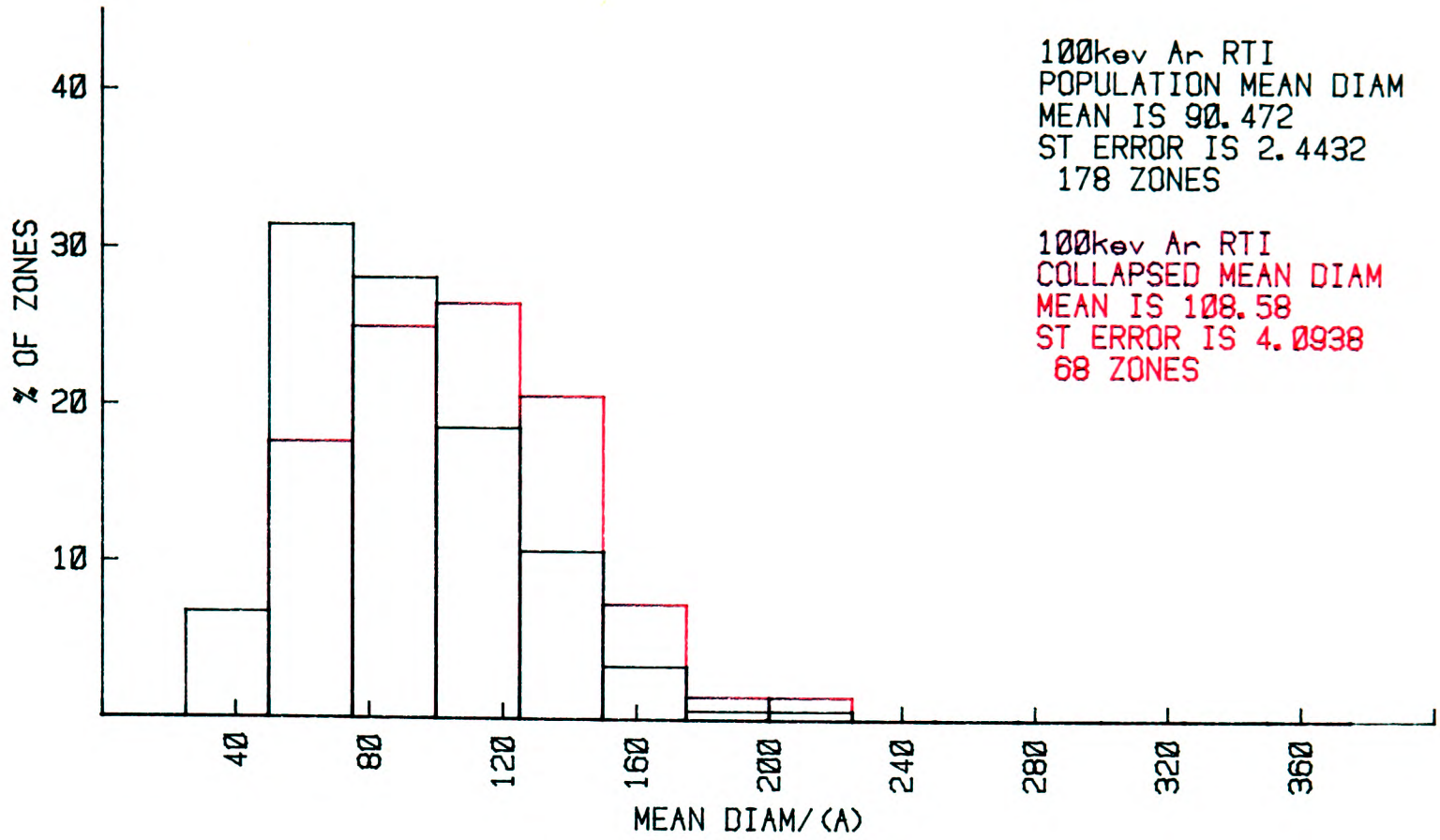
100kev Ar RTI
POPULATION MEAN DIAM
MEAN IS 90.472
ST ERROR IS 2.4432
178 ZONES
100kev Ar RTI
COLLAPSED MEAN DIAM
MEAN IS 108.58
ST ERROR IS 4.0938
68 ZONES
% OF ZONES
40
30
20
10
40
80
120
160
200
240
280
320
360
MEAN DIAM/(A)

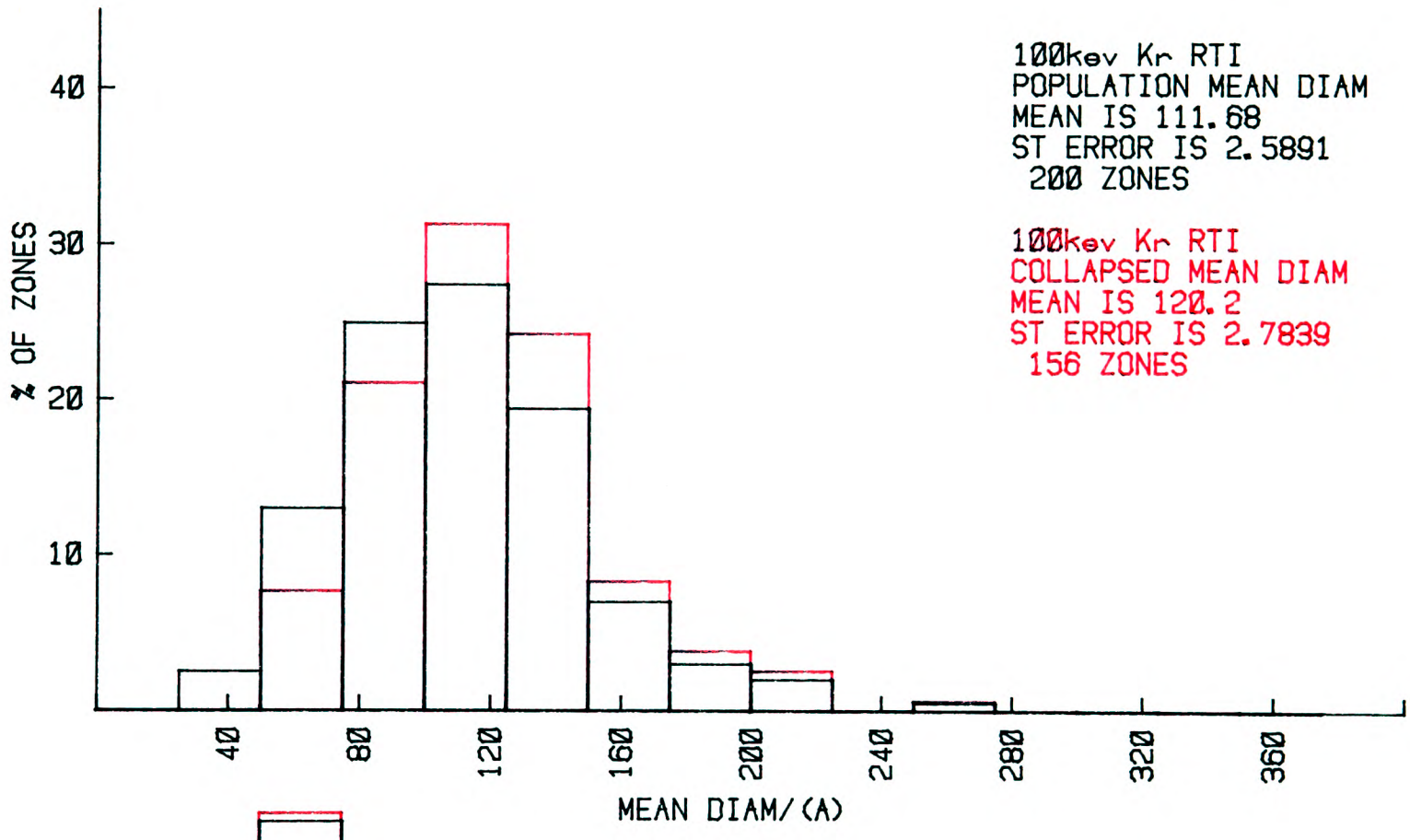
100kev Kr RTI
POPULATION MEAN DIAM
MEAN IS 111.68
ST ERROR IS 2.5891
200 ZONES
100kev Kr RTI
COLLAPSED MEAN DIAM
MEAN IS 120.2
ST ERROR IS 2.7839
156 ZONES
% OF ZONES
40
30
20
10
40
80
120
160
200
240
280
320
360
MEAN DIAM/(A)

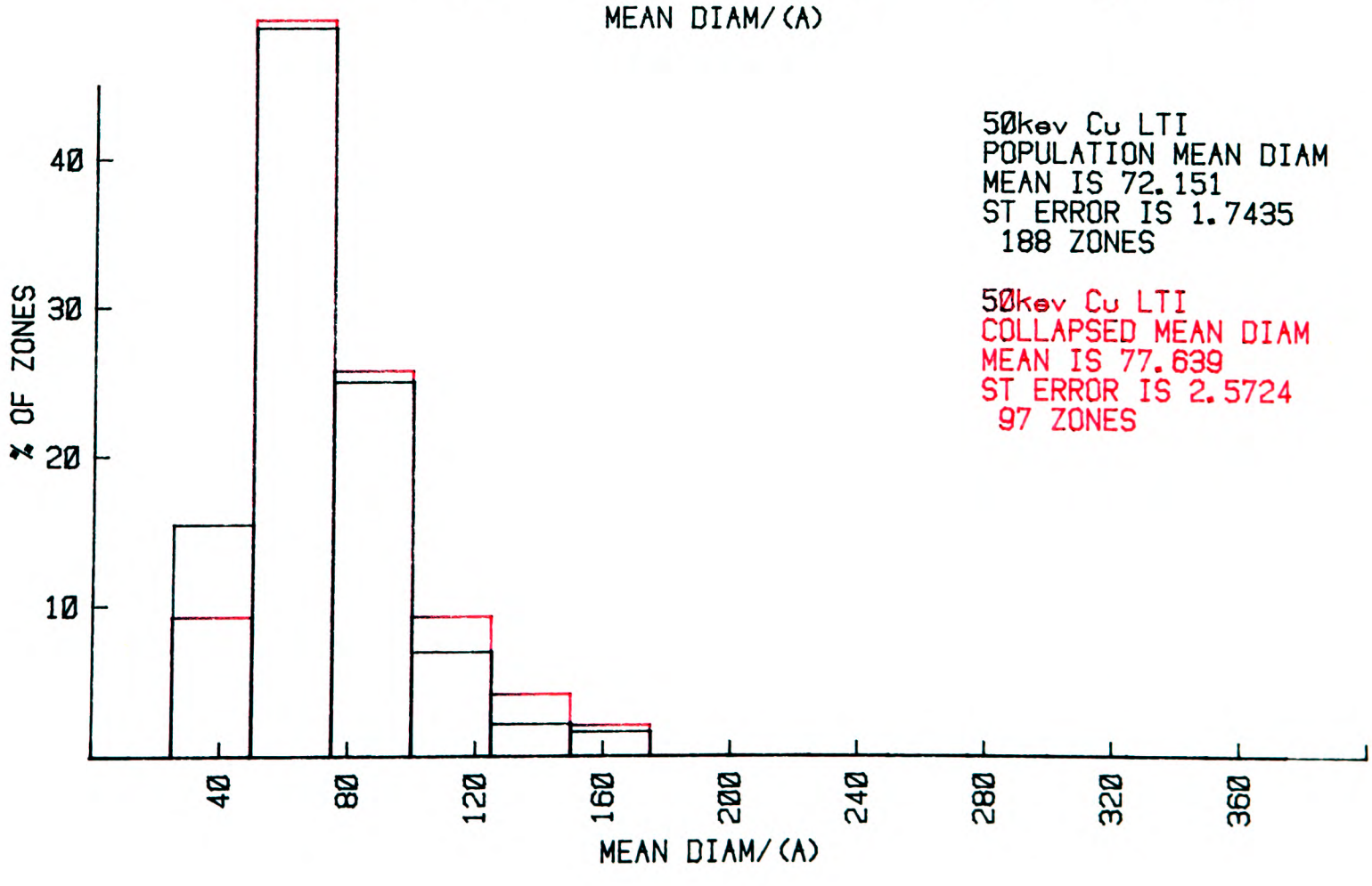
50kev Cu LTI
POPULATION MEAN DIAM
MEAN IS 72.151
ST ERROR IS 1.7435
188 ZONES
50kev Cu LTI
COLLAPSED MEAN DIAM
MEAN IS 77.639
ST ERROR IS 2.5724
97 ZONES
% OF ZONES
40
30
20
10
40
80
120
160
200
240
280
320
360
MEAN DIAM/(A)

Fig 6.3 Mean diameter distributions illustrating that heavier ions create larger disordered zones than lighter ions.

(a)

(b)

(c)

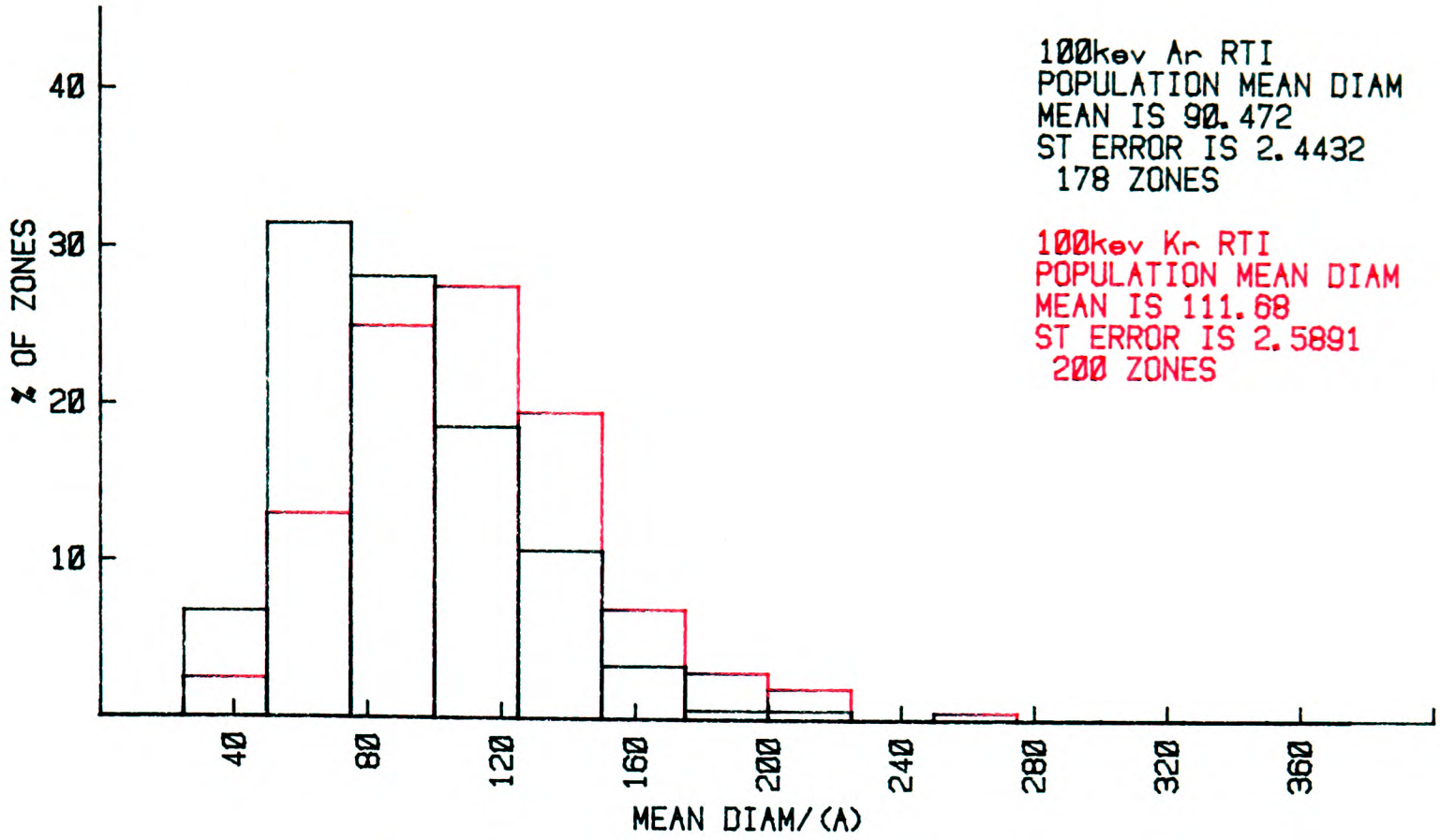
100kev Ar RTI
POPULATION MEAN DIAM
MEAN IS 90.472
ST ERROR IS 2.4432
178 ZONES
100kev Kr RTI
POPULATION MEAN DIAM
MEAN IS 111.68
ST ERROR IS 2.5891
200 ZONES
% OF ZONES
40
30
20
10
40
80
120
160
200
240
280
320
360
MEAN DIAM/(A)

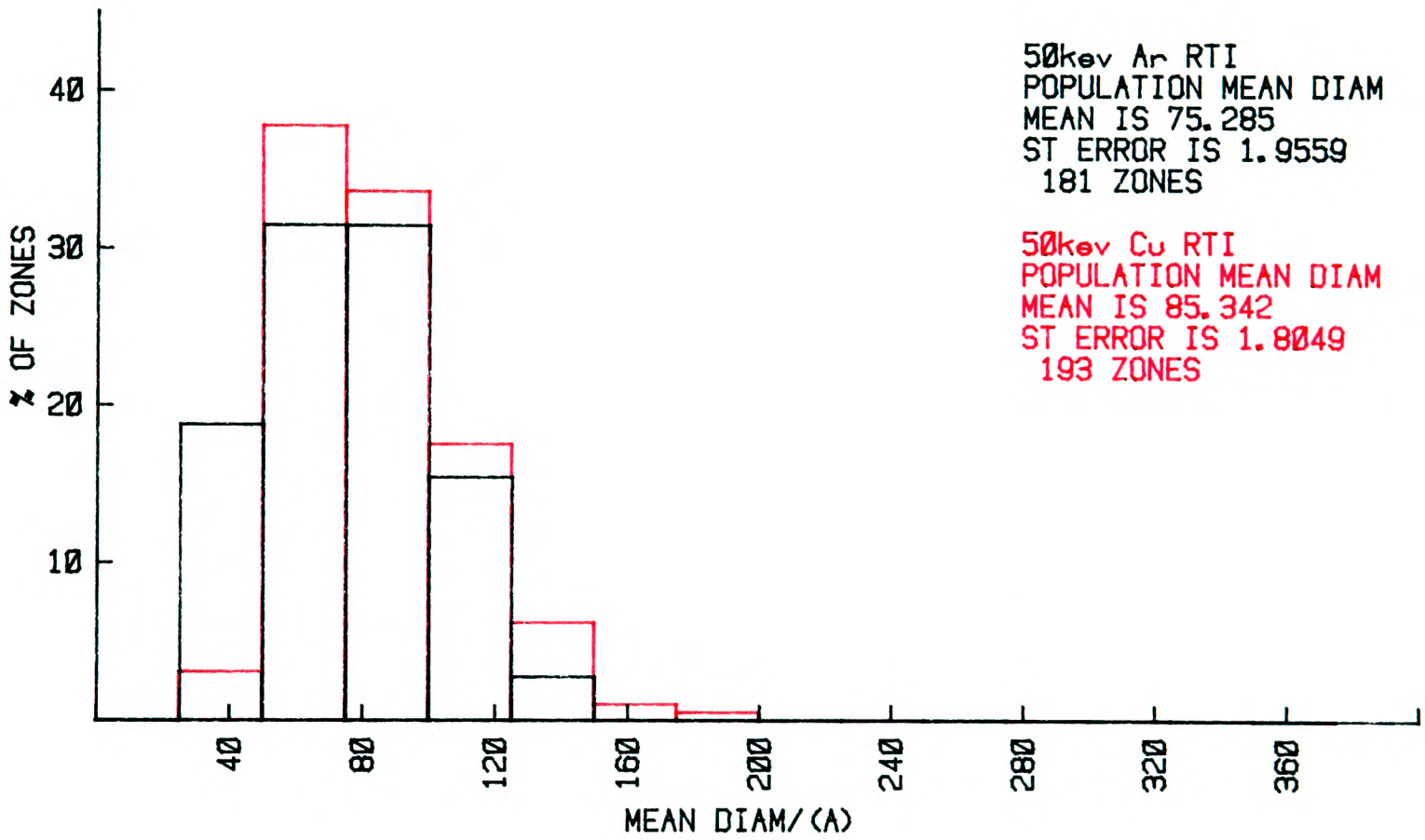
50kev Ar RTI
POPULATION MEAN DIAM
MEAN IS 75.285
ST ERROR IS 1.9559
181 ZONES
50kev Cu RTI
POPULATION MEAN DIAM
MEAN IS 85.342
ST ERROR IS 1.8049
193 ZONES
% OF ZONES
40
30
20
10
40
80
120
160
200
240
280
320
360
MEAN DIAM/(A)

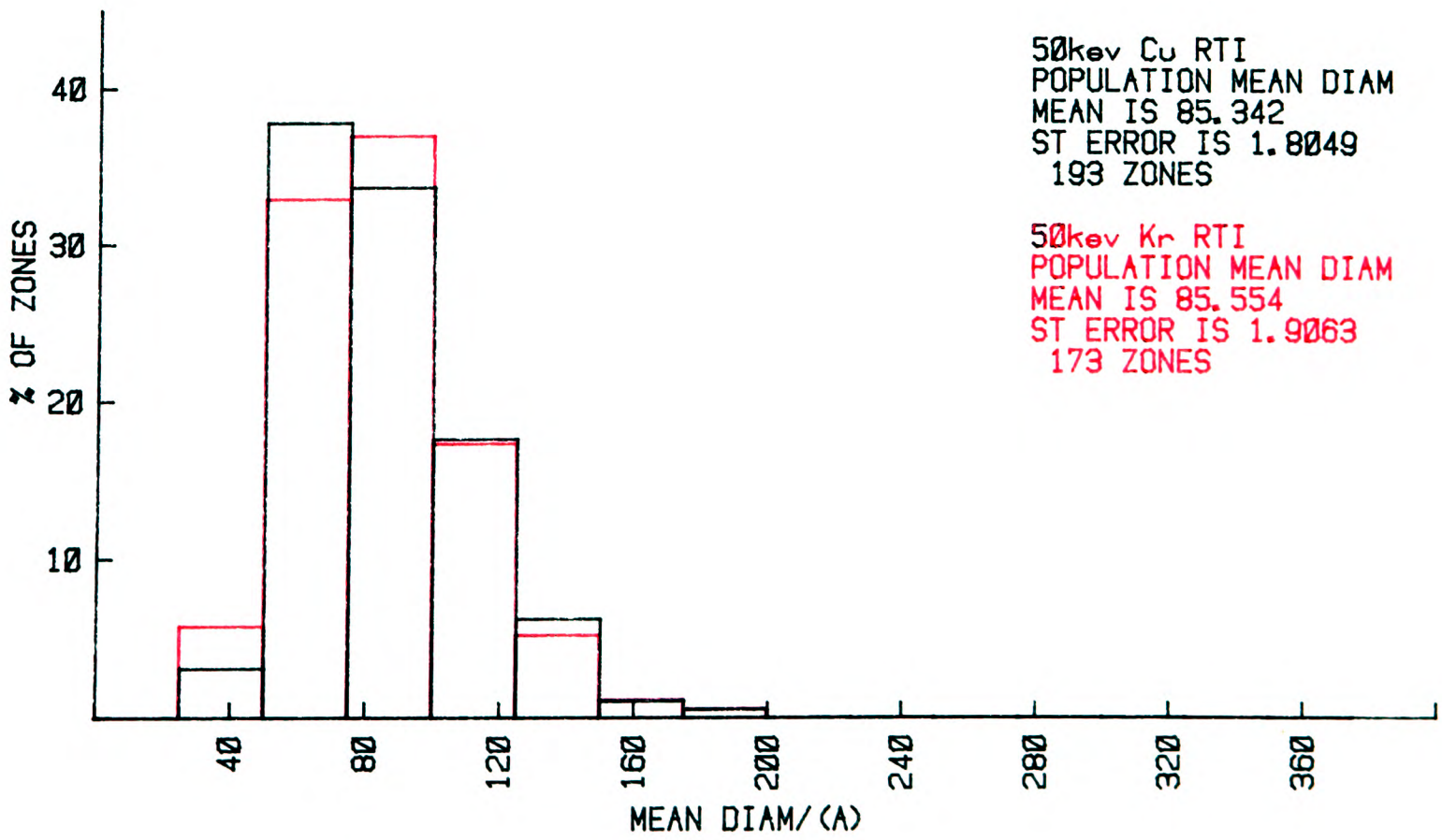
50kev Cu RTI
POPULATION MEAN DIAM
MEAN IS 85.342
ST ERROR IS 1.8049
193 ZONES
50kev Kr RTI
POPULATION MEAN DIAM
MEAN IS 85.554
ST ERROR IS 1.9063
173 ZONES
% OF ZONES
40
30
20
10
40
80
120
160
200
240
280
320
360
MEAN DIAM/(A)

which, although not obvious from the mean values can be seen more clearly from the distributions, shown in Fig 6.3(c). In addition, this mass dependence of zone size is more obvious at 100keV than at 50keV where Ar and Kr zones have a 24% and 15% difference in mean diameters respectively.

A small change in zone shape may be seen at 50keV (although not at 100keV) as the ion mass changes. Ar zones have lower ratios and higher shape factors than either Cu or Kr zones (Fig 6.4(a),(b)) illustrating that they are somewhat less regular in shape. This effect is also evident from Table 6.8 which shows that Ar zones have a greater number of subzones than either Cu or Kr zones, indicating more irregularity.

This observation that heavier ions produce larger disordered zones, coupled with the fact that defect yields are also greater for heavier ions, is entirely consistent with the observation made in Section 6.3.1 that within any single irradiation condition, the larger disordered zones tend to collapse more readily.

6.3.3 Correlation between Zone Size and Ion Energy

In both cases where the direct comparison can be made between zones produced by the same ion at 100keV and 50keV, the higher energy zones are substantially larger. Again, Table 6.6(a) and Fig 6.5 illustrate that the mean diameter of Ar zones increases by 20% and of Kr zones by 36% on doubling the energy. In addition, the zones produced at higher energy have smaller ratios (Fig 6.4(c)), greater shape factors and greater

Fig 6.4 Ratios of mean to maximum zone diameters illustrating:

(a) That lighter ions are less regularly shaped than heavier ions at 50keV.

(b) That ion mass has no noticeable effect on zone shape at 100keV.

(c) That higher energy zones are less regularly shaped than those produced by lower energy ions.

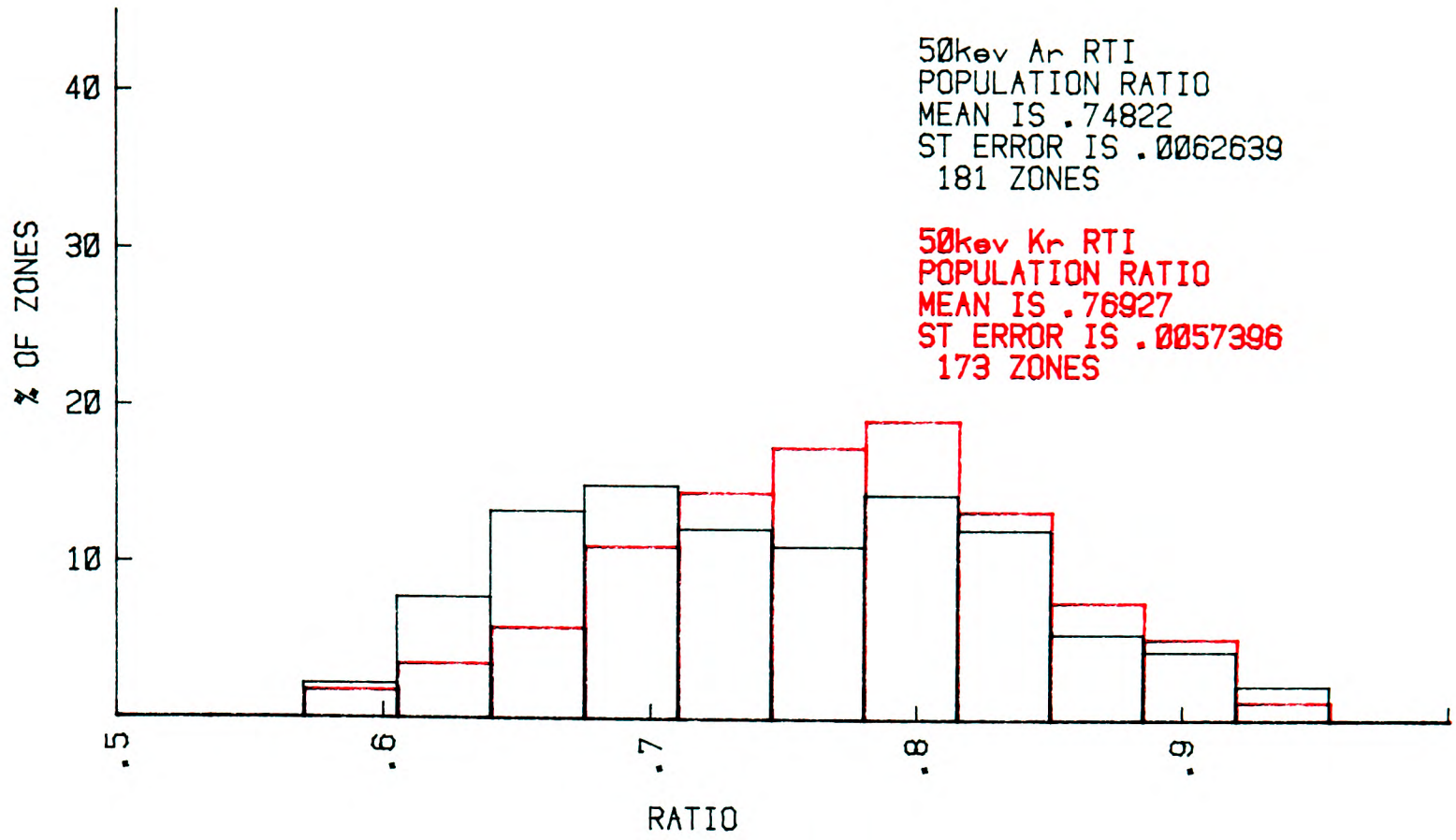
50kev Ar RTI
POPULATION RATIO
MEAN IS .74822
ST ERROR IS .0062639
181 ZONES
50kev Kr RTI
POPULATION RATIO
MEAN IS .76927
ST ERROR IS .0057396
173 ZONES
% OF ZONES
40
30
20
10
.5
.6
.7
.8
.9
RATIO

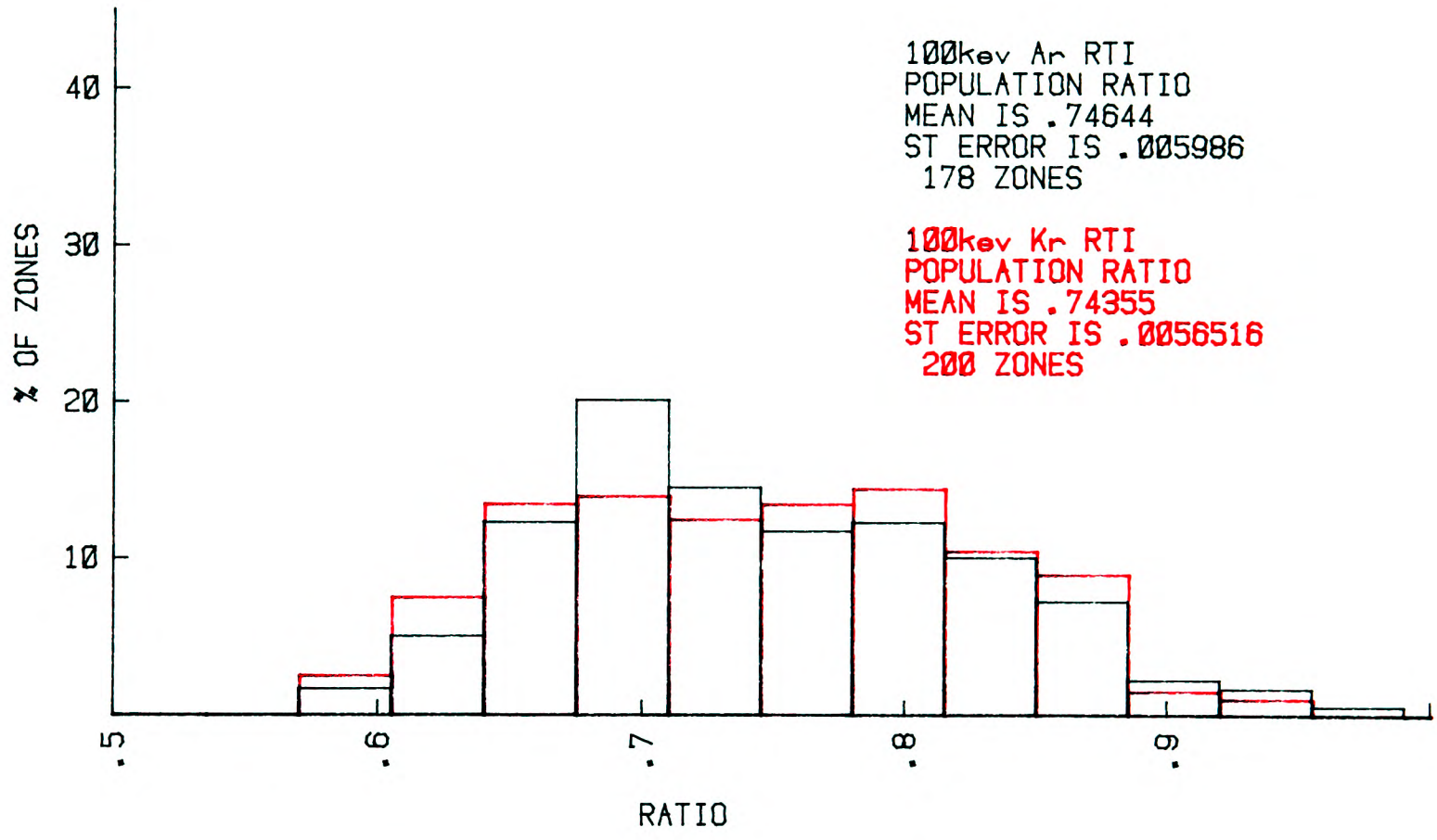
100kev Ar RTI
POPULATION RATIO
MEAN IS .74644
ST ERROR IS .005986
178 ZONES
100kev Kr RTI
POPULATION RATIO
MEAN IS .74355
ST ERROR IS .0056516
200 ZONES
% OF ZONES
40
30
20
10
.5
.6
.7
.8
.9
RATIO

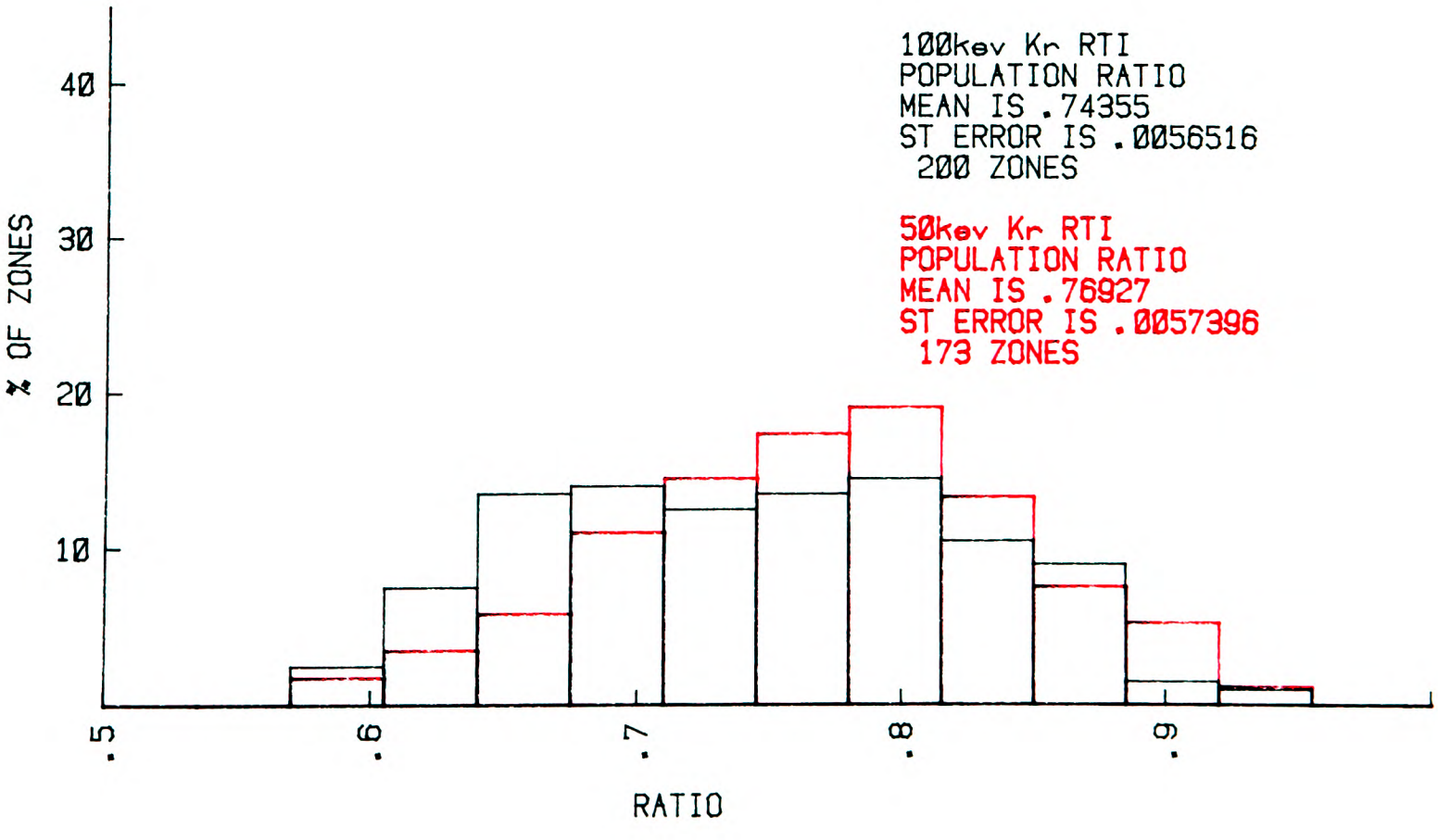
100kev Kr RTI
POPULATION RATIO
MEAN IS .74355
ST ERROR IS .0056516
200 ZONES
50kev Kr RTI
POPULATION RATIO
MEAN IS .76927
ST ERROR IS .0057396
173 ZONES
% OF ZONES
40
30
20
10
.5
.6
.7
.8
.9
RATIO

	50keV Ar	50keV Cu	50keV Kr	100keV Ar	100keV Kr
Mean number of subzones per zone	1.40	1.23	1.31	1.46	1.43

TABLE 6.8 Incidence of subzones for each room temperature irradiation condition.

	Low Temp Irradiation 50keV Cu	Room Temp Irradiation 50keV Cu	Room Temp Irradiation 100keV Kr
Mean Image Width	51 ±2	52 ±2	64 ±2
Maximum Image Width	64 ±3	64 ±2	81 ±3

TABLE 6.9 Kinematical image widths of loops

		50keV Ar	50keV Cu	50keV Kr	100keV Ar	100keV Cu	100keV Kr
(a)	$\langle X \rangle_D$	90	103	91	158	179	150
	$\sqrt{\langle \Delta X^2 \rangle_D}$	62	66	56	109	115	92
	$\sqrt{\langle Y^2 \rangle_D}$	48	45	36	84	78	60
(b)	$\langle X \rangle_D$		97			170	
	$\sqrt{\langle \Delta X^2 \rangle_D}$		62			106	
	$\sqrt{\langle Y^2 \rangle_D}$		46			77	

TABLE 6.10 Mean damage distribution depths ($\langle X \rangle_D$) and widths parallel ($\sqrt{\langle \Delta X^2 \rangle_D}$) and perpendicular ($\sqrt{\langle Y^2 \rangle_D}$) to the ion beam. Using (a) a mean atomic weight for Cu_3Au and, (b) a true diatomic calculation.

Fig 6.5 Mean diameter distributions illustrating that higher energy zones are larger than those produced by lower energy ions.

(a)

(b)

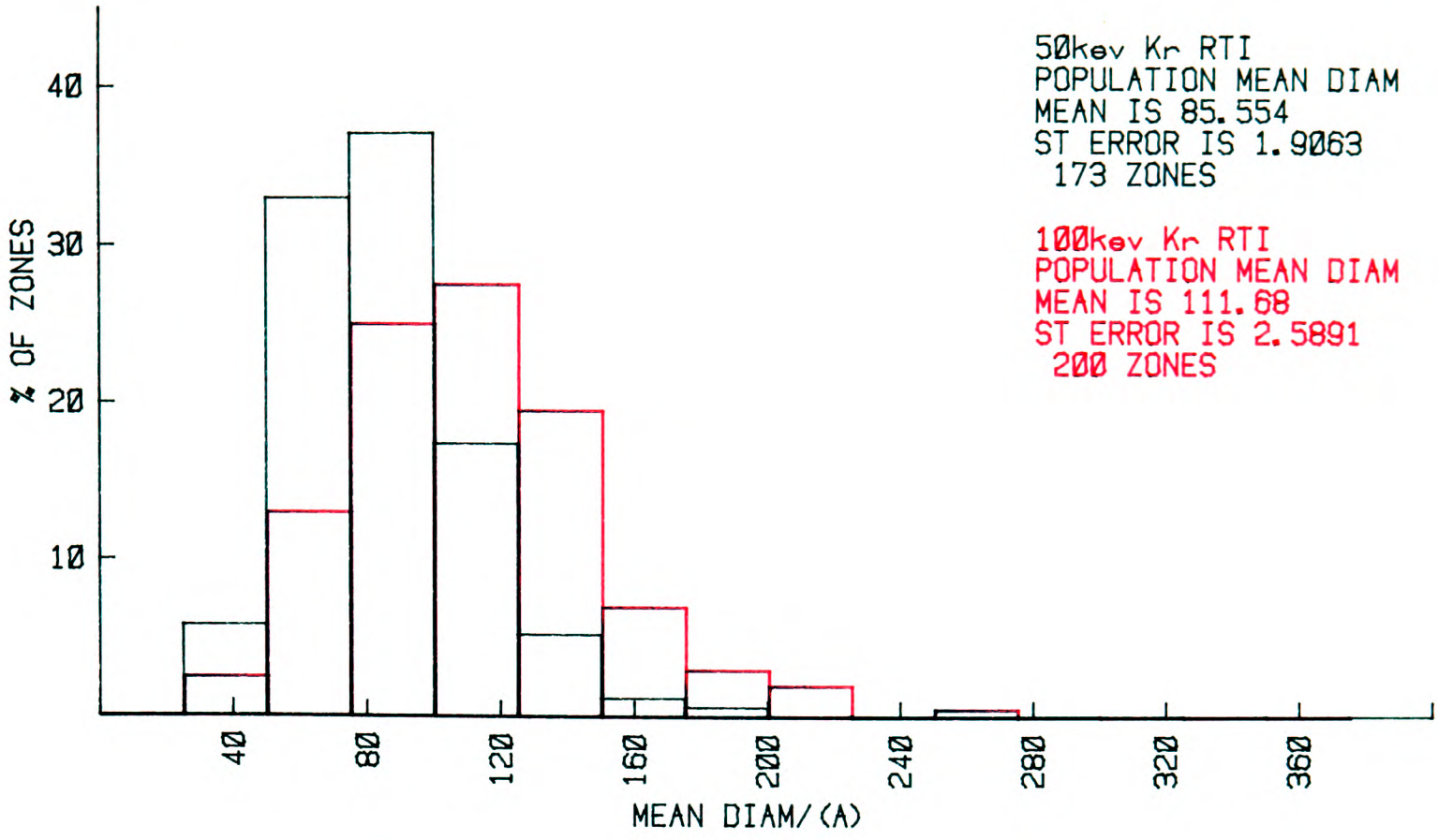
50kev Kr RTI
POPULATION MEAN DIAM
MEAN IS 85.554
ST ERROR IS 1.9063
173 ZONES
100kev Kr RTI
POPULATION MEAN DIAM
MEAN IS 111.68
ST ERROR IS 2.5891
200 ZONES
% OF ZONES
40
30
20
10
40
80
120
160
200
240
280
320
360
MEAN DIAM/(A)

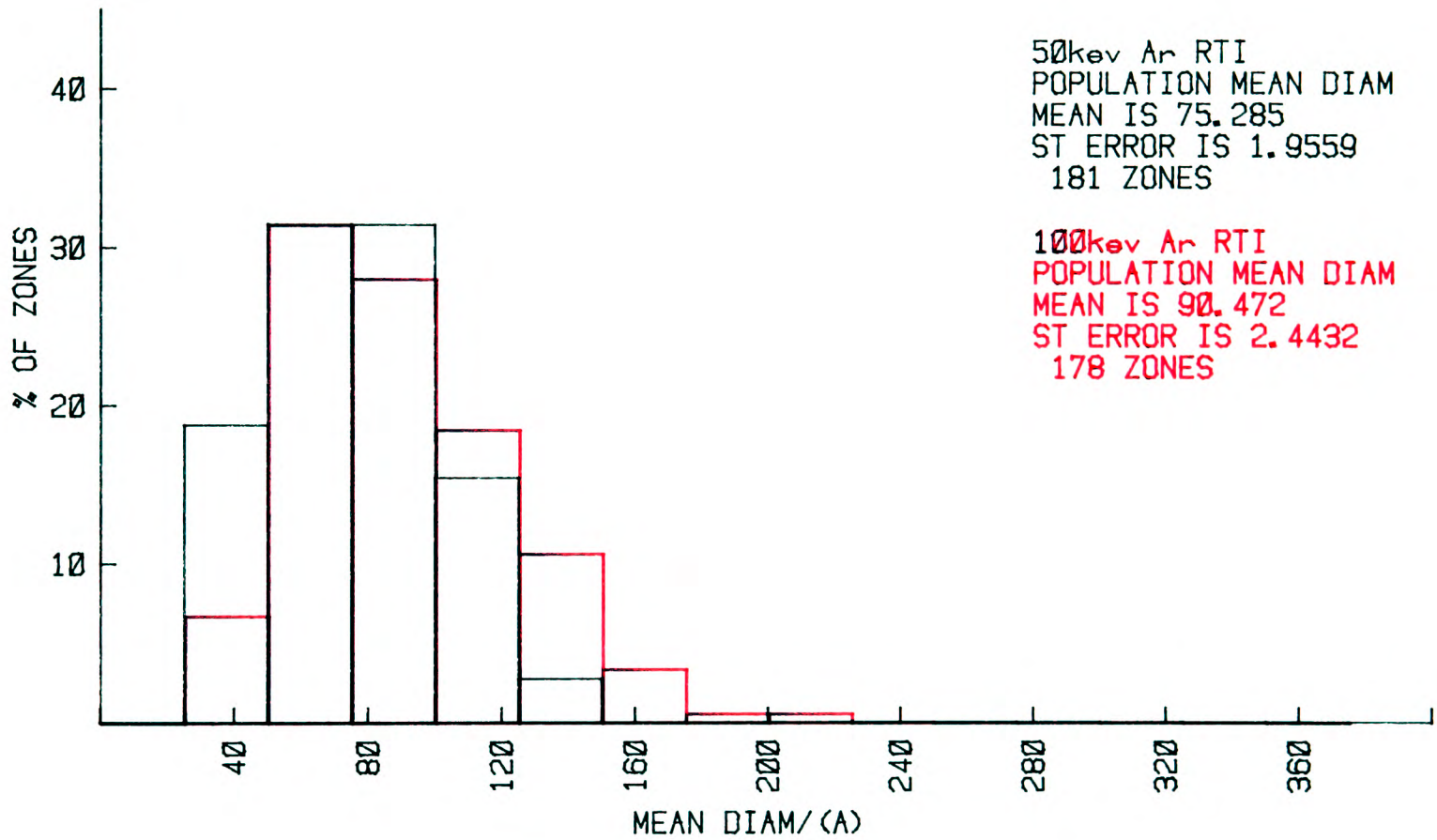
50kev Ar RTI
POPULATION MEAN DIAM
MEAN IS 75.285
ST ERROR IS 1.9559
181 ZONES
100kev Ar RTI
POPULATION MEAN DIAM
MEAN IS 90.472
ST ERROR IS 2.4432
178 ZONES
% OF ZONES
40
30
20
10
40
80
120
160
200
240
280
320
360
MEAN DIAM/(A)

numbers of subzones than their lower energy counterparts indicating less regular zones at 100keV.

In view of this result that higher energy ions produce larger disordered zones, it may be regarded as a little surprising that no change in defect yield is observed on doubling the energy. This point will be investigated further in the next chapter.

6.3.4 Correlation between Zone Size and Irradiation Temperature

In each of the three cases where zones produced at room temperature and those produced at low temperature (though imaged at room temperature) by the same ions could be compared, the room temperature zones were larger. This effect, though present, was not particularly pronounced in the 100keV Ar case although it is significantly greater for 50keV Cu and Kr, as can easily be seen by comparing Table 6.6(a) with 6.7(a) and from Fig 6.6.

Interestingly, the 50keV Kr low temperature zones are smaller than the 50keV Cu low temperature zones in contrast to the room temperature trend.

Again, this effect, coupled with the respective defect yields is entirely consistent with the observation that larger disordered zones are more likely to contain loops.

As far as zone shapes are concerned, no consistent trends with irradition temperature are obvious.

Fig 6.6 Mean diameter distributions indicating that zones produced at room temperature are larger than those generated at low temperature.

(a)

(b)

(c)

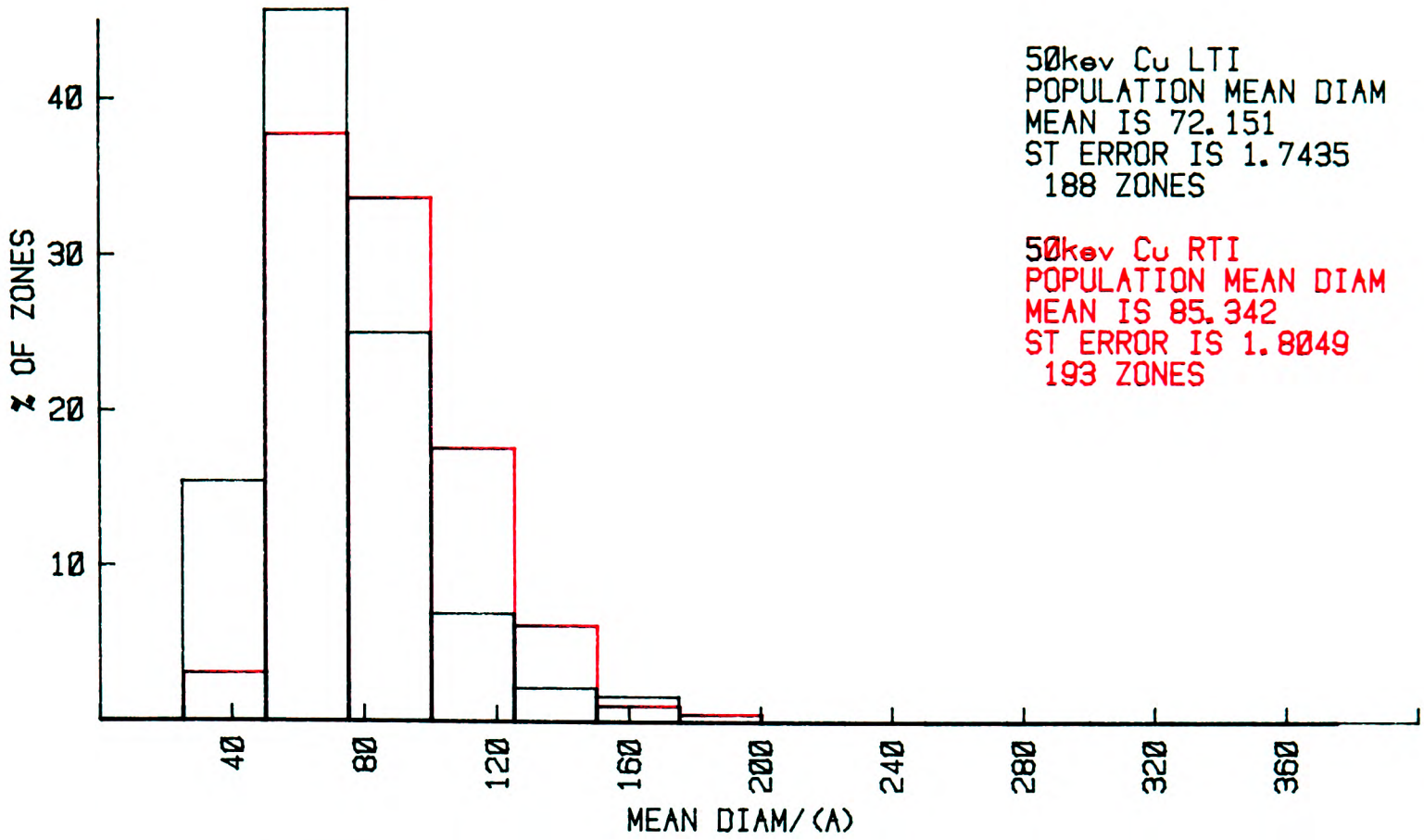
50kev Cu LTI
POPULATION MEAN DIAM
MEAN IS 72.151
ST ERROR IS 1.7435
188 ZONES
50kev Cu RTI
POPULATION MEAN DIAM
MEAN IS 85.342
ST ERROR IS 1.8049
193 ZONES
% OF ZONES
10
20
30
40
40
80
120
160
200
240
280
320
360
MEAN DIAM/(A)

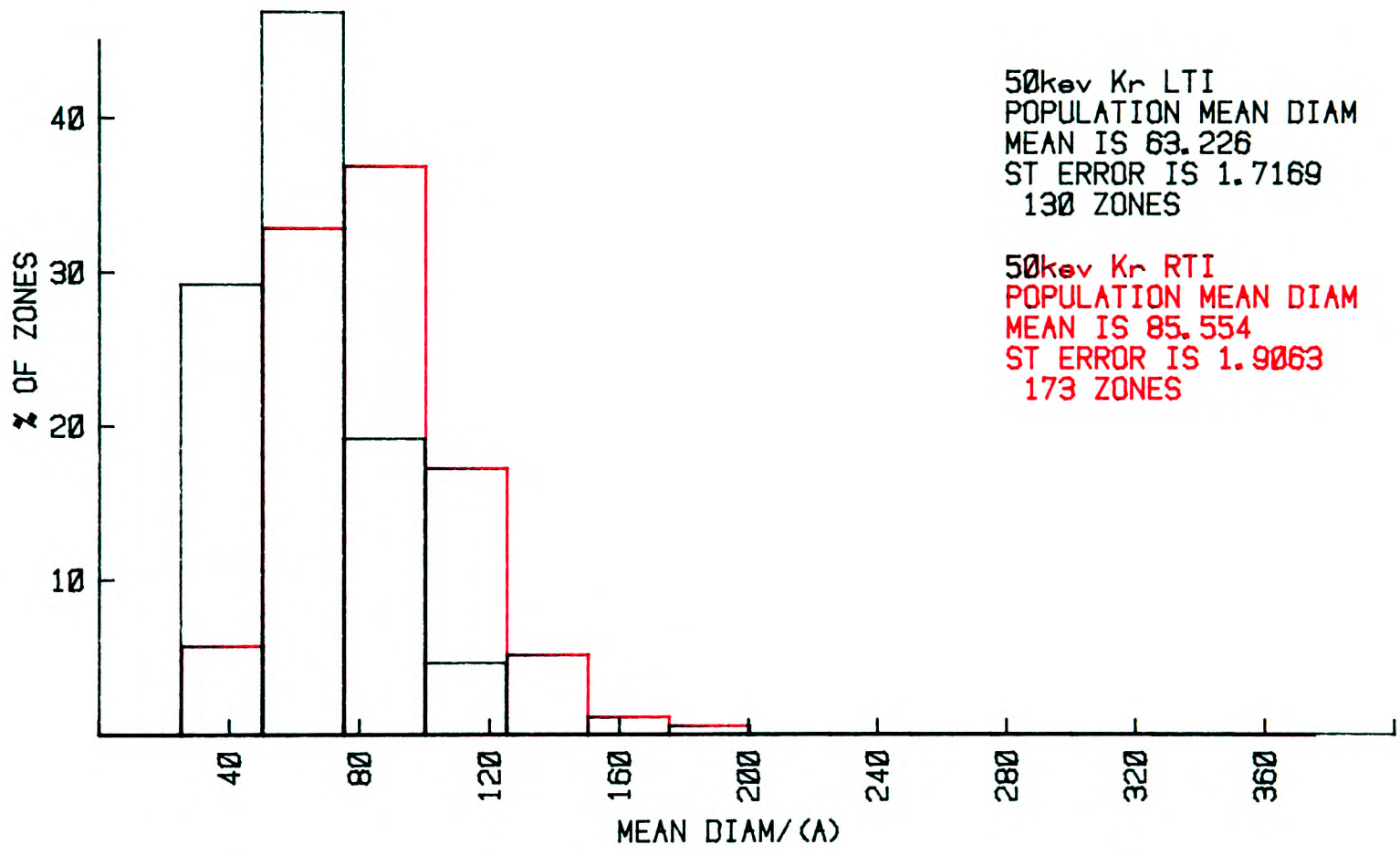
50kev Kr LTI
POPULATION MEAN DIAM
MEAN IS 63.226
ST ERROR IS 1.7169
130 ZONES
50kev Kr RTI
POPULATION MEAN DIAM
MEAN IS 85.554
ST ERROR IS 1.9063
173 ZONES
% OF ZONES
10
20
30
40
40
80
120
160
200
240
280
320
360
MEAN DIAM/(A)

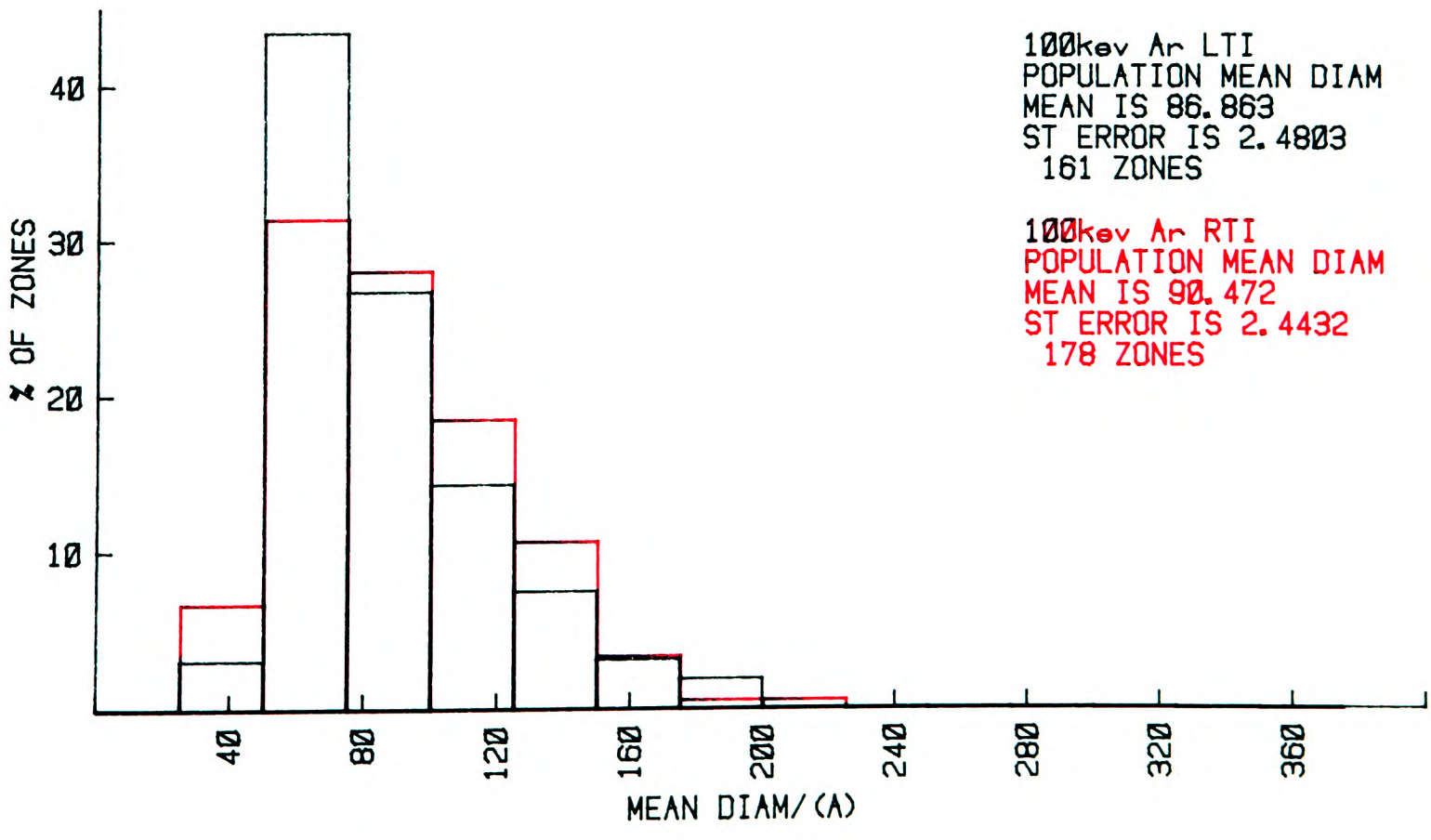
100kev Ar LTI
POPULATION MEAN DIAM
MEAN IS 86.863
ST ERROR IS 2.4803
161 ZONES
100kev Ar RTI
POPULATION MEAN DIAM
MEAN IS 90.472
ST ERROR IS 2.4432
178 ZONES
% OF ZONES
10
20
30
40
40
80
120
160
200
240
280
320
360
MEAN DIAM/(A)

6.3.5 Loop-Sizes

Loop populations from the 50keV Cu RTI, 50keV Cu LTI and 100keV Kr RTI irradiation conditions were sized from kinematical micrographs, shown in Fig 6.7 and the results are given in Table 6.9. As the procedure for obtaining the real loop diameter from its kinematical image width is a somewhat unreliable one [Jäger 1981], the values quoted are uncorrected image widths. The most obviously striking result is that the loops produced by 50keV Cu ions are independent of irradiation temperature, in agreement with the observations of Laupheimer et al [1981]. This makes the result that disordered zone sizes differ in the two cases (Section 6.3.4) even more interesting and removes any possibility that this is due to some imaging artefact.

Additionally, the loops produced by 100keV Kr ions have ~23% larger mean diameters than those produced by 50keV Cu.

6.3.6 Errors and Limitations

As discussed in Section 5.5.2 the disordered zones examined in each population had a spread of sizes and shapes due to the range of knock-on energies produced by the ions. The errors given in Tables 6.6 and 6.7 are simply the standard deviations of the distributions measured. In addition to these random errors, three possible sources of systematic error have been identified:

(i) Assessment of zone perimeter.

When the digitizing process described in Chapter

Fig 6.7 Examples of the kinematical loop images used for sizing:

(a) 50keV Cu LTI

(b) 50keV Cu RTI

(c) 100keV Kr RTI

Fig 6.8 Examples of (a) collapsed and (b) uncollapsed zones from the 100keV Kr RTI condition.

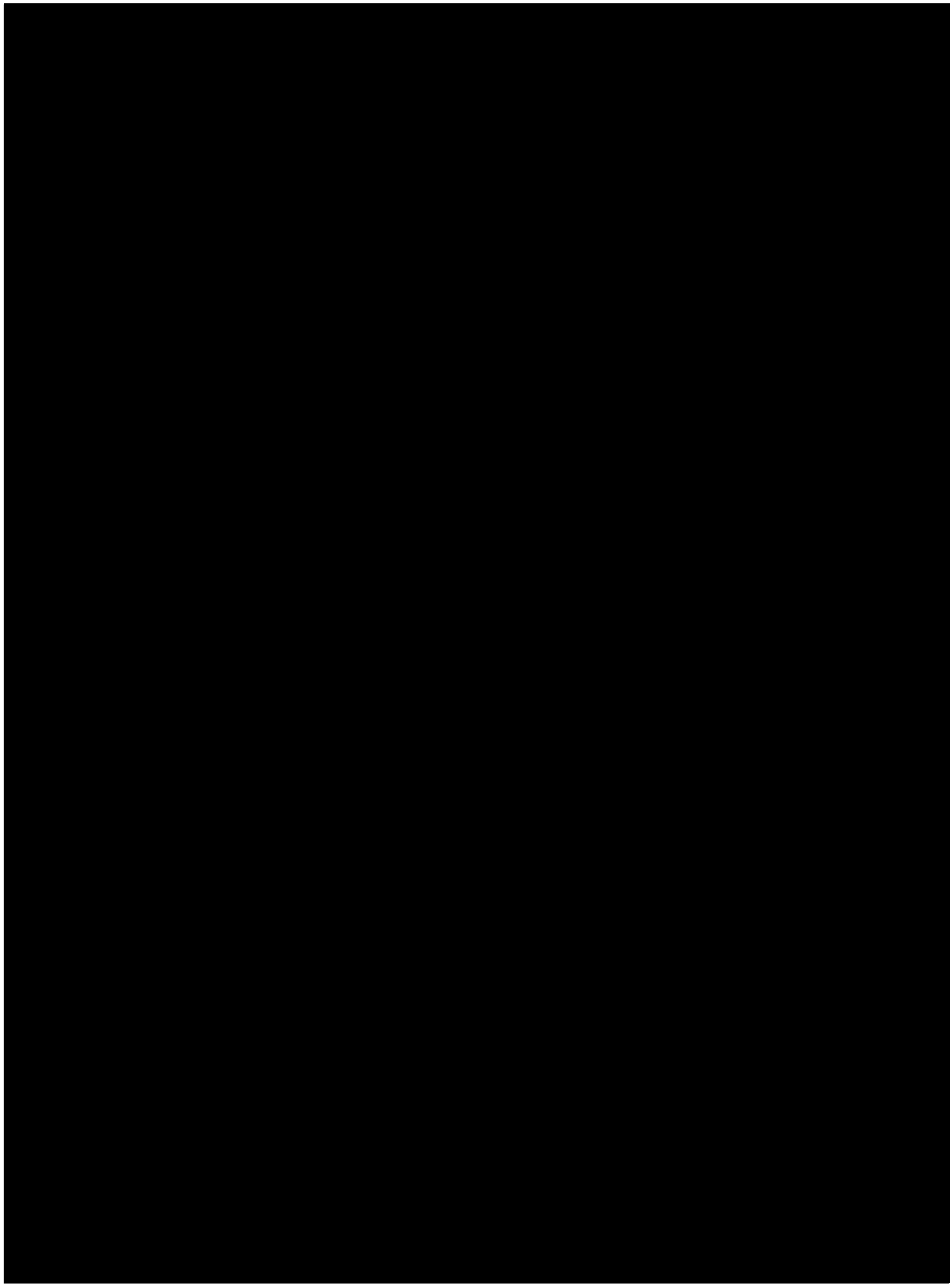

A.E.R.E. HARWELL

PHOTOGRAPHIC GROUP

HR 1514

NOT FOR PUBLICATION

Five is effected, a subjective assessment of where a zone perimeter lies must be made. This must inevitably lead to some uncertainty in the values given in Tables 6.6 and 6.7. However, as this assessment was carried out in as consistent a manner as possible for all irradiation conditions, its effect should be similar in all cases. Thus, the relative differences in zone size which have been identified are likely to be independent of this effect.

(ii) Displacement cascades intersecting the lower foil surface and thus not being wholly contained.

This may result in a smaller size distribution being obtained than would occur in bulk specimens. However, inspection of Table 6.10 indicates that this is unlikely to occur. The figures given in the first three rows of this table have been calculated from the W.S.S. analytical theory by using a weighted average of Cu and Au to obtain the effective mass of Cu_3Au. (The last three rows give the dimensions obtained by using a true diatomic calculation based on W.S.S., (Winterbon; Private Comm.) illustrating tnat the averaging procedure applied in the other cases is a good approximation.) Of the five cases analysed, the 100keV Ar ions are expected to produce the deepest damage layer and even this should not penetrate beyond ~260Å ($\langle x \rangle_D + \sqrt{\langle \Delta x^2 \rangle_D}$). For this reason it is believed that no systematic error has resulted

from this effect.

(iii) The possibility that loops present in collapsed cascades produce an increase in image width of the disordered zone.

If the presence of a loop in a disordered zone were to produce a large increase in disordered zone image width, the significance of the result given in Section 6.3.1 (i.e. that larger zones collapse more readily) must be questioned. Additionally, the results that heavier ions produce larger zones and that room temperature irradiations produce larger zones than low temperature irradiations could conceivably be attributed simply to differences in defect yields. (The ion energy effect identified in Section 6.3.3 should not be affected since defect yields do not vary between 50keV and 100keV.)

However, if uncollapsed populations are investigated (i.e. only those zones which do not contain a loop) the previously identified trends are still present. Table 6.6(c) illustrates that 50keV Ar zones are still over 10% smaller than 50keV Cu or Kr and that zones produced at low temperature are still much smaller than their room temperature counterparts. It is concluded therefore that the ion mass and irradition temperature effects identified in Sections 6.3.2 and 6.3.4 respectively are genuine effects and not artefacts due to the presence of

loops.

With respect to the effect reported in Section 6.3.1, it is unlikely that an increase of almost 50% in the mean diameter of a zone (as is the case in the 100keV Kr room temperature irradiation case) could be produced by the presence of a loop without altering the zone appearance appreciably. Fig 6.8 demonstrates that the collapsed zones, though larger, show no evidence of loop-produced strain contrast.

Support for the conclusion that loops do not significantly affect disordered zone images has already been reported. Jenkins et al [1976] used a Bloch wave approach to compute g=<110> image intensities for disordered zones containing dislocation loops and also carried out various contrast experiments in the TEM. The conclusion drawn was that under the conditions of the current experiments, the structure factor contrast dominated the image and that the effect of small dislocation loops within disordered zones can be neglected.

By using some unpublished calculations kindly provided by Dr M. L. Jenkins (displayed graphically in Fig. 6.9), it was possible to estimate the size of the effect in the 100keV Kr case. The result of this is given in Appendix 6.3, from which it is clear that a loop present in a disordered zone is unlikely to cause an increase in image width of

Fig 6.9 {110} dark field image intensities for:

(A) Disordered zones alone

(B) Disordered zones containing loops.

(a) A 100Å diameter zone containing a 50Å diameter, edge-on Frank loop.

(b) A 75Å diameter zone containing a 50Å diameter, edge-on Frank loop.

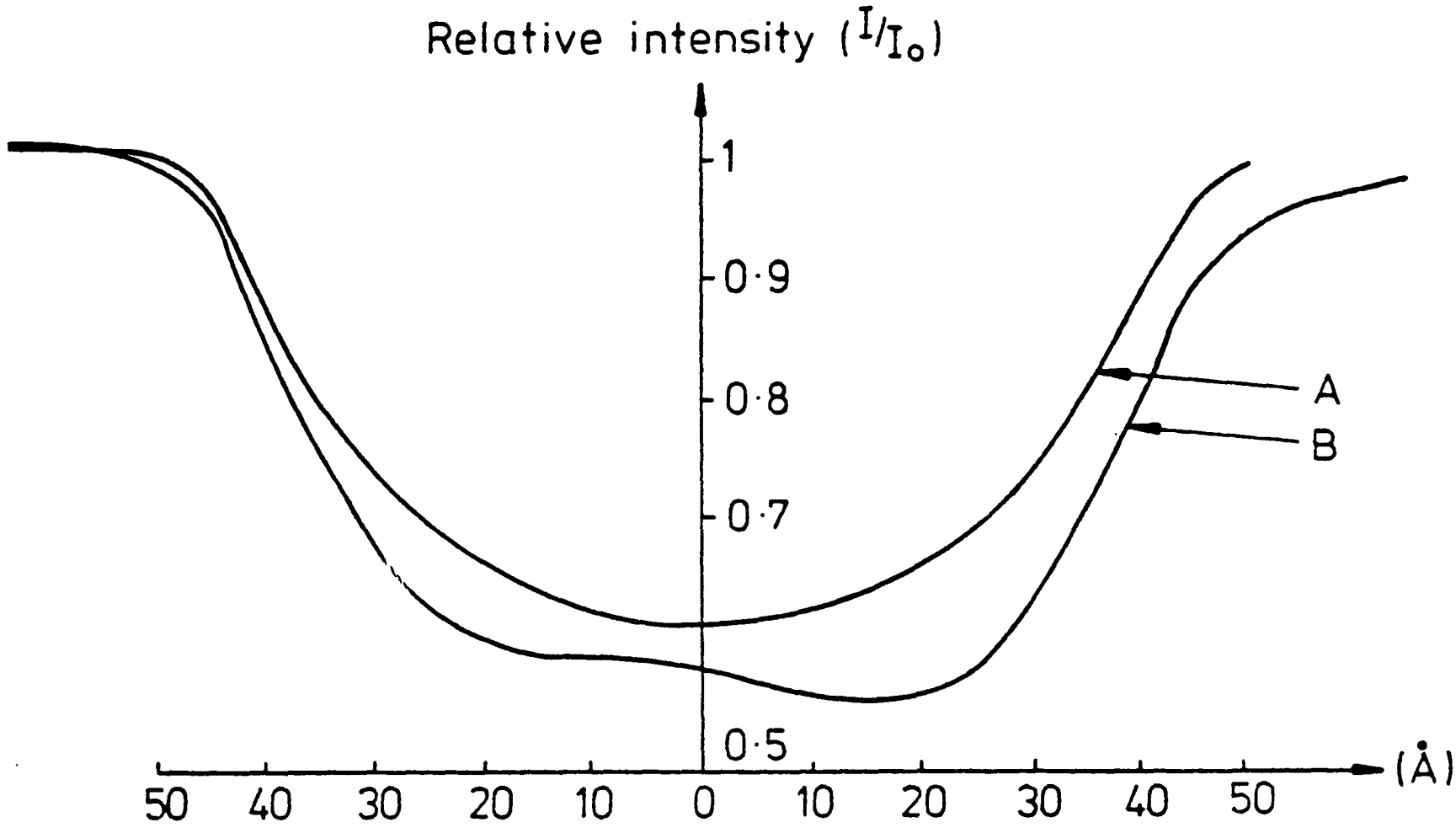
Relative intensity (I/I_o)
1
0·9
0·8
0·7
0·5
A
B
50 40 30 20 10 0 10 20 30 40 50
(Å)

(a)

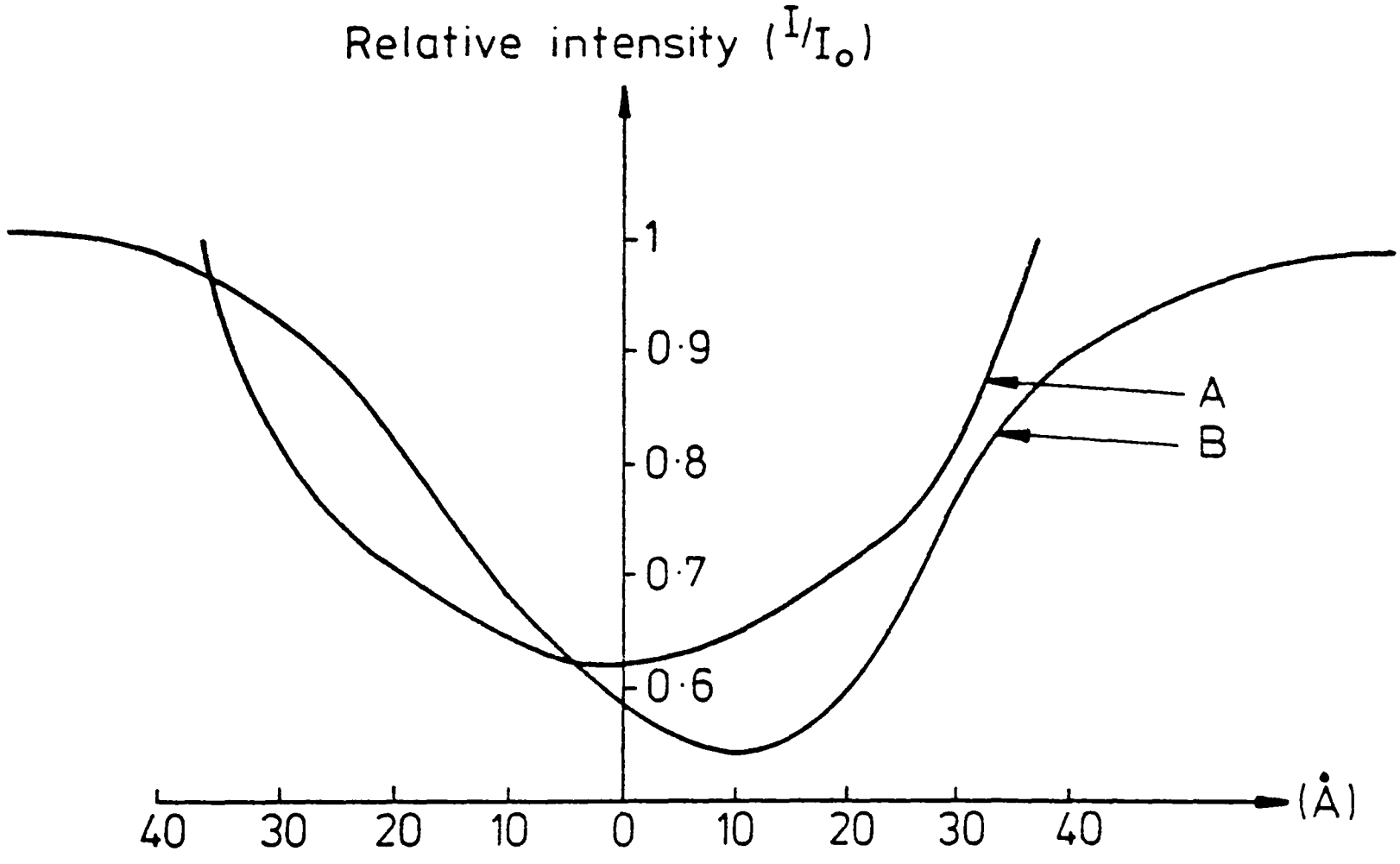
Relative intensity (I/I_o)
1
0·9
0·8
0·7
0·6
A
B
40 30 20 10 0 10 20 30 40
(Å)

(b)

greater than 10% and can in no way account for the 48% observed. This demonstrates that the effect reported in Section 6.3.1 is a real one, and not an artefact due to the presence of loops.

6.4 SUMMARY OF RESULTS

The significant results contained in the preceeding sections may be summarised as follows:

(i) Collision cascades produced at low temperature collapsed to dislocation loops with moderately high probability even when no thermally activated point defect mobility is possible.

(ii) No further increase in collapse is observed with subsequent warming of the cascades.

(iii) Collision cascades produced at room temperature are more likely to collapse than those produced at low temperature.

(iv) Collision cascades produced by heavier ions are more likely to collapse than those produced by lighter ions.

(v) A change in ion energy from 50 to 100keV does not alter the likelihood of collapse.

(vi) Within any single irradiation condition the larger disordered zones are more likely to have collapsed.

(vii) Increases in ion mass, ion energy and irradiation

temperature all result in larger disordered zones being produced.

(viii) Despite disordered zone diameters increasing, dislocation loop diameters are unaffected by increases in irradiation temperature.

APPENDIX 6.1

The Magnitude of Beam Heating Effects

Fisher [1970] derives an expression for the maximum rise in temperature which may be encountered in a thin foil subject to an electron beam.

$$\Delta T = \frac{I_o a^2}{4k} \{ \nu_o + \log_e (b/a)^2 \} Q$$

Where Q is the energy loss of the electrons per unit penetration and is given by:

$$Q = 0.153 \rho \frac{Z}{A\beta^2} \left\{ \log_e \left[\frac{E(E + m_e c^2)^2 \beta^2}{2I^2 m_e c^2} \right] + (1 - \beta^2) - [2 - (1 - \beta^2)^{1/2} - 1 + \beta^2] \log_e 2 + 1/8 [1 - (1 - \beta^2)^{1/2}]^2 \right\} \text{MeVcm}^{-1}$$

Where:

ρ	= Foil density	$= 12.38 \text{gcm}^{-3}$
k	= Foil thermal conductivity	$= 0.63 \text{Wcm}^{-1}\text{K}^{-1}$ (at 83K)
Z	= Atomic number	
A	= Atomic weight	Z/A = 0.44
I	= Excitation energy	= 856eV
I_o	= Electron beam flux	$= 2.2 \times 10^{19} \text{ecm}^{-2}\text{s}^{-1}$
a	= Beam radius	$= 2.8\mu\text{m}$
b	= Distance to heat sink	$= 30\mu\text{m}$
E	= Beam energy	= 300keV
β	= v/c	= 0.78
$m_e c^2$	= Electron rest energy	= 0.512MeV
ν_o	= Euler's constant	= 0.577

ρ and k are taken from Gmelins Handbuch.

Z/A and I are interpolated between Cu and Au for Cu_3Au.

I_o was experimentally measured by intercepting the beam with a faraday cup.

a was found by photographing a low magnification image of a fully focused beam.

b is taken as the maximum possible distance between any point on the specimen and the nearest bar of the Cu grid supporting it.

Thus, Q reduces to:

$$16.04 \text{MeVcm}^{-1} = 2.57 \times 10^{-12} \text{Jcm}^{-1}$$

giving a value of:

$$T = 9.2\text{K}$$

APPENDIX 6.2

The magnitude of electron beam induced vacancy mobility.

Micrographs showing the presence of dislocation loops were obtained from areas of specimen which had been exposed to only a very diffuse electron beam for less than 60s [Fig 6.1]. The purpose of this calculation is to demonstrate that these loops cannot possibly have been formed by beam induced vacancy motion within the vacancy rich cascade core.

The number of electron-atom collisions within the cascade volume in which the atom receives over a certain kinetic energy T is given by:

$$N = nI_oV\sigma(T)$$

Where:
- n = Atomic density of specimen
- $\sigma(T)$ = Cross section for such collisions
- I_o = Electron flux
- V = Cascade volume

So that if the cross section for all collisions imparting energies above the vacancy migration energy is used, a rough estimate of the number of vacancy jumps expected in the cascade region may be made. Allowance must be made for the fact that not all such collisions will cause vacancy movement since not all the atoms in the cascade region have vacancy nearest neighbours.

Thus the number of vacancy jumps is given by:

$$N = nI_oVp\sigma(T)$$

Where:
- p = Probability that an atom has a vacancy nearest neighbour in the cascade region.

A 100keV cascade contains ~1000 vacancies (modified Kinchin & Pease) in a sphere of diameter ~100Å. Such a sphere will contain $\sim 10^5$ atoms. So, since the co-ordination number is 12 in f.c.c.:

$$p = \frac{10^3}{10^5} \times 12 \sim 0.1$$

(The inherent assumption that an atom receiving the vacancy migration energy can move into all 12 of its neighbouring sites is obviously erroneous and will probably lead to an over-estimate of p.)

Now, for a defocused beam of measured diameter d ~ 100 μm, the electron flux is approximately:

$$I_o \sim 10^{16}\ ecm^{-2}\ s^{-1}$$

Urban [1979] gives a value for the cross section for Cu atoms at 300keV as:

$$\sigma \sim 4 \times 10^{-21} \text{ cm}^2$$

(As the cross section for Au is $\sim 1 \times 10^{-21}$ cm^2 this will overestimate N.)

The volume of a cascade of diameter 100Å is:

$$V \sim 4 \times 10^{-18} \text{ cm}^3$$

and the atomic density in Cu_3Au is:

$$n = 7.6 \times 10^{22} \text{ atoms cm}^{-3}$$

Thus, the number of vacancy jumps in the cascade region per second is:

$$N = 7.6 \times 10^{22} \times 4 \times 10^{-21} \times 10^{16} \times 4 \times 10^{-18} \times 0.1$$

Therefore:

$$N \sim 1 \text{ jump sec}^{-1}$$

Given that the formation of a vacancy loop from the diffuse vacancy core of an uncollapsed cascade must require considerably more than 60 vacancy jumps, the loops imaged within 1 minute of the electron beam being applied cannot be accounted for by this mechanism. This same conclusion was reach by Howe et al [1966] operating under similar experimental conditions.

APPENDIX 6.3

The Effect of Strain Contrast on Disordered Zone Imaging.

The model of Jenkins et al [1976] assumes a spherical disordered zone comprising two distinct regions. The central core is considered to be completely disordered with the zone periphery linearly increasing in order up to the perfect order of the lattice. The scattering matrix method is used to obtain the <110> diffracted beam intensity which is then plotted as a function of position. Fig. 6.9 shows two examples of such contrast profiles for a 100Å and a 75Å disordered zone. Inspection of this figure indicates that although the contrast profile may be influenced by the presence of a dislocation loop, it maintains the size and shape of the structure-factor contribution fairly well.

In order to estimate the likely increase in image width which results from the presence of the dislocation loop, two procedures have been followed:

(a) The region of maximum contrast gradient is detected on either side of the profile, and a linear extrapolation from this point to the background level is effected. (The line has the same gradient as the maximum gradient of the curve.) The distance between the two points at which these lines intercept the background level is then taken as the image width.

(b) The depth of the contrast profile is measured and a cutoff level of 15% (of the depth) determined. The distance across the profile at the 15% level is then taken as the image width.

The first of these is designed to estimate the effect assuming the eye is sensitive to contrast gradients with the second assuming sensitivity to relative levels above background.

In the case of a 50Å loop in a 100Å zone (Fig 6.9(a)) these two procedures lead to (a) 2% and (b) 4% increases in image widths. For a 60Å loop in a 100Å zone, the values increase slightly to (a) 4% and (b) 10%.

In the 100keV Kr room temperature irradiation case loops of image width 64Å were measured which probably corresponds to a real loop diameter of ~50-60Å [Rühle 1969]. Also, the measured zone sizes ranged from 81Å (uncollapsed) to 120Å (collapsed) with a value for the total population of 112Å.

It is felt that the two loop/zone configurations used above describe the real situation reasonably well. However, even if an unrealistically low value for zone width is used (A 50Å loop in a 75Å zone produces an increase of ~20% in zone image width; Fig 6.9) the 48% observed cannot be achieved.

If the same calculations are applied to the 50keV Cu case (78Å zone, 40-50Å loop) an increase in image width of ~8% is found, whereas the observed difference is ~15%.

CHAPTER SEVEN

DISCUSSION

7.1 INTRODUCTION

In Chapter Two it was indicated that the time evolution of the cascade has been established as occurring in four phases. These have been identified as: point defect production by collisions; the attainment of local thermal equilibrium; the cooling of the cascade volume to ambient lattice temperatures and the annealing of remaining defects if the ambient lattice temperature is sufficiently high. Their durations are considered to be of the order:

Collision Phase	$\sim 10^{-13}$ s
Relaxation Phase	$\sim 5 \times 10^{-13}$ s
Cooling (Spike) Phase	$10^{-12} - 10^{-10}$ s
Annealing Phase	$10^{-9} - 10^{-7}$ s

Although the identification of these four phases has been made by several authors, the end of each phase and beginning of the next is somewhat nebulous and overlap is known to occur. In the present experiments, the annealing phase does not occur for the low temperature irradiations and since in Cu_3Au, interstitials are mobile at ~75K and vacancies at ~330K [Takamura and Okuda 1973; Gilbert et al 1973], no appreciable thermally induced vacancy motion is expected to occur even in the room temperature irradiations.

As cascade collapse has been observed even at low temperature,

where all point defects are frozen, it must be concluded that collapse is occurring at some point during the first three phases, i.e. within 10^{-10}s of the initiation of the cascade. The problem associated with this conclusion is that even at temperatures around the melting point of Cu_3Au, the thermally induced vacancy jump rate is expected to be orders of magnitude below that required to produce significant vacancy agglomeration within 10^{-10}s from the vacancy configurations known to exist at the end of the collision phase.

In the subsequent sections it is proposed to explain the observed disordered zone sizes and cascade collapse behaviour by considering the atomic motion which may occur during the various phases of the cascade. The observations which require explanation are:

(i) For all irradiation conditions studied, disordered zones are produced by the incident ions.

(ii) Increases in ion mass, ion energy and irradiation temperature all result in larger disordered zones being produced.

(iii) Cascade collapse occurs at temperatures at which vacancies and interstitials are unable to undergo long range migration in the lattice.

(iv) Increases in ion mass and irradiation temperature increase the probability of collapse.

(v) A change in ion energy from 50 to 100keV does not alter the probability of collapse.

Points (i) and (ii) are examined in Section 7.2 under the heading of "Disordering" whereas (iii), (iv) and (v) are postponed to Section 7.3 under "Cascade Collapse".

Before embarking on this, some insight can be gained from consideration of theoretical cascade parameters. The relevant parameters, as given by the WSS analytical theory (which deals with cumulative average cascades - Chapter Two) are presented in Table 7.1. The predicted cascade diameter (perpendicular to the ion beam), volume, energy density and lifetime are given. The first two having been calculated using Winterbon et al [1970] and the remaining two from Sigmund [1974]. The relevant points which should be noted from this table are that WSS predicts:

(i) Cascades produced by heavier ions are spatially more compact, have higher energy densities and shorter lifetimes than those produced by lighter ions.

(ii) Cascades produced by lower energy ions are smaller, have higher energy densities and shorter lifetimes than those produced by higher energy ions.

The first of these trends, has been confirmed both by Field Ion Microscope (FIM) studies [Wei et al 1981], and by binary computer simulations [Walker and Thompson 1978]. In the FIM work, tungsten was bombarded with ions from Ar to W and a monatonic decrease in cascade dimensions was observed with increasing ion mass. In the computer simulations, various 20keV ions were "implanted" into Si and the same trend was

	50keV Ar	50keV Cu	50keV Kr	100keV Ar	100keV Cu	100keV Kr
Observed Zone Diameter (Å)	75	85	86	90	-	112
WSS Cascade Diameter (Å)	95	90	73	168	156	120
WSS Cascade Volume ($x10^5 Å^3$)	5.8	5.6	3.1	32	29	14
WSS Energy Density (eV/atm)	0.23	1.43	3.72	0.06	0.29	1.15
WSS Cascade Lifetime($x10^{-11}$s)	4	0.6	0.2	35	5	2

TABLE 7.1 Measured and calculated cascade parameters

	50keV Ar	50keV Cu	50keV Kr	100keV Ar	100keV Cu	100keV Kr
Number of Vacancies (NRT)	740	800	820	1480	1600	1640
Vacancy conc. (NRT/WSS) at %.	1.7	1.9	3.5	0.6	0.7	1.6
Cascade Efficiency		0.37				0.29

TABLE 7.2 Data on vacancies in each case

observed. With respect to the second trend identified, the FIM and simulation studies have confirmed that cascade dimensions increase as the ion energy is increased.

However, as pointed out in Chapter Two, the fact that WSS predicts the behaviour of cumulative average cascades, and must therefore overestimate cascade dimensions, requires that care be exercised when considering Sigmund energy densities. This overestimation is more significant in cascades of low energy density such as are produced by high energy or light ions, as in such cases simulations have indicated that sub-cascade formation is more common. Thus, in 100keV cascades it is expected that there will exist local regions, within which the energy density is comparable to that of the 50keV cascades. Similarly, in the diffuse cascades produced by such light ions as Ar, regions of energy density much in excess of that predicted by WSS may be expected.

Besides the quantities related to zone size, other relevant parameters are related to the number of vacancies created in a given cascade. Norgett et al [1972] derived a method for estimating the number of vacancies produced for a given ion/energy configuration, and this has been calculated for each of the conditions used in this study, (Table 7.2). A slight dependence on ion mass is observed, with heavier ions producing slightly greater numbers of vacancies due to reduced electronic stopping. Additionally, both computer simulation [Stuart et al 1976] and electron irradiation studies [Yoshida and Urban 1980] have demonstrated a systematic decrease in the displacement threshold energy, E_d as lattice temperature

increases. The work of Yoshida and Urban revealed a 35% decrease of E_d in Cu (from 17.5eV to 13eV) as the lattice temperature increased from 70K to 300K, which may result in around 35% more vacancies being generated in the low temperature cascades relative to the room temperature, provided a similar reduction in E_d occurs under cascade producing irradiation.

By combining the NRT predicted numbers of vacancies with the WSS volumes it is possible to obtain the average vacancy concentrations which are also given in Table 7.2. It is to be expected that these will be underestimates of vacancy concentration as WSS overestimates cascade volumes. Nevertheless, the trend predicted is observed by FIM observations [Wei et al 1981], in which 30keV W ions produced cascades with a vacancy concentration of 16 atomic % whereas Ar ions only resulted in 2 atomic %.

In summary, it may be said that under those conditions in which the Sigmund energy density is high (i.e. low ion energy or high ion mass) compact cascades tend to form, with the energy density probably being close to the Sigmund value. In the other extreme of low Sigmund energy densities (i.e. high ion energy or low ion mass), cascades are produced which, though on average more diffuse than those of nominally high energy density, tend to be smaller than predicted by WSS, and may contain subcascade regions of true energy density comparable to those which exist in cascades of nominally higher energy density.

It should also be mentioned at this point that the cascade

lifetimes given in Table 7.1 are likely to be underestimates, and that in fact the cooling phase of the cascade may last much longer than suggested by these figures. As outlined in Chapter Two, Chudinov et al [1977] have demonstrated that energy loss from cascades will not occur by such a group motion as heat conduction until the atomic velocities approach that of sound. This reduction in initial "temperature" leads to an increase in cascade lifetimes by up to an order of magnitude over the Sigmund values. However, the trends exhibited in Table 7.1 should still be correct. More compact cascades should lose their energy to the surrounding lattice at a higher rate than diffuse cascades, resulting in shorter lifetimes for high energy density cascades.

7.2 DISORDERING

7.2.1 Possible Mechanisms

The production of antisite defects (i.e. disordering) during a cascade may result from several mechanisms. The first of these is purely collisional in nature and as such, will only operate during the collision phase. The remainder would be expected to operate during the cooling or spike phases of the cascade:

(i) Production of replacement collision sequences along <110> directions resulting in rows of antisite defects.

The propagation of replacement collision sequences (RCS), in which each atom replaces its neighbour, along the <110> directions of an $L1_2$ lattice will

result in disorder as nearest neighbours along half of the <110> rows are of opposite types.

(ii) Random recombination of vacancy-interstitial pairs produced during the collision phase of the cascade.

The close proximity of vacancies and interstitials in cascades results in extensive recombination during the relaxation and cooling phases as observed by Guinan and Kinney [1981]. If such recombination is random, antisite defects will be produced.

(iii) High energy densities resulting in local melting (or at least appreciable atomic interchange) in the cascade during the cooling phase.

Provided the local atomic kinetic energies in the cascade region are high enough, atoms may leave their lattice sites, thus producing local melting. If subsequent recrystallization is random, a local disordered zone will result. Even if the atomic energies are below that required for melting, disordering may still result if they exceed those required for disordering in Cu_3Au.

(iv) Vacancy migration producing atomic motion which results in disorder.

The extensive vacancy migration which has been observed to occur in simulations (Chapter Two)

during the relaxation and cooling phases must result in atomic rearrangements and must therefore introduce disorder. It should be pointed out that if mechanism (iii) occurs, extensive vacancy migration may be expected to produce additional disorder after recrystallization.

The extent to which each of these four mechanisms may be expected to produce disorder will now be examined.

As replacement collision sequences are low energy events which occur at cascade peripheries, if the disordering were a direct result of RCS propagation, it would be expected that larger cascades would result in the production of larger disordered zones. However, the opposite of this has been observed with the Kr disordered zones being considerably larger than those produced by Ar ions. As the Ar cascades should be larger, it appears difficult to reconcile this observation with an RCS disordering mechanism.

Additionally, the fact that the disordered zones are larger at room temperature where the lengths of RCS will be reduced [Kapinos and Kevorkyan 1983], is not consistent with disordering by RCS. This is true even in the 100keV Ar condition, which, having the lowest Sigmund energy density, is the case where RCS disordering would be expected to have its greatest effect relative to mechanisms (iii) and (iv).

The observation of disordered zones in Nb_3Sn [Jenkins et al 1982], produced by 70keV Au ions which create cascades of energy density comparable to the lowest in the present study,

adds further weight to this argument, since the A15 structure of Nb_3Sn is such that nearest neighbours along close packed directions are of the same type. Thus, antisite defects cannot be produced by the passage of RCS. This has been confirmed by a fully dynamic computer simulation of the collision phase of a cascade in Nb_3Sn [Chudinov et al 1981], in which no reduction in long range order below S~0.9 was produced.

The second method proposed which may introduce disorder is the recombination of vacancy-interstitial pairs outlined in (ii) above. Disorder produced in this way must be confined within the boundaries of the collision phase of the cascade as insignificant recombination is expected beyond this. Again, the observation that heavier ions produce larger disordered zones, but are expected to have smaller cascades, indicates that such a recombination mechanism cannot account for the observed trends in disordered zone sizes. Furthermore, as the disordered zones produced by the 50keV Kr ions are larger than the cascade dimensions predicted by WSS (which is expected to overestimate cascade dimensions), there seems no way that recombination induced disordering can account for this. Such unexpectedly large disordered zones were also observed by Jenkins and English [1982] who found that zones produced by 70keV Au ions in Cu_3Au exceeded the WSS predicted dimensions.

The observation that zone sizes increase with increasing energy density, has led to the suggestion in (iii) above that the disordering may be attributed to the occurrence of local melting and subsequent recrystallization during the spike

phase of the cascade. As thermal disordering of Cu_3Au may result from several atomic interchange mechanisms including direct exchange, whereby two atoms change positions by employing interstitial locations [Brebec 1983], it is conceivable that disorder is generated at temperatures below the melting point. It is also expected that vacancy migration may play some role in the thermal disordering of Cu_3Au, so that overlap occurs between mechanisms (iii) and (iv).

Chudinov et al [1977] have considered the likelihood of local melting occurring in the cascade region. The conclusion drawn is that provided the region cools slowly enough, melting will result. The two major factors they identify which should slow the cooling rate, thus increasing the chances of melting, are increases in ambient lattice temperature, and increases in cascade size. A similar observation to the zone sizes exceeding the predicted cascade volume has been made by Averback [1982], who used resistivity measurements to monitor annealing of damage by cascade producing irradiation. He attributed the observed high annealing rates to leakage of energy beyond the cascade boundaries in the case of high energy densities. Furthermore, the observations that sputtering yields are often greatly in excess of that predicted by WSS [Chapter Two] have demonstrated that the energy deposited in the cascade is shared amongst many more atoms than the linear theory indicates. In particular, Merkle and Jager [1981] used TEM observations of surface craters in Au, produced by Bi ions, to examine the sputtering from individual cascades. Their conclusion was that within regions of the cascade, energy densities often exceeded that required for local sublimation

of the Au specimen. Even though Bi ion cascades in Au have a higher Sigmund energy density than any of the conditions used in the current experiments (6.7eV/atom at 100keV), the energies required to sublime Au are of the order of 5ev/atom, far in excess of those required to disorder Cu_3Au.

Given that the melting point of Cu_3Au is ~1250K, which corresponds to an atomic energy of ~0.11eV/atom, the energy densities given in Table 7.1 suggest that local melting of the cascade region is quite likely, especially when it is considered that these Sigmund values must be underestimates and are probably greatly exceeded in regions of the diffuse cascades such as 100keV Ar. In the work mentioned above, in which the disordered zones were observed by Jenkins et al in Nb_3Sn, the Sigmund energy density of 0.13eV/atom (70keV Au ions) is comparable to the lowest employed in the current study. Since it is unlikely that these zones can be produced by either mechanism (i) or (ii), it must be concluded that this energy density is sufficient to produce disorder in Nb_3Sn. It is possible therefore, that the whole of the cascade region may be melted in the case of a compact cascade such as 50keV Kr, and that those parts of the more diffuse cascades which exceed the "melting energy" may also be melted. Furthermore, the fact that Cu_3Au disorders at ~660K (0.06eV/atom) suggests that disordering in the cascade may proceed without melting, provided these energies are maintained for sufficiently long times.

The production of disordered zones in a binary alloy has been demonstrated by fully dynamic computer simulations of the

cooling phase of cascades in Nb_3Sn carried out by Chudinov et al [1983]. In these local melting was assumed to occur and it was shown that upon recrystallization the atoms adopted a random configuration, thus producing a disordered zone.

The final mechanism which may induce disorder is the production of antisite defects by the migration of vacancies as suggested in (iv) above. As explained in the introduction, thermal equilibrium vacancy jump rates are such that no appreciable vacancy motion should occur during the cascade process. However, the formation of vacancy loops even when computer simulations indicate that at the end of the collision phase the vacancy arrangements are still fairly dilute, is evidence that such migration must occur. In addition, computer simulations by Guinan and Kinney [1981] and Protasov and Chudinov [1982] indicate that vacancy jump rates well in excess of the thermal equilibrium rate may occur ($\sim 5 \times 10^{12}$ jumps s^{-1}) for surprisingly long times ($\sim 10^{-11}$s). This suggests that each vacancy in the region may execute up to 50 jumps during the cascade lifetime. Even at a vacancy concentration of 2 at %, this still suggests that every atom in the region may be expected to move once on average. Given that only 50% of the atoms need move to completely disorder the region, it is quite possible that the observed disorder is produced in this way.

The above discussion on each of the four possible mechanisms indicates that the disordered zones observed at cascade sites are unlikely to have resulted from either the collisional or recombination mechanisms, even in the cases of the lowest observed energy densities. This does not mean of course that

no disorder is introduced by these mechanisms, merely that they are not the dominant ones. With respect to the remaining two, namely that extensive atomic interchange occurs during the spike phase either by local melting (or by some other atomic exchange mechanism), or by interchange induced by migrating vacancies; the trends in zone sizes, the energy densities and computer simulations all indicate that these are the most likely cause of the observed disorder. However, distinguishing between these mechanisms, which both occur during the spike phase, would appear to be an impossible task. Even the disordering which may be introduced by vacancy-interstitial recombination (again, occurring during the relaxation and spike phases) must be inextricably linked with the other spike mechanisms. In view of this, it is proposed to explain the observed trends in disordered zone sizes by a model based on this spike induced disordering, without being specific as to which mechanism dominates.

7.2.2 The Model

In view of the conclusion of the preceding section, that the observed disordering is most likely to have occurred during the spike phase, a model will be proposed in this section which provides a framework, within which the observed trends in disordered zone sizes may be understood. Irrespective of whether the disorder is due to local melting or vacancy migration, it is expected that local energy density, and the time for which that density is maintained must be important factors. If disorder may only be introduced by local melting of the region, it cannot occur unless local energy densities

exceed ~0.11eV/atom (corresponding to the 1250K melting point). However, the fact that Cu_3Au disorders at 660K suggests that densities of ~0.06eV/atom may suffice. On the other hand, if disorder is introduced by the migration of vacancies, neither of these values may have to be achieved as computer simulations by Protasov and Chudinov [1982] indicate that migration continues at temperatures below 500K. This is also supported by the work of Guinan and Kinney [1981] which suggests that vacancy movement is much more significant than predicted by thermal equilibrium calculations.

It is therefore proposed that there exists a critical energy density, E_c , above which the atoms in a local region have sufficient energy to interchange positions and produce disorder. The value of E_c will of course depend on the mechanism (or combination of mechanisms) which is producing the disorder, although it is expected that it should lie in the range 0.05-0.1eV/atom. It seems reasonable that the time for which the atoms retain an energy in excess of E_c must also be important. If the local energy density exceeds E_c for only a short time, disordering must be limited in its extent. For this reason, it is further proposed that there exists a critical time, t_c , for which the atoms in a region must have energies in excess of E_c for disordering to result. Furthermore, the degree to which the local energy density exceeds E_c must also play a part. In regions in which E_c is greatly exceeded, it is expected that disordering will occur even if cooling is rapid. Thus, the critical time required for disordering must be some function of the local energy

density which exists at the start of the cooling phase, θ. i.e. $t_c(\theta)$ must be short for high energy density regions, but longer for low density regions.

From the discussion on cascade dimensions presented in the introduction, it is expected that cascades of high Sigmund energy density (ie heavy ion, low energy) should have a fairly constant energy density and should disorder uniformly throughout their volume, and may even transmit sufficient energy to the surrounding lattice to induce its disorder. On the other hand, it is expected that cascades of nominally low energy density may only disorder in those regions in which the density exceeds E_c. This accounts for the fact that zones produced at the sites of nominally high energy density cascades are of a size similar to that predicted by WSS for the cascade dimensions, whereas those at the sites of nominally low density cascades occupy volumes smaller than WSS predicts.

The trends in zone sizes which must be accounted for by the model are:

(i) Zones produced at room temperature are larger than those produced at low temperature.

(ii) Zones produced by higher energy ions are larger than those produced at lower energy.

(iii) Zones produced by lighter ions are smaller than those produced by heavier ions.

The first of these observations may be explained by

considering the rate of cooling in the two cases. The higher ambient lattice temperature in the room temperature case must be expected to slow the cooling of the cascade region. Given that the collision phase should not be greatly altered by the change in ambient lattice temperatures, and so the average atomic energies within the cascade should initially be similar (which in turn means that $t_c(\theta)$ should be similar in each case), the decreased rate of cooling in the room temperature case will result in more atoms remaining above E_c for longer than t_c i.e. result in a larger disordered zone. This is confirmed in the study by Chudinov et al [1977] referred to above. In this work it was found that provided the initial temperature at which energy is extracted by a conduction mechanism is taken as ~3000K (see previous), surprisingly small changes in ambient lattice temperature (~200-300K) could result in significant changes in the volume melted. Thus, given that atomic energies at room temperature are ~0.03eV/atom and that E_c is around 0.05-0.1eV/atom it appears quite feasible that the difference between room and liquid helium temperatures may be sufficient to account for the observed difference in zone size.

The observation that zones produced by 100keV ions are larger than those at 50keV may again be accounted for by considering the respective cooling rates. It is expected that there will exist subcascade regions within the 100keV cascade which have energy densities similar to those at 50keV. Those in the 100keV case will however, be surrounded by excited regions of lower energy density whereas those in the 50keV case are in

much closer proximity to the ambient lattice. This should result in the 50keV regions cooling at a higher rate, and so fewer atoms remaining above E_c for longer than t_c. In contrast, it is expected that the high density subcascades in the 100keV cases will lose their energies relatively slowly via the low density regions and maintain those regions above E_c for longer than t_c. The outcome of this will be that the disordered zones in the 50keV case will be smaller than those at 100keV.

The final observation, that heavier ions produce larger disordered zones than lighter ions despite generating smaller cascades may be attributed to the greater initial atomic kinetic energies in the dense, heavy ion cascades. In such cases E_c may be exceeded over most of the WSS cascade volume, whereas in the more diffuse light ion cascades it will only be exceeded within the higher density subcascades which are expected to arise (Section 7.1). As these subcascade regions in say, the Ar cascades are unlikely to exceed the dimensions of Kr cascades, it is not surprising that the disordered zones in the latter case are larger. Of course, cooling in the heavy ion cases will be accelerated relative to the more diffuse cascades as a result of both the proximity of the ambient lattice and the higher atomic energies, and this must partially offset the effects of the more rapid disordering. In fact, the observation that the 50keV Kr zones are larger than their 50keV Cu counterparts at room temperature, but not at low temperature may indicate that the increased rate of cooling in the heavy ion case is enhanced sufficiently at low temperature to outweigh the effect of the initial energy

distribution. However, the energy densities given in Table 7.1 suggest that disordering should still occur over most of the WSS volume. This argument is supported by the observation that in the 50keV Kr case (and in the 70keV Au irradiations [Jenkins and English 1982]), the disordered zone sizes exceed the predictions of the WSS theory indicating that the energy density is sufficient not only to disorder within the cascade volume, but also to transmit sufficient energy to the surrounding lattice to precipitate its disorder. This observation is in complete agreement with the findings of Averback [1982] who also observed leakage of energy from the cascade region.

The justification for the model used to explain the results lies not only in the corroboration it has from the various other experimental and simulation studies, but also in its ability to explain, in a self consistent manner, all the observations of disordered zones in this study. It is now proposed to extend the model to explain the defect yield results.

7.3 CASCADE COLLAPSE

As described in Chapter Two, the previously observed variation in defect yields with ion mass has been attributed by both Eyre [1973] and Wilkens [1975] to the increased vacancy concentration at the centre of a cascade created by a heavy ion, producing an enhanced driving force for further vacancy agglomeration. In a study of ion irradiation of α-iron, Jenkins et al [1978] invoked a similar mechanism to explain the fact that self ions produce no collapse, but 80keV

tungsten ions result in a defect yield of 0.2. However, as this idea predicts less collapse at room temperature relative to that observed at low temperature (Section 2.4.1), in direct contradiction to the results of this study, it is clear that other factors must also be important.

The cascade collapse observed at low temperatures in the present study suggests that enhanced vacancy migration, coupled with a systematic drift to the cascade centre must occur at some point in the cascade evolution, and recent fully dynamic computer simulations have proposed physical mechanisms by which this may occur. Guinan and Kinney [1981] simulated cascades from their initiation until well into the spike phase and observed that vacancy motion proceeded at a surprisingly high rate ($\sim 5 \times 10^{12}$ jumps s^{-1}) for as long as the simulation continued (2×10^{-12} s). This was attributed to stimulation from the recombination of vacancy-interstitial pairs which was also observed. In another study, Protasov and Chudinov [1982] simulated a cascade from the start of the spike phase in order that this phase could be followed further toward its conclusion than had previously been attempted. As discussed in Section 7.1, these workers argue that energy loss from the cascade region cannot proceed by thermal conduction mechanisms until the "temperature" has dropped to ~3000K, at which point phonons may remove the energy. By attributing to the atoms in their cascade, velocities corresponding to this temperature, they have, not surprisingly, observed local melting followed by recrystallization. Upon recrystallization, which occurs at ~1000K, random vacancy motion is observed to be extensive. As

the temperature drops to around 500K-800K, this motion ceases to be random and vacancies migrate in a systematic manner towards the centre of the region (i.e. up the "temperature" gradient). In cases in which the energy is rapidly extracted, the vacancy concentration at the centre is observed to double, relative to its initial value, before the vacancies become frozen in. However, if the energy is extracted at a lower rate (corresponding to a cascade lifetime of $\sim 10^{-10}$s) vacancy agglomeration has been observed to proceed until a void forms at the centre of the region after $\sim 2 \times 10^{-11}$s. Due to the computing time constraints it proved impossible to follow the process to its conclusion after $\sim 10^{-10}$s, but by increasing the anharmonic terms in the atomic interaction potential to simulate the increasing thermal pressure of the surrounding lattice on the void, they observed collapse of the void to a Frank dislocation loop. Despite the fact that this work must be treated with caution due to the assumptions made, it has demonstrated a mechanism by which vacancies may migrate to the cascade centre to form a void and possibly even a loop. As such it must be regarded as an important contribution to the understanding of cascade collapse.

This simulation suggests that the formation of a void, and hence collapse probability, should be dependent on two main factors. The first of these is the rate of cooling of the cascade region, with rapidly cooled cascades having insufficient time to allow such vacancy agglomeration as is required for void/loop formation. The second factor is the initial configuration of vacancies existing after the collision phase has occurred, with cascades of high vacancy

concentration forming voids/loops even if they are rapidly cooled. In view of this it is proposed that there exists a critical vacancy concentration, C_v, which must be achieved if cascade collapse is to occur. It is not suggested that this concentration must be achieved by the end of the collision phase, but instead by the end of the spike phase by which time no further vacancy motion is possible. To account for the differences in the cooling rates of cascades, a critical time, t_v, must be introduced into the model. This is the time required for the critical vacancy concentration to be achieved under any given circumstances, and must therefore be a function of initial vacancy concentration, C_o, (i.e. $t_v(C_o)$); such that cascades of high initial vacancy concentration should require less time to form a void or loop and so t_v would be less under such circumstances than if the initial concentration were low. The observations which must be explained by this model are:

(i) Within any single irradiation condition, cascades which produce larger disordered zones are more likely to collapse to loops.

(ii) Cascades produced at room temperature are more likely to collapse than those produced at low temperature.

(iii) Cascades produced by heavier ions are more likely to collapse than those produced by lighter ions.

(iv) Cascades produced by ions at 100keV are equally likely to collapse to loops as those produced by 50keV ions.

It is worth pointing out again at this stage that point (i) is not considered to be due to an imaging artefact caused by the presence of loops (Section 6.3.6). However, even if this were the case, the fact that larger disordered zones are observed after room temperature (as opposed to low temperature) and heavy ion (as opposed to lighter ion) irradiations, cannot simply be dismissed as originating from the same artefact. These must be genuine effects as they are also present in the uncollapsed zone populations.

The observation that cascades associated with larger disordered zones are more likely to collapse to loops is entirely consistent with the model proposed for the origin of the disorder. Section 7.2 indicated that a large disordered zone should result from a cascade in which either cooling has been slow enough to allow extensive disordering to occur, or in which the deposited energy density is sufficiently high that disordering has resulted very quickly. If the first of these is correct, the slow cooling rate should also allow vacancy migration to continue beyond t_v, thus producing extensive agglomeration and collapse. On the other hand, if a high energy density is responsible for the high degree of disordering, it is expected that the high initial vacancy concentration which accompanies a high energy density (Tables 7.1 and 7.2) will result in a reduction in t_v , thus allowing agglomeration to be sufficient for C_v to be achieved and

collapse to occur.

Observation (ii), that room temperature cascades collapse more readily than their low temperature counterparts, is not at all surprising when viewed in terms of the preceding discussion. Room temperature cascades have larger disordered zones associated with them, due to their reduced rate of cooling, and as such fall into the first of the two categories outlined above, with vacancy migration extending beyond t_v, and collapse ensuing.

The possibility of fewer vacancies being generated at low temperature owing to the increased displacement threshold (Section 7.1), must also be considered when examining this result. It is conceivable that this might lead to a reduced vacancy concentration in the cascade, and therefore an increase in t_v. However, the observation that the loop sizes for the 50keV Cu condition are independent of irradiation temperature suggests that the number of vacancies generated in each case is the same. As 35% more vacancies at room temperature would result in a 16% increase in loop diameter, it is considered most unlikely that such a difference would not have been revealed by the sizing procedure employed. It is therefore concluded that the number of vacancies produced in a cascade at room temperature is the same as that generated at low temperature. This conclusion is supported by Laupheimer et al [1981] who observed no change in the diameter of loops created by 30keV self ion irradiation of Cu over the range 6-295K. Since loop diameters remain constant but disordered zone diameters increase with increasing temperature,

this may indicate that the time required for disordering (t_c) exceeds the time required for agglomeration (t_v) such that all vacancies surviving recombination may agglomerate in both cases, but that in the low temperature case insufficient time is available for disordering on the peripheries of the region.

The reason for observation (iii) is also contained in the above discussion as cascades produced by heavier ions are associated with larger disordered zones due to their high energy densities. As described previously, such zones also have high vacancy concentrations and therefore small values of t_v which leads to enhanced collapse.

The fact that changing the ion energy from 50keV to 100keV has no effect on the collapse behaviour may be explained by again considering the variations in density which occur within the higher energy cascades. As collapse occurs in 50keV cascades it is clear that the critical vacancy concentration required for formation of a visible loop C_v, must be attained in such cascades. As pointed out in Section 7.1, subcascade regions will occur in 100keV cascades which have similar energy densities/initial vacancy concentrations to those in the 50keV cascades. It is therefore expected that t_v for such regions should be similar to that in a 50keV cascade, and given that cooling of the subcascade regions in the 100keV case should proceed at a reduced rate relative the 50keV case, collapse must also be expected in such subcascade regions. The larger observed loop diameters in the 100keV cascades (Section 6.3.5) imply that additional vacancies from the more diffuse regions also join the loop despite the fact that they

are not required to precipitate the initial collapse. The lower cascade efficiencies in the 100keV case may indicate either that not all vacancies reach the loop in this case or that more recombination results as a consequence of the increased distances they must migrate over.

The observation that a reduction in defect yield occurs below 50keV in Cu_3Au [Jenkins and Wilkens 1976] as has been observed in other materials [Chapter Two] is consistent with the proposed model if it is assumed that cascades of energy below 50keV are so dense that they cool before t_v has elapsed, i.e. that the cooling rate dominates over the vacancy concentration at such small cascade sizes. Alternatively, this may be due to clusters resulting from such low energy bombardment being too small for resolution by the diffraction contrast technique.

7.4 SUMMARY

The superlattice technique has enabled the independent investigation of both cascade collapse and cascade disordering under a variety of irradiation conditions. The experimental results obtained from these investigations are consistent with extensive atomic interchange during the so-called spike phase producing disorder, and collapse resulting from the systematic vacancy migration which occurs during the same phase of the cascade evolution. A model based upon this spike motion has been proposed which accounts for the observations that:

Cascade collapse occurs at low temperatures, and that

subsequent increases in the ambient lattice temperature induce no further collapse;

Cascades produced at higher temperatures will result in larger disordered zones and a greater collapse probability;

Cascades produced by heavier ions will result in larger disordered zones and a greater collapse probability;

Cascades produced by more energetic ions will result in larger disordered zones but not a greater collapse probability;

In any irradiation condition, the cascades associated with larger disordered zones are more likely to collapse;

The major factors which determine the extent of this motion and hence the degree of disordering and collapse probability have been identified as the rate of cooling of the cascade region and the initial elastically deposited energy density and vacancy concentration.

An interesting experiment would involve the investigation of both disordering and collapse behaviour at elevated temperatures to monitor whether or not the observed trends continued. In particular, irradiating above the vacancy migration temperature (~420K) and just below the order-disorder transition may yield further insight into the relative importance of the various mechanisms proposed in this work. Additionally, extending the range of energy densities beyond that studied in the present study would provide an interesting test of the limits of applicability of the model.

APPENDIX 7.1

Number of vacancies in loop = "Volume" of loop x Atomic Density

Volume of loop = Area x Depth

Area = $\pi d^2/4$

Depth = {111} plane spacing

= 2.3Å

Atomic Density = 7.57×10^{-2} Å^{-3}

From Table 6.9:

50keV Cu loop image width 51Å

100keV Kr loop image width 64Å

Likely range of loop diameters: [Rühle 1969]

50keV Cu: 51/1.2 - 51Å = 42 - 51Å

100keV Kr: 64/1.2 - 64Å = 53 - 64Å

Thus, likely numbers of vacancies are:

50keV Cu:	240	-	360	: 300 is mean
100keV Kr:	380	-	560	: 470 is mean

Given that the expected (NRT) numbers of vacancies in each case are 800 and 1640 (Table 7.2), the cascade efficiencies are:

50keV Cu: 0.37

100keV Kr: 0.29

REFERENCES

ANDERSEN H H; BAY H L
Rad. Effects 19, No 3, 139-146, (1973)

Jour. Appl. Phys. 45, 953-954, (1974)

Jour. Appl. Phys. 46, 2416-2422, (1975)

AVERBACK R S
Jour. Nucl Mat. 108 & 109, 33-45, (1982)

AVERBACK R S; BENEDEK R; MERKLE K L
Jour. Nucl. Mat. 69 & 70, 786-789, (1978)

BEELER J R
Advances in Mater. Research 4, 295-476, (1970)

BEELER J R; BEELER M F
Fund. Aspects of Rad. Dam. in Metals
Proc. Int. Conf. Gatlinburg Tenn. USA, USERDA CONF 751006-P1
28-34, (1975)

BIRTCHER R C; BLEWITT T H; KIRK M A; SCOTT T L; BROWN B S; GREENWOOD L R
Jour. Nucl. Mat. 108 & 109, 3-9, (1982)

BRANDON D G; BOWDEN P
Phil. Mag. 6, 707-710, (1961)

BREBEC G
Mass Transport in Solids
Proc. NATA Adv. Study Inst. held at Lannion, France 1981.
(Bénière F and Catlow C R A Eds.)
Plenum Press N.Y., 227-250 (1983)

BRINKMAN J A
Jour. Appl. Phys. 25, No 8, 961-970, (1954)

BRODIE I; MURAY J J
The Physics of Microfabrication
Plenum Press NY 1982

CHUDINOV V G; GOGOLIN V P; GOSHCHITSKII B N; PROTASOV V I
Phys. Stat. Sol.(a) 67, 61-67, (1981)

Phys. Stat. Sol.(a) 80, 349-352, (1983)

CHUDINOV V G; PROTASOV V I; TELICHKO M T
Fiz Metal Metalloved 43, No.4, 692-701, (1977)
(English translation: Phys. Metals. Metallog.
43, No.4, 12-20, (1977))

CURRENT M I; WEI C-Y; SEIDMAN D N
Phil. Mag. A 47, No 3, 407-434, (1983)

ENGLISH C A; EYRE B L; BARTLETT A F; WADLEY H N G
Phil. Mag. A 35, No 3, 533-548, (1977)

ERGINSOY C; VINEYARD G H; ENGLER A
Phys. Rev. 133, No 2A, 595-606, (1964)

ERGINSOY C; VINEYARD G H; SHIMUZU A
Phys. Rev. 139, No 1A, 118-125, (1965)

EYRE B L.
Jour. Phys. F. 3, No 2, 422-470, (1973)

EYRE B L; ENGLISH C A
Point Defects and Defect Inter. in Metals.
Proc. of Yamada Conf. held at Kyoto 1981, (Takamura J-I;
Doyama M; Kiritani M. Eds.), 799-806, (1982)

FISHER R M; MARCINKOWSKI M J
Phil. Mag. 6, 1385-1405, (1961)

FISHER S B
Rad. Effects 5, No 3 & 4, 239-243, (1970)

GALE B; HALE K F
Brit. Jour. Appl. Phys. 12, 115-117, (1961)

GIBSON J B; GOLAND A B; MILGRAM M; VINEYARD G H
Phys. Rev. 120, 1229-1253, (1960)

GILBERT J; HERMAN H; DAMASK A C.
Rad. Effects 20, No 1 & 2, 37-42, (1973)

GMELINS HANDBUCH DER ANORGANISCHEN CHEMIE
Verlag Chemie, GmbH, Weiheim Bergstrasse, Germany, 1954, 820-930

GUINAN M W; KINNEY J H
Jour. Nucl. Mat. 104, 1319-1323, (1981)

HAGA K; BAILEY A C; KING W E; MERKLE K L; MESHII M
Proc. Seventh Int. Conf. on HVEM held at Berkeley, USA, 1983.
(Fisher R M; Gronsky R; Westmacott K H Eds) CONF-830819, (1983)

HAMEED M Z; SMALLMAN R E; LORETTO M H
Phil. Mag. A46, 5, 717-721, (1982)

HAUSSERMAN VON F
Phil. Mag. 25, 537-560, (1972)

HEINISCH H L
Hanford Laboratory Report HEDL-TME 83-17, UC-20, 20c, (1983)

HERTEL B
Phil. Mag. A, 40, No 3, 313-330, (1979)

HERTEL B; KAMMHOLZ K; DIEHL J
Rad. Effects 48, No 1-4, 45-49, (1980)

HIRSCH P; HOWIE A; NICHOLSON R B; PASHLEY D W; WHELAN M J
Electron Microscopy of Thin Crystals
Butterworth, (1965)

HOWE L M; McGURN J F; GILBERT R W
Acta. Met. 14, 801-820, (1966)

HOWE L M; RAINVILLE M H
Phil. Mag. A 39, No 2, 195-212, (1979)

JAGER W
Jour. Microsc. Spectrosc. Electron. 6, 437-462, (1981)

JAGER W; RUHLE M; WILKENS M
Phys. Stat. Sol.(a) 31, 525-533, (1975)

JENKINS M L; ENGLISH C A
Jour. Nucl. Mat. 108 & 109, 46-61, (1982)

JENKINS M L; ENGLISH C A; EYRE B L
Phil. Mag. A, 38, 1, 97-114, (1978)

JENKINS M L; KATERBAU K-H; WILKENS M
Phil. Mag. A, 34, No.6, 1141-1153, (1976)

JENKINS M L; ROLLER G; KATERBAU K-H; WILKENS M
Jour. Nucl. Mat. 108 & 109, 603-613, (1982)

JENKINS M L; WILKENS M
Phil. Mag. A, 34, No.6, 1155-1167, (1976)

KAPINOS V G; KEVORKYAN YU R
Rad. Effects. 79, 9-20, (1983)

KATERBAU K-H
Phys. Stat. Sol. (a), 38, 463-476, (1976)

Phil. Mag. A,43, No 2, 409-426, (1981)

KINCHIN G H; PEASE R S
Rep. Prog. Phys. 18, 1-51, (1955)

KING W E
Phd. Thesis, Northwestern Univ., Evanston, Illinois, (1980)
(Unpublished).

KING W E; BENEDEK R
Point Defects and Defect Interactions in Metals
Proc. of Yamada Conf. held at Kyoto 1981. (Takamura J-I;
Doyama M; Kiritani M; Eds.), 807-810, (1982)

Jour. Nucl. Mat. 117, 26-35, (1983)

LAUPHEIMER A; FRANK W; RUHLE M; SEEGER A; WILKENS M
Rad. Effects Lett. 67, No 3, 95-99, (1981)

LAUPHEIMER A; WILKINS M
Phys. Stat. Sol. (a) 55, 97-507, (1979)

LINDHARD J; NIELSON V; SCHARFF M; THOMSEN P V
Kgl. Danske Videnskab Selskab, Matfys. Medd, 33, No 10, (1963)

MARWICK A D
UKAEA Harwell Report AERE-R7745

MERKLE K L
Phys. Stat. Sol. 18, 173, (1966)

Rad. Dam. in Reactor Mat. 1, Proc. Symp. held at Vienna,
IAEA-SM-120/B-2, 159-170, (1969)

MERKLE K L; AVERBACK R S
Fund. Aspects of Rad. Dam. in Metals
Proc. Int. Conf. Gatlinburg Tenn. USA; USERDA CONF 751006-P1
127-133, (1975)

MERKLE K L; JAGER W
Phil. Mag. A. 44, 741-762, (1981)

MERKLE K L; PRONKO P P
Jour. Nucl. Mat. 53, 231, (1974)

MERKLE K L; SINGER L R; WROBEL J R
Appl. Phys. Lett. 17, No 1, 6-7, (1970)

MUKAI T; MITCHELL T E
Phil. Mag. A45, No.5, 741-751, (1982)

NELSON R S
Phil. Mag. 10, 723-726, (1964)

NORGETT M J; ROBINSON M T; TORRENS I M
UKAEA Harwell Report TP494 (1972)

PANDE C S
Phys. Stat. Sol. (a) 52, 687-696, (1979)

POTTER D I; HERNANDEZ O G
Acta. Met. 29, 187-196, (1981)

POWELL C F; OXLEY J H; BLOCHER J M
Vapour Deposition
J Wiley (1966)

PRAMANIK D; SEIDMAN D N
Jour. Appl. Phys. 54, No 11, 6352-6367, (1983)

PROTASOV V I; CHUDINOV V G
Rad. Effects 66, 1-7, (1982)

ROBINSON M T; TORRENS I M
Phys. Rev. B 9, No 12, 5008-5024, (1974)

ROBINSON T M; JENKINS M L
Phil. Mag. A. 43, No 4, 999-1015, (1981)

RUHLE M.
Rad. Dam. in Reactor Mat. 1, Proc. Symp. held at Vienna,
IAEA-SM-120/B-2, 113-157, (1969)

SEEGER A
Proc. 2nd Int. Conf. Peaceful Uses of Atomic Energy held at Geneva
6, 250-273, (1958)

SEIDMAN D N
Jour. Phys. F. 3, No 2, 393-421, (1973)

SEILER G; WILKENS M; KATERBAU K-H
Proc. 8th Int. Cong. Electron Micr. held at Canberra
1, 618, (1974)

SEITZ F
Phys. Today 5, No.6, 6-9, (1952)

SEITZ F; KOEHLER J S
Prog. in Solid State Phys. 2, 305-448, (1956)

SIEGEL S
Phys. Rev. 75, 1823-1824, (1949)

SIGMUND P
Appl. Phys. Lett. 14, No 3, 114-117, (1969a)

Phys. Rev. 184, 383-416, (1969b)

Appl. Phys. Lett. 25, No 3, 169-171, (1974)

Appl. Phys. Lett. 27, No 1, 52, (1975)

SILSBEE R H
Jour. Appl. Phys. 28, 1246-1250, (1957)

STATHOPOLOUS A Y
Phil. Mag. A. 44, No 2, 285-308, (1981)

STUART R N; GUINAN M W; BORG R J
Rad. Effects 30, No 3, 129-133, (1976)

TAKAMURA S; OKUDA S
Rad. Effects 17, No 3 & 4, 151-158, (1973)

TAYLOR A; WALLACE J R; RYUN E A;PHILIPPIDES A;WROBEL J R;
Nucl. Inst. Methods 189, 211-217, (1981).

TENENBAUM A
Phil. Mag. A 37, 6, 731-748, (1978)

THOMPSON D A
Rad. Effects, 56, Nos 3 & 4, 105-150, (1981)

THOMPSON M W
Defects and Radiation Damage in Metals
Cambridge University Press (1969)

TORRENS I M; ROBINSON M T
Rad. Ind. Voids in Metals (CORBETT J W; IANNIELLO L C Eds.)
USAEC Report CONF 710601, 739, (1972)

URBAN K
Phys. Stat. Sol.(a) 56, 157-168, (1979)

VINEYARD G H
Proc. Int. Conf. on Cryst. Latt. Def., 1962
Jour. Phys. Soc. Jpn. 18 Suppl. III, 144-150, (1963)

WALKER R S; THOMPSON D A
Rad. Effects 37, No 1 & 2, 113-120, (1978)

WEI C-Y; CURRENT M I; SEIDMAN D N
Phil. Mag. A. 44, No 2, 459-491, (1981)

WEI C-Y; SEIDMAN D N
Phil. Mag. A. 43, No 6, 1419-1439, (1981)

WILKENS M
Fund. Aspects of Rad. Dam. in Metals
Proc. Int. Conf. Gatlinburg Tenn. USA, USERDA CONF 751006-P1
98-112, (1975)

WINTERBON K B; SIGMUND P; SANDERS J B
Kgl. Danske Videnskab Selskab, Matematisk-Fysiske Meddelelser.
37, 14, 40-113, (1970)

YAMAGUCHI S; WATANABE D; OGAWA S.
Jour. Phys. Soc. Japan 17, 6, 1030, (1961)

YOSHIDA N; URBAN K
Phys. Lett. 75A, No.3, 231-233, (1980)

APPENDIX A

Examples of disordered zones created under all twelve irradiation conditions. All micrographs were recorded on the JEM100B microscope except for the 50keV Ar LTI condition shown in Fig. A1, upon which no analysis was performed at Oxford. For this reason, an HVEM room temperature image is presented in this case.

Fig A.1 50keV Ar LTI

Fig A.2 50keV Cu LTI

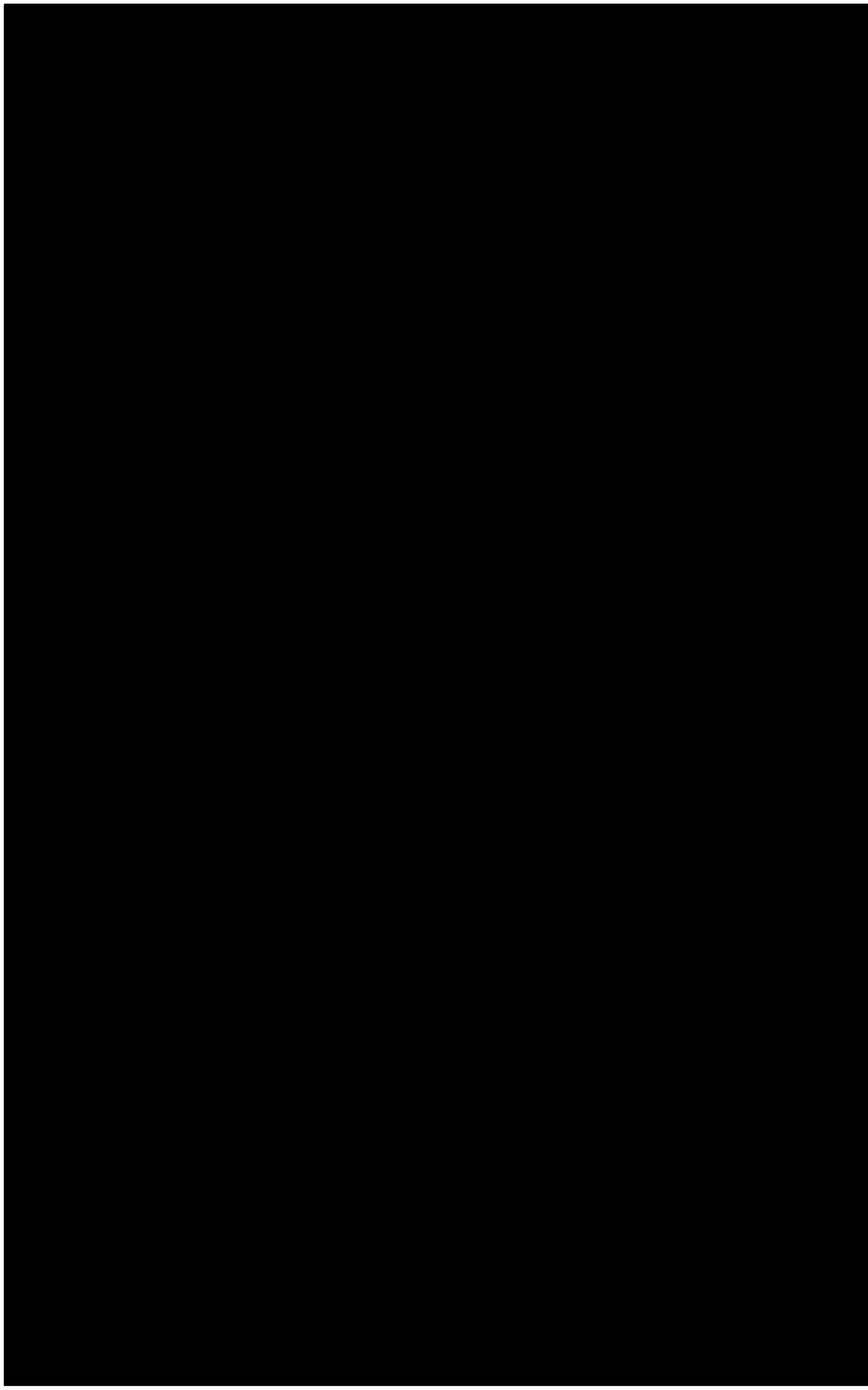

A.E.R.E. HARWELL

PHOTOGRAPHIC GROUP

HR 1515

NOT FOR PUBLICATION

Fig A.3 50 keV Kr LTI

Fig A.4 100keV Ar LTI

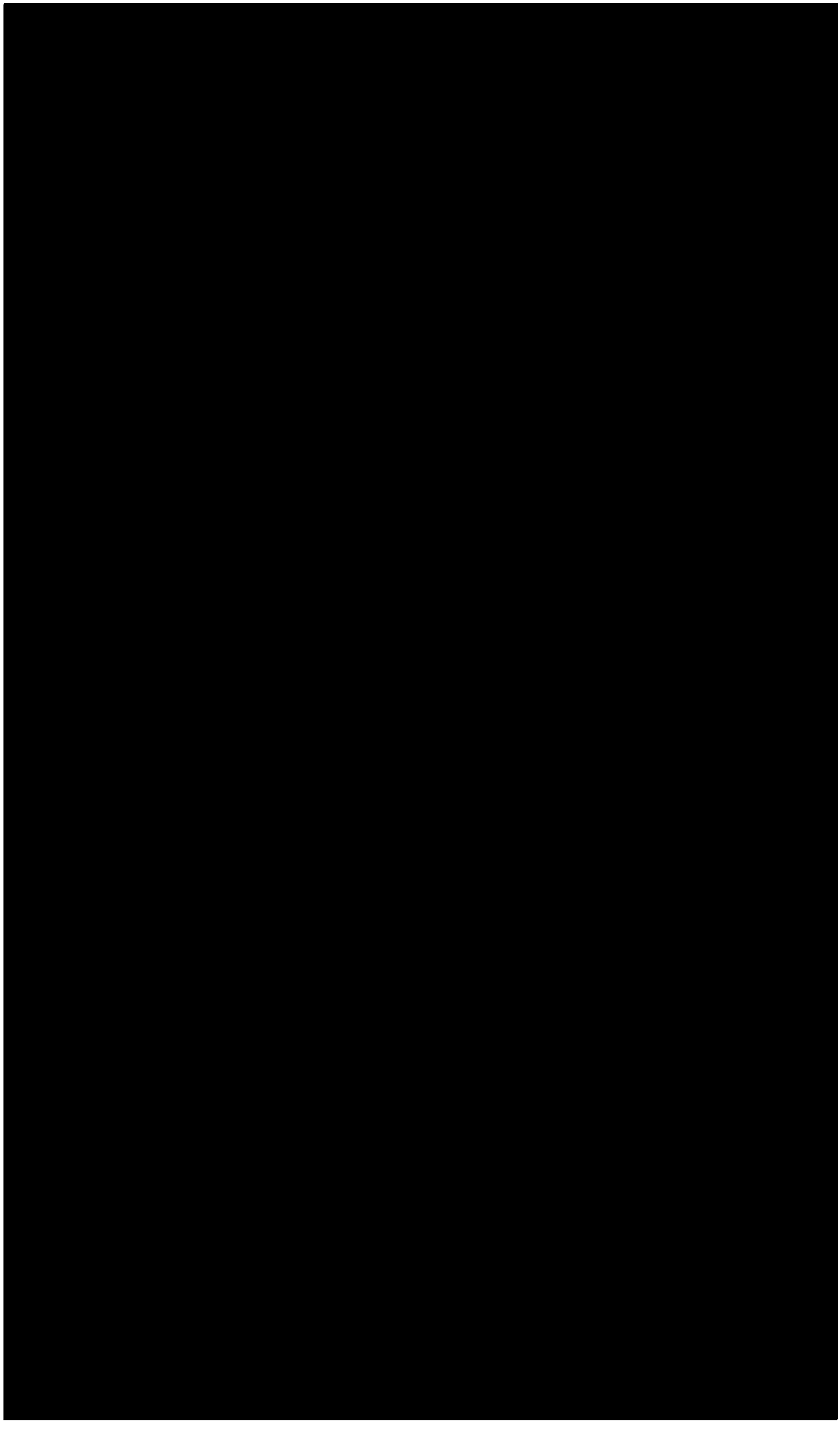

A.E.R.E. HARWELL

PHOTOGRAPHIC GROUP

HR 1521

NOT FOR PUBLICATION

Fig A.5 100keV Cu LTI

Fig A.6 100keV Kr LTI

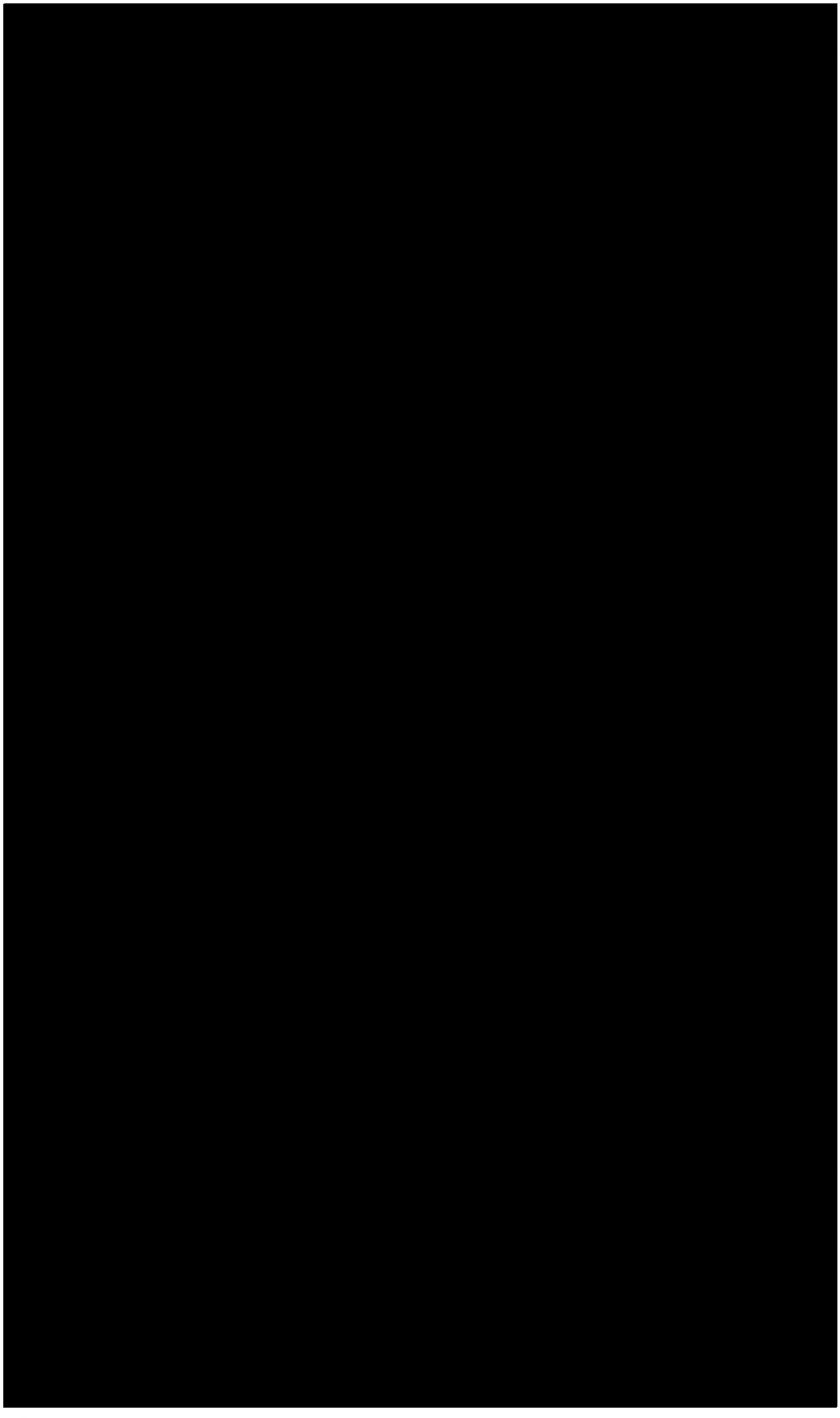

A.E.R.E. HARWELL

PHOTOGRAPHIC GROUP

HR 1520

NOT FOR PUBLICATION

Fig A.7 50keV Ar RTI

Fig A.8 50keV Cu RTI

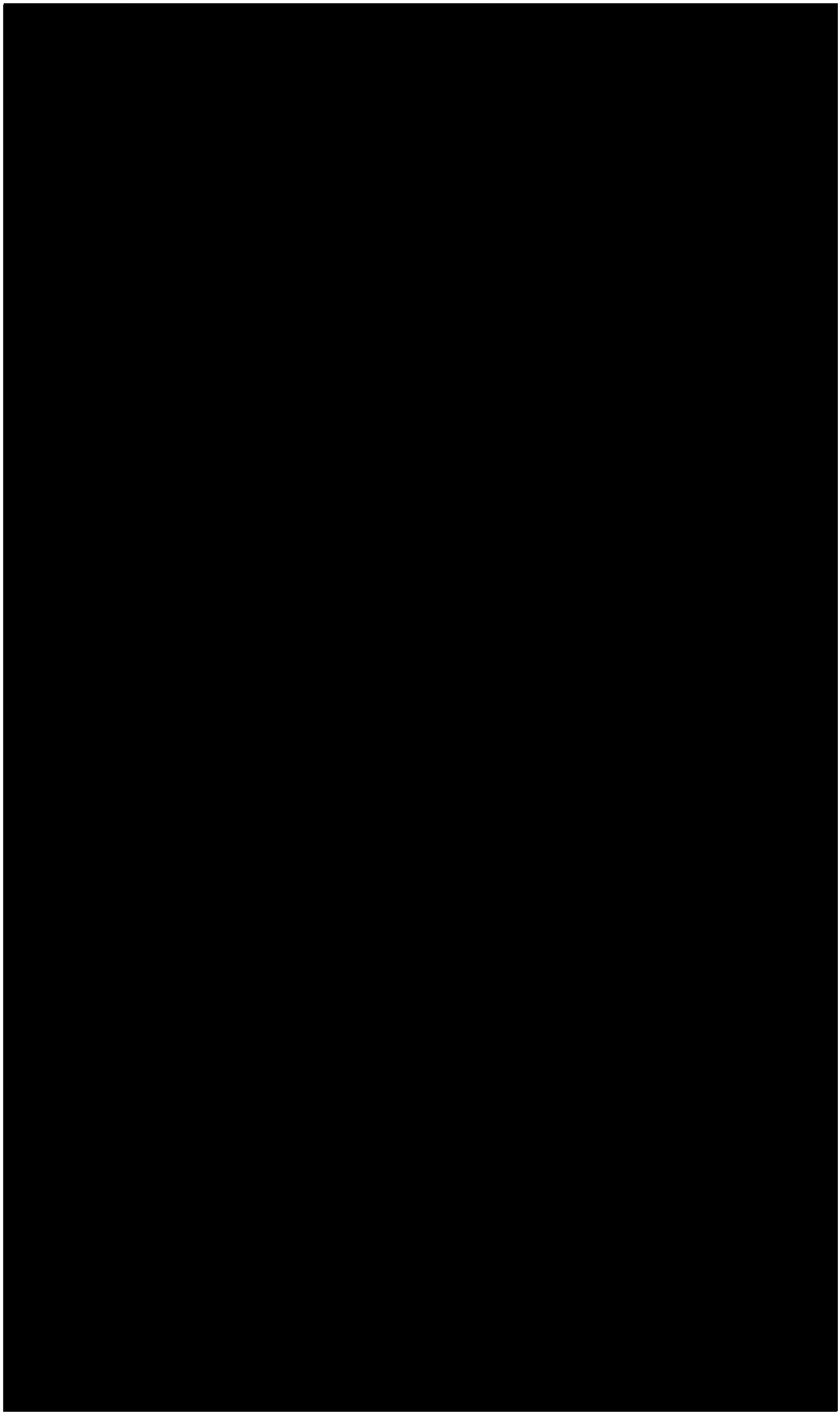

A.E.R.E. HARWELL

PHOTOGRAPHIC GROUP

HR 1523

NOT FOR PUBLICATION

Fig A.9 50keV Kr RTI

Fig A.10 100keV Ar RTI

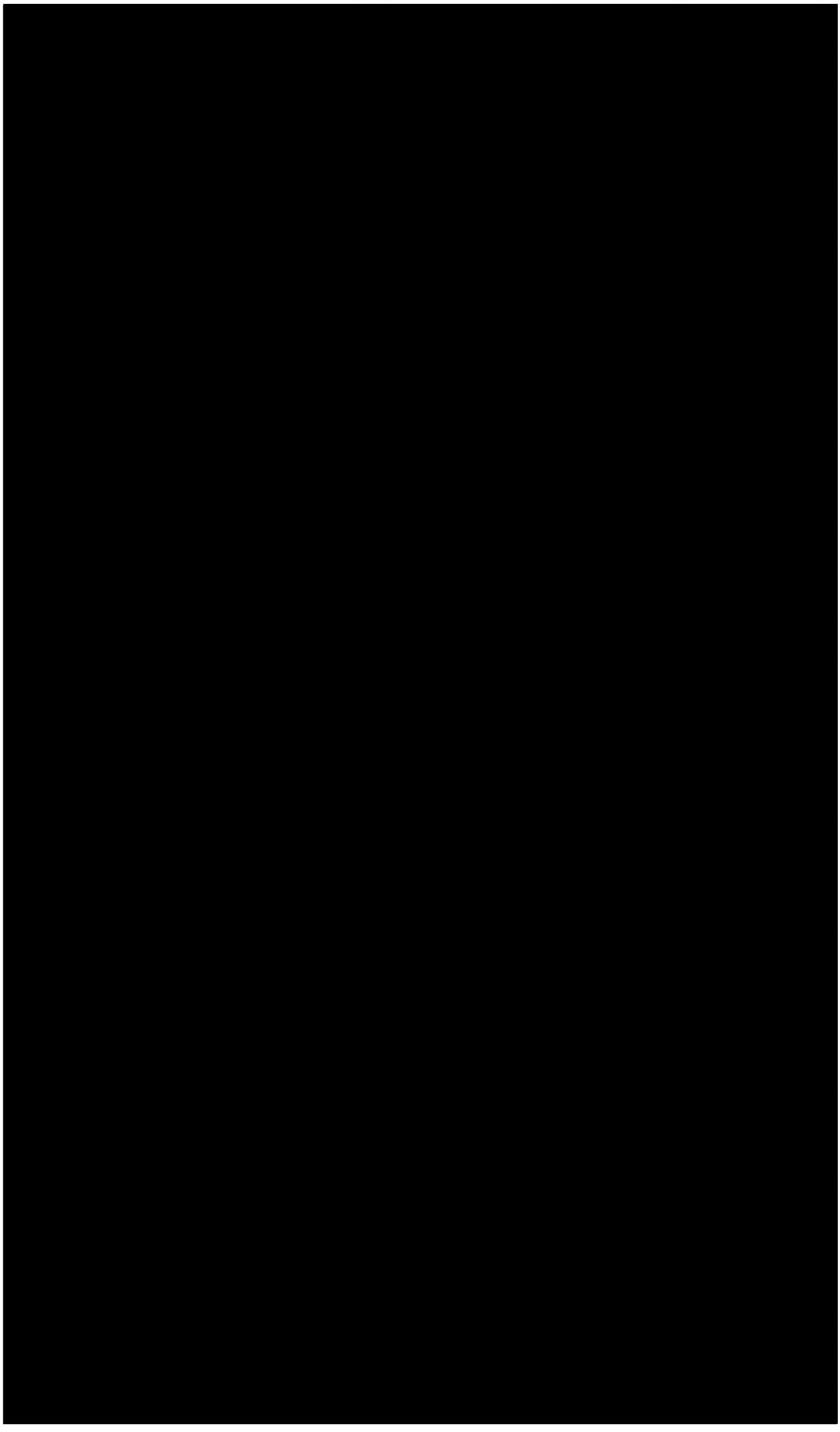

A.E.R.E. HARWELL
PHOTOGRAPHIC GROUP

HR 1522

NOT FOR PUBLICATION

Fig A.11 100keV Cu RTI

Fig A.12 100keV Kr RTI

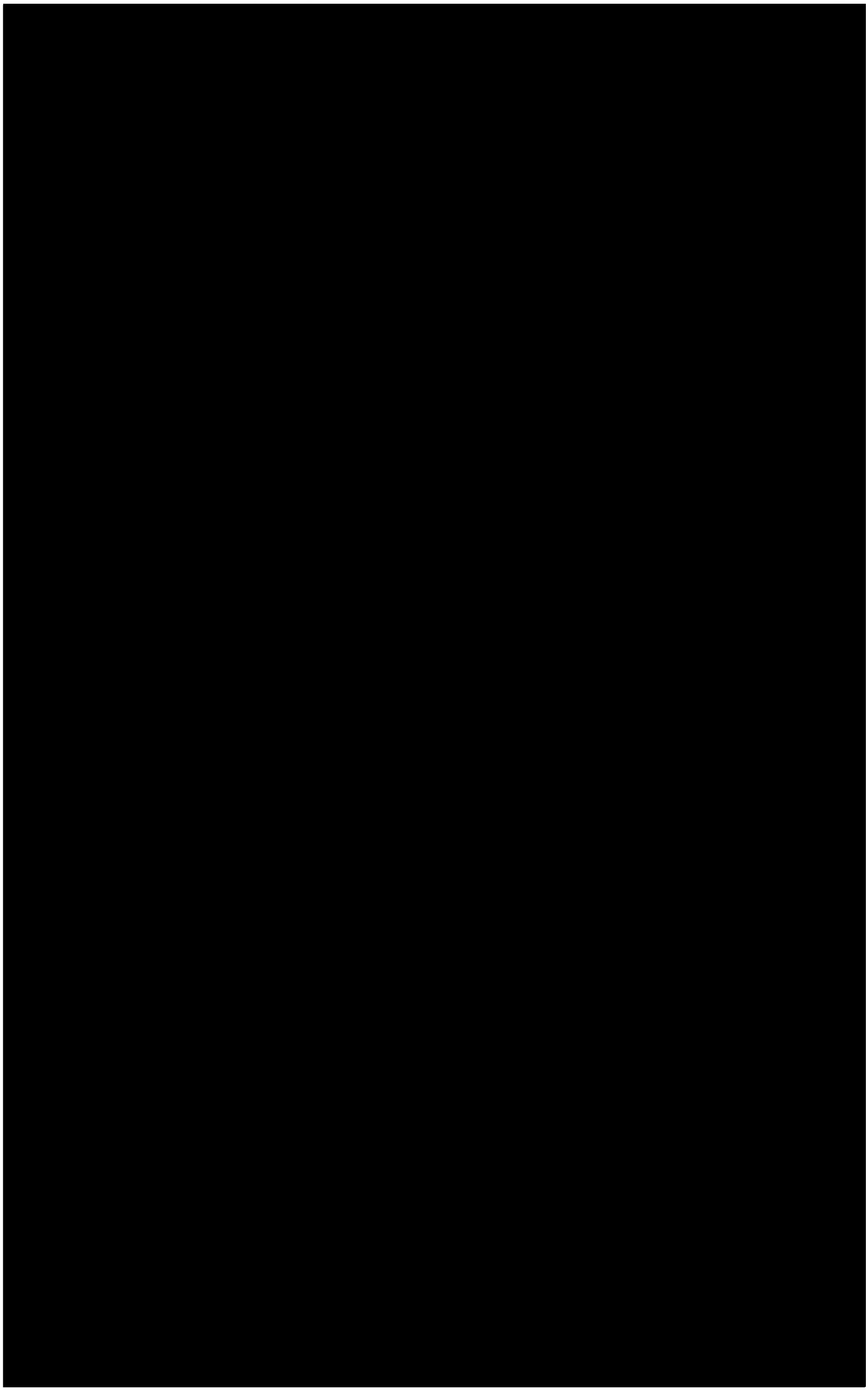

A.E.R.E. HARWELL

PHOTOGRAPHIC GROUP

HR 1525

NOT FOR PUBLICATION

APPENDIX B

Listings of the programmes DIGITIZE, AREA and DISTRIBS which were written for the HP86 microcomputer. These facilitate the data acquisition and manipulation required to obtain the results on zone and loop sizes presented in Chapter Six.

```
10  ! ********************************THIS IS DIGITIZE*****************************
20  !
30  !            This program controls the aquisition of coords by the digitizer
40  ! transferring them to the computer memoryas they are monitored. once all
50  ! coords have been stored they are transferred to disc. Due to the limita-
60  ! tions of available disc space, the maximum number of zones which may be
70  ! digitized is 110.
80  !   Each zone is digitized 3 times. The coords of each attempt are stored i
90  ! arrays DIGX,DIGY. On completion of each attempt,the coords are transferre
100 ! to MAINX,MAINY. IMAX and IMSUM are required to facilitate transfer.After
110 ! all N zones have been digitized 3 times,MAINX/Y are stored on disc.The
120 ! current attempt number is J.It runs from FJ to LJ.(e.g If first zone is
130 ! number 10 and last is 100,FJ=31 and LJ=300). IMAX(J) is the number of
140 ! coords required to digitize attempt J.IMSUM(J) is the sum of the first J
150 ! elements of IMAX(J).
160 !
170 !                                                  Dimensioning  ix arrays and string
180 OPTION BASE 1
190 SHORT DIGX(300),DIGY(300),IMAX(330),IMSUM(330)
200 SHORT MAINX(16075),MAINY(16075),ZERO(330)
210 DIM INFO$(6)[20]
220 !                                          Setting all elements of array ZERO to zer
230 MAT ZERO=ZER
240 BEEP 50,500
250 !                                 Subroutines ZEROA/B/C clear working arrays to zer
260 GOSUB ZEROA
270 GOSUB ZEROB
280 BEEP 50,500
290 GOSUB ZEROC
300 BEEP 50,250
310 !                           Requests input of information on irradition condition
320 !                           and print magnification etc and stores it in INFO$
330 DISP "WHAT IS IRRADIATION CONDITION"
340 INPUT INFO$(1)
350 DISP "WHAT IS PRINT NUMBER"
360 INPUT INFO$(2)
370 DISP "WHAT IS PRINT MAGNIFICATION"
380 INPUT INFO$(3)
390 !                           Note that maximum number of zones which may be digitize
400 !                           is 110 (If more are required,disc must be changed)
410 DISP "NUMBER OF FIRST ZONE"
420 INPUT INFO$(4)
430 DISP "NUMBER OF LAST ZONE"
440 INPUT INFO$(5)
450 DISP "DIGITIZING CLOCKWISE(=C) OR ANTICLOCKWISE(=A)"
460 INPUT INFO$(6)
470 !                                 Requests origin and x-axis to be input from digitize
480 DISP "INPUT CO-ORDINATE ORIGIN AND POINT ON X-AXIS"
490 OUTPUT 906 ;"SG"
500 OUTPUT 906 ;"AA"
510 S=SPOLL (906) @ IF BIT (S,4)=1 THEN 510
520 !                                                  N is number of zones to be digitiz
530 N=VAL (INFO$(5))-VAL (INFO$(4))+1
540 DISP "ZONES";VAL (INFO$(4));"TO";VAL (INFO$(5));"FOR ANALYSIS, :N:"CLOSE"
550 !                           FJ and LJ are first and last attempt numbers respectiv
560 !                           recall that each zone requires 3 attempts
570 FJ=3*(VAL (INFO$(4))-1)+1
580 LJ=3*VAL (INFO$(5))
590 P=0
600 !                                 This loop accepts digitized coords from the digitiz
610 !                                 and stores them in DIGX/DIGY
620 FOR J=FJ TO LJ
630 !                                                        K is current zone numb
640 K=(J+2.9) DIV 3
650 !                                                  P is number of attempt at zone
660 P=P+1
670 !                                                        P may not e used
680 IF P<3 THEN P=1
690 !                                 If P=3 then this is last attempt at zone
700 !                                 Set P=3 to trap errors in digitizing
```

```
710 NEWJ=J-FJ+1
720 BEEP
730 !              Visual reminder of zone and attempt currently being digitized
740 DISP "ZONE";K;"ATTEMPT";P
750 !                                                  Coord digitized every 100m.
760 OUTPUT 906 ;"CN 100"
770 !                                                        I is coord number
780 I=0
790 I=I+1
800 OUTPUT 906 ;"SKO"
810 S=SPOLL (906)
820 IF BIT (S,2)=0 THEN GOTO 810
830 OUTPUT 906 ;"OD"
840 !                                          Digitized coord stored in DIGX,DIGY
850 !                                          (TIM and TOM are irrelevant)
860 ENTER 906 ; DIGX(I),DIGY(I),TIM,TOM
870 !                                  Ensures that more than 10 points are recorded
880 !                                  before closure test is executed
890 IF I<10 THEN 790
900 !                  If any special function key is pressed during attempt,this
910 !                  section aborts attempt by invoking subroutine RESTART
920 S=SPOLL (906)
930 IF BIT (S,7)=0 THEN 1050
940 OUTPUT 906 ;"OK"
950 ENTER 906 ; BAD
960 GOSUB RESTART
970 !                                Audible warning that RESTART has been executed
980 BEEP 7,1000
990 BEEP 7,1000
1000 GOTO 740
1010 !               This section tests if cursor has returned to starting point
1020 !               (ie Closure test). Zone is considered to be digitized when
1030 !               DIGX/DIGY are both whithin 15 digitizer units (375 microns)
1040 !               of the starting point
1050 IF ABS (DIGX(I)-DIGX(1))>15 THEN 790
1060 IF ABS (DIGY(I)-DIGY(1))>15 THEN 790
1070 !                IMAX(NEWJ) is number of coords required to digitize attempt
1080 IMAX(NEWJ)=I
1090 IMSUM(NEWJ)=SUM (IMAX)
1100 DISP IMAX(NEWJ);"READINGS TAKEN"
1110 !                                    TRANS transfers coords from DIGX/Y to MAINX/

1120 GOSUB TRANS
1130 IF P<3 THEN 1240
1140 !                This section determines if sufficient space remains on dis

1150 !                for another zone to be digitized. If there is insufficient
1160 !                space,data is automatically transferred to disc.
1170 RE=16075-IMSUM(NEWJ)
1180 IF RE>700 AND NEWJ<330 THEN 1240
1190 DISP "INSUFFICIENT SPACE ON DISC,TRANSFERRING DATA TO DISC"
1200 DISP "LAST ZONE DIGITIZED WAS";K
1210 INFO$(5)=VAL$ (K)
1220 !                                                Subroutine DISC transfers data to di
1230 GOSUB DISC
1240 GOSUB ZEROA
1250 IF LJ-J>0 THEN GOTO 1270
1260 GOSUB DISC
1270 NEXT J
1280 END
1290 !                          ZEROA/B/C are used to set arrays to zero as requi
1300 ZEROA:
1310 MAT DIGX=ZER
1320 MAT DIGY=ZER
1330 RETURN
1340 ZEROB:
1350 MAT MAINX=ZER
1360 MAT MAINY=ZER
1370 RETURN
1380 ZEROC:
```

```
1390 MAT IMAX=ZER
1400 MAT IMSUM=ZER
1410 INFO$=""
1420 RETURN
1430 !           TRANS transfers coords from DIGX/Y into appropriate locations
1440 !           in MAINX/Y. Attempts are stored sequentially in MAINX/Y using
1450 !           IMAX and IMSUM to determine which locations should be used
1460 !           for each attempt.
1470 TRANS:
1480 IF NEWJ>1 THEN GOTO 1520
1490 MAT MAINX(1:IMAX(NEWJ))=DIGX(1:IMAX(NEWJ))
1500 MAT MAINY(1:IMAX(NEWJ))=DIGY(1:IMAX(NEWJ))
1510 GOTO 1540
1520 MAT MAINX(1+IMSUM(NEWJ-1):IMSUM(NEWJ))=DIGX(1:IMAX(NEWJ))
1530 MAT MAINY(1+IMSUM(NEWJ-1):IMSUM(NEWJ))=DIGY(1:IMAX(NEWJ))
1540 RETURN
1550 !                                DISC stores coords (and other data required fo
1560 !                                retrieval) on disc in drive 1
1570 DISC:
1580 ASSIGN# 1 TO  "LENGTHS:D701"
1590 PRINT# 1 ; IMAX()
1600 ASSIGN# 1 TO  *
1610 ASSIGN# 2 TO  "XDATA:D701"
1620 PRINT# 2 ; MAINX()
1630 ASSIGN# 2 TO  *
1640 ASSIGN# 3 TO  "YDATA:D701"
1650 PRINT# 3 ; MAINY()
1660 ASSIGN# 3 TO  *
1670 ASSIGN# 4 TO  "SUMS:D701"
1680 PRINT# 4 ; IMSUM()
1690 ASSIGN# 4 TO  *
1700 ASSIGN# 5 TO  "INFO:D701"
1710 PRINT# 5 ; INFO$()
1720 ASSIGN# 5 TO  *
1730 !           Clears arrays for next zones.(New disc must be loaded).
1740 GOSUB ZEROB
1750 GOSUB ZEROC
1760 RETURN
1770 !      Subroutine RESTART aborts current attempt and allows user to restar
1780 !      digitizing at any prior zone.All arrays are reset accordingly.
1790 RESTART:
1800 DISP "AT WHICH ZONE SHOULD DIGITIZING RESTART"
1810 INPUT K
1820 J=(K-1)*3+1
1830 NEWJ=J-FJ+1
1840 P=1
1850 MAT IMAX(NEWJ:330)=ZERO(NEWJ:330)
1860 MAT IMSUM(NEWJ:330)=ZERO(NEWJ:330)
1870 GOSUB ZEROA
1880 RETURN
```

```
10  ! ********************************* THIS IS AREA *******************************
20  !
30  !     This program retrieves the coords stored on disc by DIGITIZE.They are
40  ! again stored in arrays MAINX,MAINY,with coords from each attempt being
50  ! transferred in turn to DIGX/DIGY for analysis.The POSITION,MAX DIAMETER,
60  ! MEAN DIAMETER,ELONGATION RATIO,AREA and SHAPE FACTOR of each attempt
70  ! is calculated,with the average of the 3 attempts for all 5 parameters
80  ! being obtained for each zone. These averages are then stored on disc.
90  !
100 !                                                  Dimensioning all arrays and strings
110 OPTION BASE 1
120 SHORT MAINX(16075),MAINY(16075),IMAX(330),IMSUM(330),DIGX(300),DIGY(300)
130 DIM AREAS(330),DIAM(300),RADIUS(300),POSX(330),POSY(330),ZONEINFO$(6)
140 DIM MAXDIAM(330),MEANDIAM(330),STANDEV(330),ELONG(330)
150 SHORT XZONEPOS(110),YZONEPOS(110),ZONEAREA(110),ZONEMAXDI(110)
160 SHORT ZONEMEANDI(110),ELONGATION(110),STDEV(110)
170 SHORT MASTER(110,8),COLLAPSE(110)
180 DIM COND$(2)[20],INFO$(6)[20]
190 !                                 ALLCLEAR sets all elements of all arrays to zero
200 GOSUB ALLCLEAR
210 BEEP
220 !                                   This section retrieves all coord data from disc
230 ASSIGN# 1 TO  "LENGTHS:D701"
240 READ# 1 ; IMAX()
250 ASSIGN# 1 TO  *
260 ASSIGN# 2 TO  "SUMS:D701"
270 READ# 2 ; IMSUM()
280 ASSIGN# 2 TO  *
290 ASSIGN# 3 TO  "XDATA:D701"
300 READ# 3 ; MAINX()
310 ASSIGN# 3 TO  *
320 ASSIGN# 4 TO  "YDATA:D701"
330 READ# 4 ; MAINY()
340 ASSIGN# 4 TO  *
350 ASSIGN# 5 TO  "INFO:D701"
360 READ# 5 ; INFO$()
370 ASSIGN# 5 TO  *
380 BEEP
390 !                             COND$ contains information on irradiation condition
400 COND$(1)=INFO$(1)
410 COND$(2)=INFO$(2)
420 !                                                  MAG is the print magnification
430 MAG=VAL (INFO$(3))
440 !                                       The next section determines the number of
450 !                                       zones/attempts retrieved from disc
460 !                                       FZ is number of first zone to be analysed
470 FZ=VAL (INFO$(4))
480 !                                        LZ is number of last zone to be analysed
490 LZ=VAL (INFO$(5))
500 !                                             N is number of zones to be analysed
510 N=LZ-FZ+1
520 !                                  TOTJ is number of attempts required for N zones
530 TOTJ=3*N
540 DISP "ZONES";FZ;"TO";LZ;"ARE TO BE ANALYSED,";N;"ZONES"
550 DISP
560 !                 This loop requires input from keyboard for each zone. If zone
570 !                 K has collapsed, a 1 should be entered into COLLAPSE(K).
580 !                 Otherwise a 0 should be entered.
590 !                                                        K is the current zone number
600 FOR K=FZ TO LZ
610 !                           NEWK is a dummy variable which aids array manipulation
620 !                           K runs from FZ to LZ, NEWK runs from 1 to N.
630 NEWK=K-FZ+1
640 DISP "HAS ZONE";K;"COLLAPSED","1=YES  0=NO"
650 INPUT COLLAPSE(NEWK)
660 NEXT K
670 S=0
    !                           This loop calculates all 5 parameters for all atte
                                                        the current zone K
```

```
710 !                                                  P is current attempt at zone r
720 P=P+1
730 IF P>3 THEN P=1
740 K=(J+2.9) DIV 3
750 !                          Redimensioning DIGX/Y appropriately for each attempt
760 REDIM DIGX(IMAX(J))
770 REDIM DIGY(IMAX(J))
780 !                                  This section transfers coords of attempt J
790 !                                  from MAINX/Y into DIGX/Y for calculation
800 IF J>1 THEN 840
810 MAT DIGX=MAINX(1:IMAX(J))
820 MAT DIGY=MAINY(1:IMAX(J))
830 GOTO 870
840 MAT DIGX=MAINX(IMSUM(J-1)+1:IMSUM(J))
850 MAT DIGY=MAINY(IMSUM(J-1)+1:IMSUM(J))
860 !                          CONVERT converts from digitizer units to millimetres
870 GOSUB CONVERT
880 !                     ************* POSITION *************
890 !                         Coords of zone position, POSX/Y, are defined as the
900 !                         mean of all coords on the periphery of the zone
910 SUMX=SUM (DIGX)
920 SUMY=SUM (DIGY)
930 POSX(J)=SUMX/IMAX(J)
940 POSY(J)=SUMY/IMAX(J)
950 !                     ************** DIAMETERS ************
960 !              RADIUS(S) is the distance between the zone centre, POSX/Y and
970 !              the point S on the periphery. (There are IMAX(J) points). The
980 !              mean radius of the zone is the average value of the elements
990 !              of RADIUS, MEANRAD.The mean diameter, MEANDIAM is double
1000 !              MEANRAD.
1010 !              DIAM(S) is the distance from the point S to OUTPNT.The maximum
1020 !              The furthest point from the centre, POSX/Y is OUTPNT. The
1030 !              point which lies furthest from the centre is OUTPNT.
1040 !              distance from OUTPNT to point S is DIAM(S).The maximum diamete
1050 !              of the zone is taken as the maximum element of array DIAM.
1060 !              The elongation ratio of the zone, ELONG is the ratio of the
1070 !              mean to maximum diameters.
1080 REDIM RADIUS(IMAX(J)),DIAM(IMAX(J))
1090 REDIM MAXDIAM(TOTJ),MEANDIAM(TOTJ),ELONG(TOTJ)
1100 FOR S=1 TO IMAX(J)
1110 RADIUS(S)=SQR ((POSX(J)-DIGX(S))^2+(POSY(J)-DIGY(S))^2)
1120 NEXT S
1130 MAXRAD=AMAX (RADIUS)
1140 OUTPNT=AMAXROW
1150 FOR S=1 TO IMAX(J)
1160 DIAM(S)=SQR ((DIGX(OUTPNT)-DIGX(S))^2+(DIGY(OUTPNT)-DIGY(S))^2)
1170 NEXT S
1180 MEANRAD=SUM (RADIUS)/IMAX(J)
1190 MEANDIAM(J)=2*MEANRAD
1200 MAXDIAM(J)=AMAX (DIAM)
1210 ELONG(J)=MEANDIAM(J)/MAXDIAM(J)
1220 !                     ************* ZONE SHAPE *************
1230 !              STANDEV(J) is the standard deviation of the elements of RADIUS
1240 !              for attempt J. Thus a large STANDEV signifies an irregular
1250 !              shaped zone.
1260 A=FNORM (RADIUS)
1270 SUMSQ=A^2
1280 STANDEV(J)=SQR ((SUMSQ-2*MEANRAD*SUM (RADIUS))/IMAX(J)+MEANRAD^2)/MEANRAD
1290 !                     *************** AREA ***************
1300 !                           Zone AREA is calculated by summing areas of small
1310 !                           triangles which have points I,I+1 and the origin
1320 !                           as vertices.
1330 AREA=0
1340 FOR I=1 TO IMAX(J)-1
1350 SUBAREA=(DIGY(I+1)*DIGX(I)-DIGY(I)*DIGX(I+1))/2
1360 AREA=AREA+SUBAREA
1370 NEXT I
1380 SUBAREA=(DIGY(1)*DIGX(IMAX(J))-DIGY(IMAX(J))*DIGX(1))/2
     TOTALAREA=TOTALAREA+SUBAREA
                                        ... is the last digitised ...
```

```
1410 !                                  negative and must be inverted
1420 IF INFO$(6)="A" THEN 1450
1430 AREA=-AREA
1440 !                                                  AREAS(J) is the area of attempt J
1450 AREAS(J)=AREA
1460 !                                  At the end of the third attempt, (P=3), MEANS
1470 !                                  calculates the mean value of each parameter
1480 !                                  for all 3 attempts at each zone.
1490 ON P GOSUB DUMMY ,DUMMY ,MEANS
1500 IF P=3 THEN DISP K
1510 NEXT J
1520 !                                                  MASTER is the main storage area
1530 !           The various parameters are stored in the columns of MASTER
1540 !           such that data from a particular zone occupies a single row
1550 MAT MASTER(,1)=COLLAPSE
1560 MAT MASTER(,2)=XZONEPOS
1570 MAT MASTER(,3)=YZONEPOS
1580 MAT MASTER(,4)=ZONEAREA
1590 MAT MASTER(,5)=ZONEMAXDI
1600 MAT MASTER(,6)=ZONEMEANDI
1610 MAT MASTER(,7)=ELONGATION
1620 MAT MASTER(,8)=STDEV
1630                                            Next section transfers MASTER to disc
1640 !             Data is extracted from MASTER by rows (ie zones) so that
1650 !             each zone may be stored on disc in its own record. Thus
1660 !             if zone numbers 50 to 160 have been analysed, the data
1670 !             will be stored in records numbered 50 to 160.
1680 FOR K=FZ TO LZ
1690 NEWK=K-FZ+1
1700 MAT ZONEINFO=MASTER(NEWK,)
1710 ASSIGN# 1 TO  "ZONEDATA"
1720 PRINT# 1,K ; ZONEINFO()
1730 ASSIGN# 1 TO  *
1740 NEXT K
1750 ASSIGN# 2 TO  "CONDITION"
1760 PRINT# 2 ; COND$()
1770 ASSIGN# 2 TO  *
1780 END
1790 !                                  ALLCLEAR sets all array elements to zero
1800 ALLCLEAR:
1810 MAT AREAS=ZER
1820 MAT DIGX=ZER
1830 MAT DIGY=ZER
1840 MAT POSX=ZER
1850 MAT POSY=ZER
1860 MAT MAINX=ZER
1870 MAT MAINY=ZER
1880 MAT IMAX=ZER
1890 MAT IMSUM=ZER
1900 MAT DIAM=ZER
1910 MAT RADIUS=ZER
1920 MAT XZONEPOS=ZER
1930 MAT YZONEPOS=ZER
1940 MAT ZONEAREA=ZER
1950 MAT MAXDIAM=ZER
1960 MAT ZONEMAXDI=ZER
1970 MAT MEANDIAM=ZER
1980 MAT STANDEV=ZER
1990 MAT ELONG=ZER
2000 MAT ZONEMEANDI=ZER
2010 MAT STDEV=ZER
2020 MAT COLLAPSE=ZER
2030 MAT MASTER=ZER
2040 MAT ELONGATION=ZER
2050 MAT ZONEINFO=ZER
2060 DIAMCLEAR:
2070 MAT DIAM=ZER
2080 RETURN
2090
2100 CONVERT:
```

```
2110 MAT DIGX=( 250000/MAG)*DIGX
2120 MAT DIGY=( 250000/MAG)*DIGY
2130 RETURN
2140 DUMMY:
2150 RETURN
2160 !
2170 !                                          MEANS calculates mean of 3 attempts
                                                for all 5 parameters for each zone
2180 MEANS:
2190 ZONEAREA(K)=(AREAS(J)+AREAS(J-1)+AREAS(J-2))/3
2200 XZONEPOS(K)=(POSX(J)+POSX(J-1)+POSX(J-2))/3
2210 YZONEPOS(K)=(POSY(J)+POSY(J-1)+POSY(J-2))/3
2220 ZONEMAXDI(K)=(MAXDIAM(J)+MAXDIAM(J-1)+MAXDIAM(J-2))/3
2230 ZONEMEANDI(K)=(MEANDIAM(J)+MEANDIAM(J-1)+MEANDIAM(J-2))/3
2240 ELONGATION(K)=(ELONG(J)+ELONG(J-1)+ELONG(J-2))/3
2250 STDEV(K)=(STANDEV(J)+STANDEV(J-1)+STANDEV(J-2))/3
2260 RETURN
```

```
10  ! ************************ THIS IS DISTRIBS ********************************
20  !
30  !   This program takes the data on each zone produced by AREA calculating
40  ! the mean value for the zone population and creating a frequency distri-
50  ! bution for all 5 parameters, for both total and collapsed populations.
60  ! Note that it is assumed that all zones are being analysed and not just
70  ! data from one disc (ie assumed that the first zone is number 1).
80  !    Columns 1 to 8 of MASTER contain data on COLLAPSE,X-COORDS,Y-COORDS,
90  ! AREA,MAX DIAM,MEAN DIAM,ELONGATION RATIO and SHAPE FACTORS respectively
100 !                                                  Dimensioning all arrays
110 OPTION BASE 1
120 SHORT MASTER(400,8),LOOPS(400,7),SUMS(8),LOOPSUMS(7),ZONEINFO(8)
130 SHORT POPX(400),POPY(400),POPAREA(400),POPMAXD(400),POPMEAND(400)
140 SHORT POPRATIO(400),POPSHAPE(400),LOOX(400),LOOY(400)
150 SHORT LOOAREA(400),LOOMAXD(400),LOOMEAND(400),LOORATIO(400)
160 SHORT LOOSHAPE(400),WORK(400),FREQ(15),MID(15),RELFREQ(15)
170 SHORT MEANX,SDEVX
180 GOSUB ALLCLEAR
190 BEEP
200 !                                          Redimensioning all arrays to the
210 !                                          correct population size.
220 DISP "HOW MANY ZONES ARE TO BE ANALYSED"
230 INPUT LZ
240 REDIM MASTER(LZ,8)
250 REDIM POPX(LZ)
260 REDIM POPY(LZ)
270 REDIM POPAREA(LZ)
280 REDIM POPMAXD(LZ)
290 REDIM POPMEAND(LZ)
300 REDIM POPRATIO(LZ)
310 REDIM POPSHAPE(LZ)
320 REDIM WORK(LZ)
330 !                          This section reads data stored by AREA from disc
340 !                          in drive 1, and stores it in array MASTER.
350 FOR K=1 TO LZ
360 ASSIGN# 1 TO  "ZONEDATA"
370 READ# 1,K ; ZONEINFO()
380 ASSIGN# 1 TO  *
390 MAT MASTER(K,)=ZONEINFO
400 NEXT K
410 !                          This section transfers data on zones which have
420 !                          collapsed from MASTER to LOOPS
430 !                          Array SUMS contains column sums of MASTER
440 MAT SUMS=CSUM (MASTER)
450 !                             Since each collapsed zone has COLLAPSE(K)=1,
460 !                             SUMS(1) is the number of collapsed zones
470 REDIM LOOPS(SUMS(1),7)
480 REDIM LOOX(SUMS(1))
490 REDIM LOOY(SUMS(1))
500 REDIM LOOAREA(SUMS(1))
510 REDIM LOOMAXD(SUMS(1))
520 REDIM LOOMEAND(SUMS(1))
530 REDIM LOORATIO(SUMS(1))
540 REDIM LOOSHAPE(SUMS(1))
550 TOM=0
560 FOR K=1 TO LZ
570 IF MASTER(K,1)=0 THEN 600
580 !          Subroutine SELECT transfers data on collapsed zones to LOOPS
590 GOSUB SELECT
600 NEXT K
610 !                                    LOOPSUMS contains the column sums of LOOPS
620 MAT LOOPSUMS=CSUM (LOOPS)
630 !                    Subroutine ARRAYS transfers columns of MASTER/LOOPS to
640 !                    appropriate arrays for manipulation. Prefixes POP and
650 !                    LOOP refer to total and collapsed populations respectively
660 GOSUB ARRAYS
670 !                    Subroutine DISTRIB creates a frequency distribution for
680                      relevant parameter. WORK contains the array for which
                         the distribution is to be created. FN is the name
                         number of the particular distribution
```

```
710 !                    be transferred.
720 RN=0
730 MAT WORK=POPAREA
740 GOSUB DISTRIB
750 MAT WORK=POPMAXD
760 GOSUB DISTRIB
770 MAT WORK=POPMEAND
780 GOSUB DISTRIB
790 MAT WORK=POPRATIO
800 GOSUB DISTRIB
810 MAT WORK=POPSHAPE
820 GOSUB DISTRIB
830 !            Since the number of zones which have collapsed is = 5000
840 !            of the total population, WORK must be redimensioned.
850 LZ=SUMS(1)
860 REDIM WORK(LZ)
870 MAT WORK=LOOAREA
880 GOSUB DISTRIB
890 MAT WORK=LOOMAXD
900 GOSUB DISTRIB
910 MAT WORK=LOOMEAND
920 GOSUB DISTRIB
930 MAT WORK=LOORATIO
940 GOSUB DISTRIB
950 MAT WORK=LOOSHAPE
960 GOSUB DISTRIB
970 END
980 !                                          ALLCLEAR clears all arrays.
990 ALLCLEAR:
1000 MAT MASTER=ZER
1010 MAT LOOPS=ZER
1020 MAT SUMS=ZER
1030 MAT ZONEINFO=ZER
1040 MAT POPX=ZER
1050 MAT POPY=ZER
1060 MAT POPAREA=ZER
1070 MAT POPMAXD=ZER
1080 MAT POPMEAND=ZER
1090 MAT POPRATIO=ZER
1100 MAT POPSHAPE=ZER
1110 MAT LOOX=ZER
1120 MAT LOOY=ZER
1130 MAT LOOAREA=ZER
1140 MAT LOOMAXD=ZER
1150 MAT LOOMEAND=ZER
1160 MAT LOORATIO=ZER
1170 MAT LOOSHAPE=ZER
1180 MAT WORK=ZER
1190 RETURN
1200 !                   SELECT transfers data on collapsed zones to LOOPS
1210 SELECT:
1220 TOM=TOM+1
1230 MAT LOOPS(TOM,)=MASTER(K,2:8)
1240 RETURN
1250 !                   ARRAYS transfers rows of MASTER to working arrays
1260 ARRAYS:
1270 MAT POPX=MASTER(,2)
1280 MAT POPY=MASTER(,3)
1290 MAT POPAREA=MASTER(,4)
1300 MAT POPMAXD=MASTER(,5)
1310 MAT POPMEAND=MASTER(,6)
1320 MAT POPRATIO=MASTER(,7)
1330 MAT POPSHAPE=MASTER(,8)
1340 MAT LOOX=LOOPS(,1)
1350 MAT LOOY=LOOPS(,2)
1360 MAT LOOAREA=LOOPS(,3)
1370 MAT LOOMAXD=LOOPS(,4)
1380 MAT LOOMEAND=LOOPS(,5)
1390 MAT LOORATIO=LOOPS(,6)
1400 MAT LOOSHAPE=LOOPS(,7)
```

```
1410 RETURN
1420 DISTRIB:
1430 RN=RN+1
1440 !          This section sets range and class interval for each parameter
1450 !          UCL=Upper Class Limit;LCL=Lower Class Limit;CW=Class Width
1460 IF RN=1 OR RN=6 THEN CW=1300
1470 IF RN=1 OR RN=6 THEN LOWX=0
1480 IF RN=2 OR RN=3 OR RN=7 OR RN=8 THEN CW=25
1490 IF RN=2 OR RN=3 OR RN=7 OR RN=8 THEN LOWX=0
1500 IF RN=4 OR RN=9 THEN CW=.035
1510 IF RN=4 OR RN=9 THEN LOWX=.5
1520 IF RN=5 OR RN=10 THEN CW=.025
1530 IF RN=5 OR RN=10 THEN LOWX=0
1540 DIEP RN
1550 !                                        Calculating mean value of parameter
1560 MEANX=SUM (WORK)/LZ
1570 !                              Calculating standard deviation of distribution
1580 A=FNORM (WORK)
1590 SUMSQ=A^2
1600 SDEVX=SQR ((SUMSQ-LZ*MEANX^2)/LZ)
1610 !                                          MID contains the class midpoints
1620 !                                  FREQ contains the frequency for each class
1630 MAT MID=ZER
1640 MAT FREQ=ZER
1650 !                                    This loop creates frequency distributior
1660 FOR M=1 TO 15
1670 LCL=LOWX+CW*(M-1)
1680 UCL=LCL+CW
1690 MP=(UCL+LCL)/2
1700 MID(M)=MP
1710 FOR K=1 TO LZ
1720 IF WORK(K)>= UCL THEN 1770
1730 IF WORK(K)<LCL THEN 1770
1740 !                                       Warning given if parameter exceeds range
1750 IF M=15 AND WORK(K)>UCL THEN DISP "PARAMETER BEYOND DIST LIMIT ON";RN
1760 FREQ(M)=FREQ(M)+1
1770 NEXT K
1780 !                              This normalizes frequencies to % of population
1790 RELFREQ(M)=FREQ(M)/LZ*100
1800 NEXT M
1810 HIGHX=UCL
1820 HIGHY=AMAX (FREQ)
1830 !                              This section stores data required for plotting
1840 ASSIGN# 1 TO  "MIDPOINTS"
1850 PRINT# 1,RN ; MID()
1860 ASSIGN# 1 TO  *
1870 ASSIGN# 2 TO  "FREQUENCIE"
1880 PRINT# 2,RN ; RELFREQ()
1890 ASSIGN# 2 TO  *
1900 ASSIGN# 3 TO  "COORDS"
1910 PRINT# 3,RN ; MEANX,SDEVX,HIGHY,HIGHX,LOWX,CW,LZ
1920 ASSIGN# 3 TO  *
1930 RETURN
```